FINAL REPORT

MONITORING AND HYDROLOGICAL MODELING OF HENVAL WATERSHED IN LESSER HIMALAYA

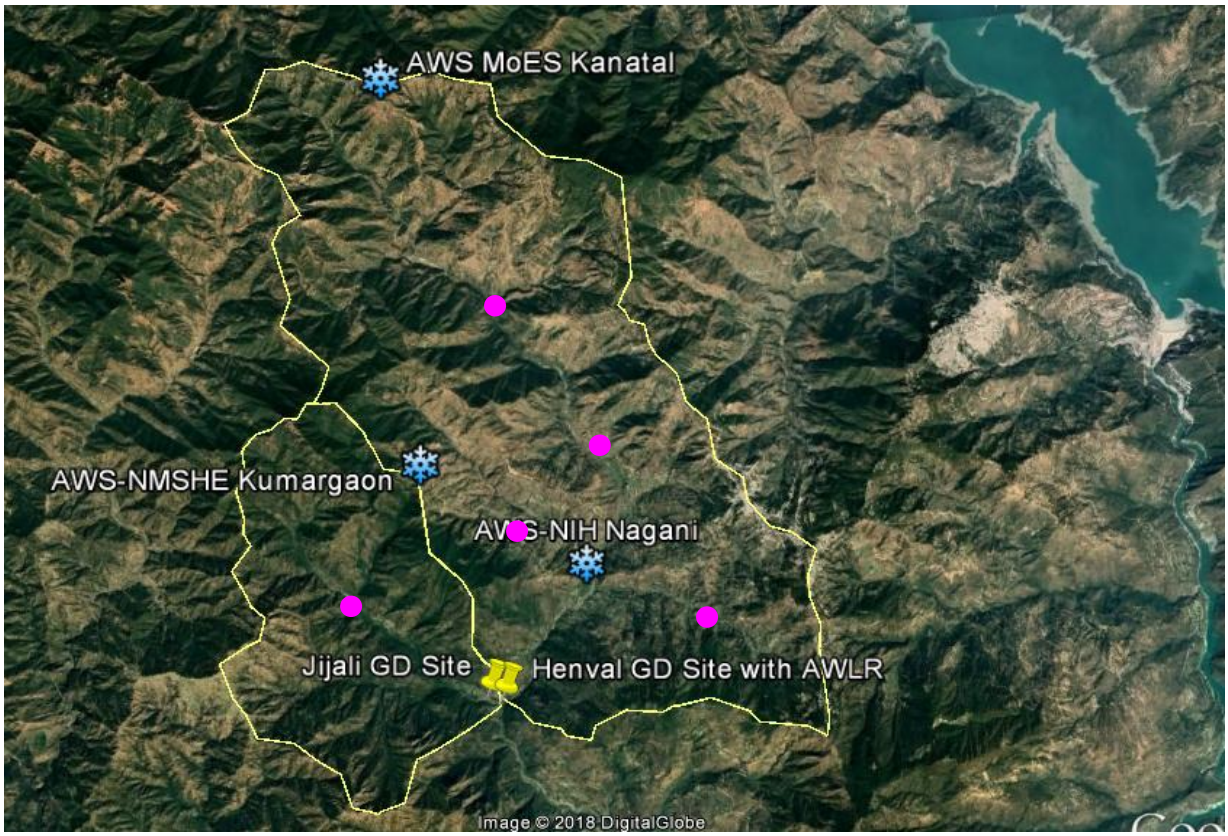

आपो हि ष्ठा मयोभुवः

WATER RESOURCES SYSTEMS DIVISION

NATIONAL INSTITUTE OF HYDROLOGY

ROORKEE- 247 667, UTTRAKHAND, INDIA

JUNE 2025

STUDY TEAM

Director	:	Dr M. K. Goel
Head	:	Dr A. R. Senthil Kumar, Scientist 'G'
Investigators	:	Dr Manish K. Nema, Scientist 'E' (PI)
		Dr P. K. Mishra, Scientist 'D'
		Dr Praveen R Patil, Scientist 'C'

TABLE OF CONTENTS

LIST OF FIGURES

LIST OF TABLES

ABSTRACT

Project Henval aims to develop a deeper understanding of climate-hydrology interaction in the lesser Himalayan experimental catchment with an area of 102 km^2. In the first phase of the project, a state-of-art field observatory was established with various instruments and sensors during 2016-2019. Preliminary data analysis on the estimation of evapotranspiration by various methods and water balancing of the watershed was performed. The field station developed at Henval watershed is envisaged to operate for long-term monitoring of different hydro-climatic variables. This study is the second phase of the project-Henval presents a comprehensive investigation into soil moisture dynamics and hydrological processes in the Lesser Himalayan region, focusing on three major research components: empirical soil moisture modeling, advanced deep learning-based soil moisture prediction, and hydrological modeling using the SPHY model.

The field monitoring of the various variables and the development of baseline datasets for the Henval watershed shall be a continuous process in this phase of the study. Firstly, an empirical soil moisture model was developed using key meteorological parameters—rainfall, wind speed, air temperature, and near-surface soil temperature. The model was calibrated and validated at three representative sites: Kumargaon, Kanataal, and Nagini. Among these, the Kumargaon site exhibited the highest model performance, with strong statistical agreement in both calibration and validation phases. The simplified version of the model, based on averaged optimized parameters, maintained high predictive accuracy at Kumargaon across multiple soil depths (R^2 = 0.86 at 2 cm, 0.83 at 6 cm, and 0.64 at 25 cm). In contrast, performance at Kanataal and Nagini was moderate, with a noticeable decline in model accuracy at greater depths, highlighting the diminishing influence of meteorological inputs on subsurface moisture. These findings emphasize the utility of empirical approaches while acknowledging their limitations for deeper soil layers.

Building upon these insights, the second research component employed advanced deep learning techniques to enhance soil moisture prediction. Two hybrid models—Convolutional Neural Network–Long Short-Term Memory (CNN-LSTM) and Recurrent Neural Network–LSTM (RNN-LSTM)—were developed to model subsurface soil moisture at 25 cm and 50 cm depths across the same stations. The CNN-LSTM model consistently outperformed the RNN-LSTM model, as evidenced by lower mean absolute error (MAE), root mean square error (RMSE), and higher coefficient of determination (R^2). The superior performance of CNN-

LSTM highlights its ability to capture both spatial and temporal dependencies in meteorological and soil data, making it a reliable tool for soil moisture estimation in data-scarce mountainous environments. This modeling framework offers promising applications in precision agriculture, drought monitoring, and water resource management under changing climatic regimes.

The third and final component of the study applied the SPHY (Spatial Processes in Hydrology) model to simulate hydrological processes in a non-glaciated watershed within the Upper Ganga Basin over a 14-year period (2010–2023). The model was calibrated and validated using observed hydrometeorological data and demonstrated robust performance in simulating key hydrological components—surface runoff, lateral flow, baseflow, and evapotranspiration—under complex Himalayan terrain. The SPHY model also proved adaptable for application across similar catchments in the northwestern Himalayas. Its integration with geospatial tools and satellite-derived datasets further enhances its utility for hydrological assessment in data-limited regions. Given the critical dependence of Himalayan hydrology on temperature and precipitation, particularly in light of climate change, SPHY provides a valuable platform for assessing watershed responses and informing water resource planning and adaptation strategies.

In summary, the study demonstrates that combining empirical models, deep learning algorithms, and physically-based hydrological models can significantly improve the understanding and prediction of soil moisture and watershed hydrology in complex mountainous regions. These methodologies collectively contribute to more informed decision-making in water resource management and climate resilience planning in the Himalayas.

Chapter 1

1.0 INTRODUCTION

1.1 General:

Watershed is supposed to be the basic unit at which the hydrologic processes are studied and is central to most of the concepts in hydrology. Experimental hydrology still has a unique place with no alternative for testing and developing new research hypotheses and models. Given the importance of experimental hydrology, NIH has initiated an experimental hydrologic project for a small lesser Himalayan watershed, namely, Henval. In the first phase of the project, a state-of-art field observatory was established with various instruments and sensors during 2016-2019. Preliminary data analysis on the estimation of evapotranspiration by various methods and water balancing of the watershed was performed. The field station developed at Henval watershed is envisaged to operate for long-term monitoring of different hydro-climatic variables. This study is supposed to be the second phase of the project.

In view of the state of affairs of existing models and studies addressing the problems of watershed hydrology, the significant limitations might be characterized as mainly twofold. First, study basin designs have been limited by the black box concept and many misconceptions (e.g., the linearity, non-heterogeneity, additivity of hydrologic systems, etc.). Second, the operation has been substantially bounded by the hydraulic conception of these watersheds as isolated hydrological systems (Wei-Zu et al. 2013). Most of the watershed studies monitor only total runoff at the stream-outlet, and the subsurface responses of the watershed are only estimated by hydrograph separation, etc. These characteristics undermine the formulation of a unified theory of watershed hydrology (Sivapalan et al. 2005) and the development of watershed models (Kirchner, 2006; Mcdonnell et al., 2007). There is a clear need to move beyond the status quo and expand from this narrow hydrological perspective to generate hypotheses governing general behaviour across places and scales, with the ultimate aim to advance the science of hydrology.

In the Himalayan mountains, “naula” (1-2 m deep, approximately lined wells to get water from seepage) and "dhara" (springs) are the primary sources of water for drinking and household consumption. Deforestation, grazing and trampling by livestock, erosion of top fertile soil, forest fires and development activities (e.g. road-widening, mining, building construction, etc.)

reduces the infiltration rate and sponge action of the land, which results in unchecked flow of water during the monsoon to cause sudden swelling of streams and rivers, so that there are floods in the foothills and even in the plains, and droughts in the villages located on the slope of the mountains. The difficulty to understand the nature of hilly areas possesses severe limitation on-ground observation. Field experimentation and information collection to develop planning activities for proper planning and management of water resources is therefore necessary.

Hydrological changes experienced by the Himalayan basins are very critical to the water security of the northern Indian plains. Rising temperatures, changing glaciers and reducing snow cover are indicative of the nature of the changing climate of the Himalaya in the recent past (Bhutiyani et al., 2007, 2010). While cryosphere components dictate the hydrology of the higher Himalayan region, the lesser Himalayan regions experience the highest precipitation across the Himalayan slopes and have a more considerable influence on the basin hydrology. However, the climate- hydrology linkages of this critical region are least known. The climate of the Himalayan slopes is dictated by the orographic forcing and strong linkages between temperature distribution of the mountain slopes and atmospheric saturation conditions by summer/winter monsoon (Thayyen and Dimri, 2014). How these processes are impacting the present and future regional hydrology is the crucial question. Thorough understanding of the coupling between surface hydrologic systems and the overlying atmospheric system under orographic moisture flow is essential to address this question. An experimental research station with state-of-art instrumentation with a long-term research framework is being set up in the lesser Himalayan region to gain understanding on these issues. This research station is aimed to produce baseline data of weather and hydrology of the lesser Himalayan mountains leading to a better understanding of climate-hydrology interaction under changing climate of the region. Since the Himalayan tributaries play an essential role in maintaining the hydrologic regime of the Ganges River; sustained research from this experimental station will help in managing the water resources of Himalayan tributaries of Ganges River under the climate change scenario.

1.2 Background

The field monitoring of the various variables and development of baseline datasets for the Henval watershed shall be a continuous process in this study. Hydrological modeling of the stream is planned to understand the catchment characteristics and runoff behaviour of the

watershed. Soil moisture is the crucial variable for partitioning rainfall into infiltration and runoff, thus playing a fundamental role in runoff modelling and flood forecasting. Recently, the scientific community is making an excellent effort to address soil moisture estimation over large areas through in situ sensors, remote sensing, and modelling approaches. There is sizeable spatial-temporal variability of soil moisture that exists in field conditions. Currently, we are able to estimate soil moisture accurately at the point scale through in-situ sensors.

Moreover, satellite sensors can obtain less accurate measurements at a coarse scale (~20 km). Finally, spatial downscaling/upscaling approaches can be used to integrate the different techniques and observations with modelling. Data assimilation and merging methods can also be considered to integrate in-situ, satellite and modelled data optimally. Based on the background above the study has been taken up for long term monitoring with the following objectives:

1. To develop a baseline runoff and meteorological data of Henval watershed with the established experimental setup.
2. To carry out Hydrological modelling of Henval river
3. To model the spatial-temporal variability and temporal-stability of the soil moisture
4. To compare and validate the satellite soil moisture data with the in-situ observations

This second phase of the study was concluded in August 2024 after three years of filed based modelling and monitoring work. However, the field observatories established under the project-Henval are likely to be extended for a longer run and suplimenting the in-situ data to the NIH.

Chapter 2

2.0 STUDY AREA

2.1 General

A small Himalayan hilly watershed of Henval River up to Jijali has been selected in the upper Ganga basin in the state of Uttarakhand for the study. This study area consists of paired watersheds. One of them is a forested catchment (undisturbed), and the other one is an agricultural watershed with anthropogenic interventions including a semi-urban habitat at Chamba (Uttarakhand). The geographical extent of the study area is from $30^0$17'N–$30^0$26'N latitude and $78^0$16'E–$78^0$25'E longitude. This area is a typical representative of a combination of lesser Himalayan hilly temperate climatic conditions with an average annual rainfall range of 1200-1800 mm. The Himalayan subtropical forests yield to a belt of broad temperate leaf and mixed forest mainly comprising of pine forest. The total area under study is 102 km^2 approximately (26 km^2 forested catchment and 76 km^2 the other one) with an elevation range of 999-2676 m. The location map of the watershed within the Upper Ganga Basin is given in Fig. 2.1. The stream in the forested sub-catchment is the source of drinking water for 87 nearby villages. This stream is being pumped 24x7 by the state authorities at its outlet at Dev Nagar for drinking water supply to the villages.

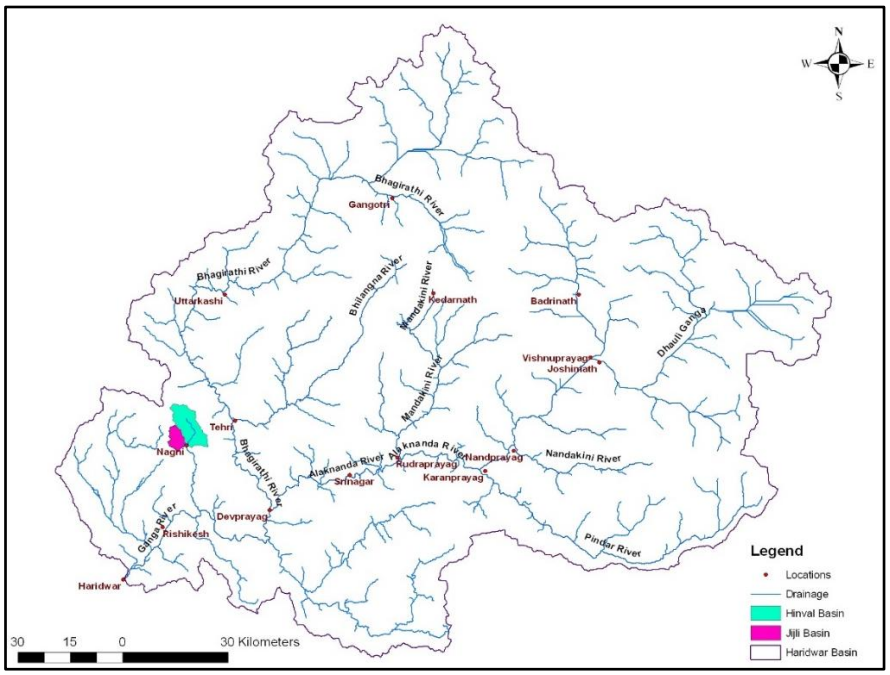

Fig. 2. 1 Location of the Henval watershed up to Jijali within Upper Ganga Basin

2.2 Climate

The climate of this region is generally humid temperate, but observed variations are attributed to physiographic aspects such as altitude, aspect, slope, drainage condition, vegetation, etc. The valleys are hot in summer and cold in winter. The average temperature generally varies from 3ºC to 30ºC. The average yearly rainfall varies from 1200 to 1800 mm. About 70 to 80% of the rainfall occurs during June and September. The rainfall in the study area starts during May and lasts up to November. It was noticed that the uniformity of rainfall was pronounced from the end of June to mid of September), whereas during the other period rainfall distribution is poor and erratic.

2.3 Digital Elevation Model

The study area is a representative of the lesser Himalayas. To characterize the topographical features and delineate the catchment boundaries, Shuttle Radar Topographic Mission (SRTM) Digital Elevation Model (DEM) data of 30m spatial resolution has been used. The study area is characterized by very rugged topography, where the elevation ranges from 988m to 2686m (Fig. 2.2). Hypsometric analysis of the study catchments has also been done and presented in Table 2.1 and Fig. 2.3.

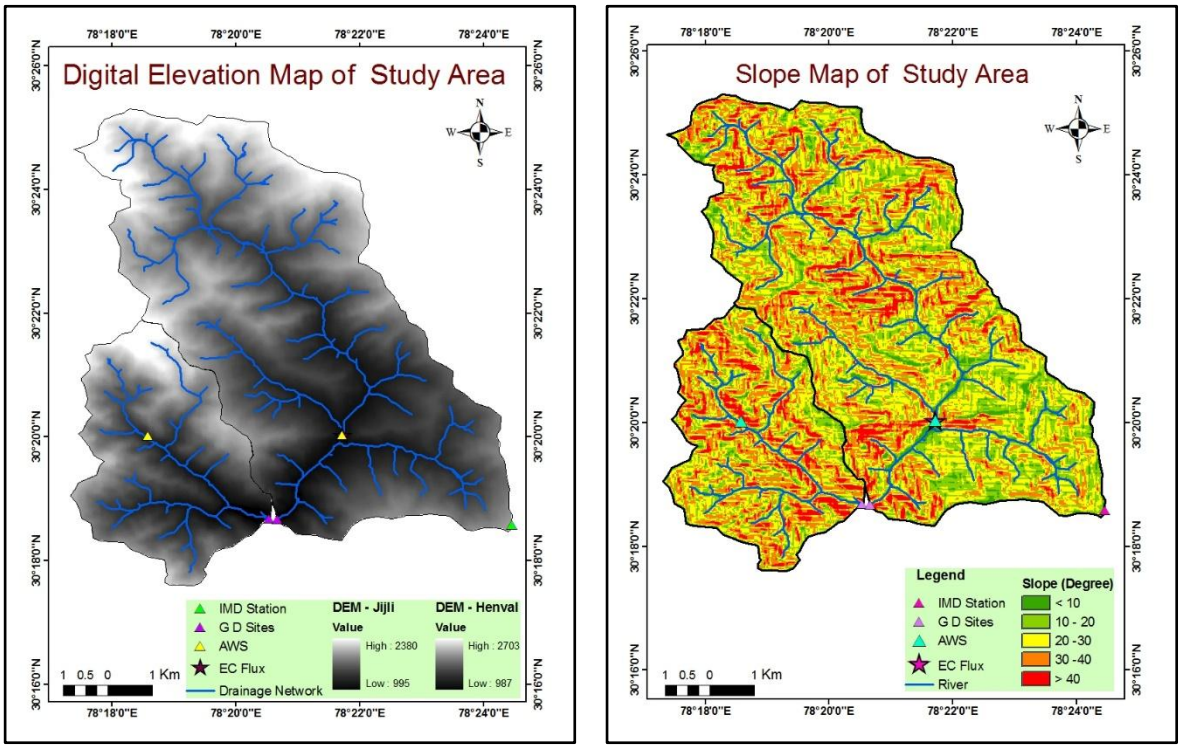

Fig. 2. 2 DEM and Slope Maps of the study Catchments

2.4 Land use land cover

The forest is the major land-cover feature of both the catchments. But, Henval catchment is having a considerable coverage of agricultural and fallow land also (the year 2011) which represent considerable human interventions in the catchment, and Jijali catchment is more pristine in nature as compare to Henval. The land use land cover (LULC) maps of both the catchments have been prepared based on the multispectral satellite images of Landsat L8 Operational Land Imager (OLI) at a spatial resolution of 30-meters. LULC map of the watershed classifies the area in 5 different land cover, i.e. Dense Forest, open forest, agricultural land, barren land and settlement (human settlement). Change of these land cover type in the course of a decade, i.e. from 2001 to 2011, is analysed in this section.

Table 2. 1: Area under various percentage slope classes for the study catchments

S. No.		The area under slope range (%)	
	Slope Range	Henval	Jijali
1	< 10	6.84	5.77
2	10-20	27.28	21.38
3	20-30	34.82	32.38
4	30-40	22.67	27.94
5	>40	8.40	12.53

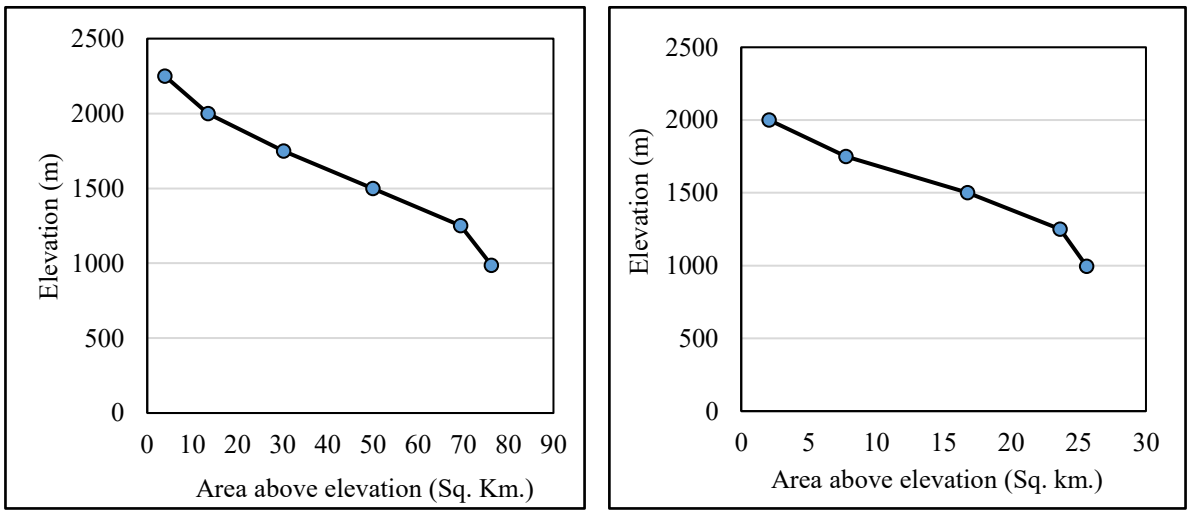

Fig. 2. 3: Hypsometry Curve of Henval (L) and Jijali (R) Catchments

LULC map of Jijali catchment (Fig. 2.4) shows three land cover types in 2001 and four land cover types in 2011. In 2001 Jijali catchment was observed to be cover with three land cover classes which were dense and open forests, and agricultural land. This land cover of three

classes evolved to four classes in 2011, which were dense forests, open forests, agricultural land and barren land.

Fig. 2.4 shows an increase in dense forest, agricultural land and barren land, which was compensated with an appreciable decrease in the open forest area. It can be seen from the Table 2.2 that there is a decrease of 24.65%, which is 6.46 km^2 for Jijali catchment from the year 2001 to 2011 in the open forest land. No settlements were captured in both the years 2001 and 2011 on a scale of 30 m pixel size. Barren land also started growing in the higher elevation of the catchments, which have grown from 0% in 2001 to 2.44% in 2011.

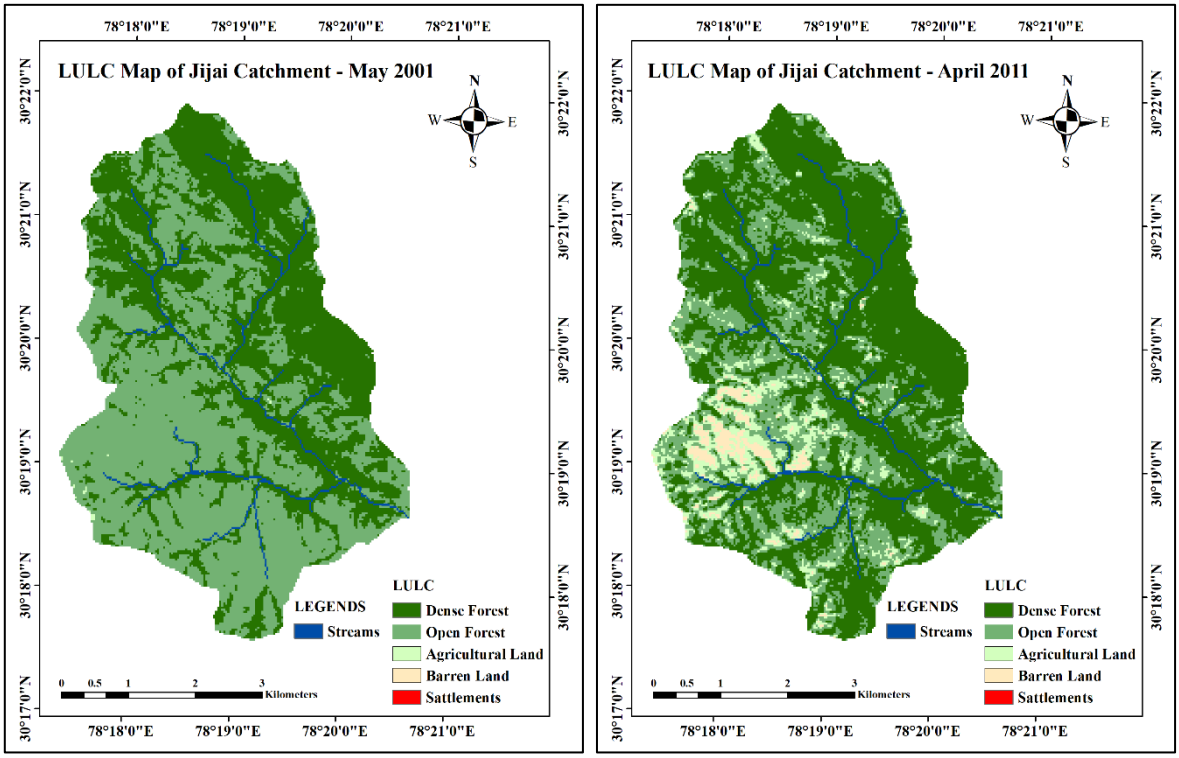

Fig. 2. 4: LULC Maps of the Jijali Catchments for the year 2001(L) and 2011(R)

Table 2. 2: Area of coverage by different land cover within the Jijali catchment

S. No.	Land cover Type	2001 (km^2)	2011 (km^2)	Change Area (km^2)	Change (%)
1	**Dense Forest**	11.76	15.5	3.74	14.27
2	**Open Forest**	14.44	7.98	-6.46	-24.65
3	**Agriculture**	0.02	2.1	2.08	7.94
4	**Barren Land**	0	0.64	0.64	2.44
	Total	26.22	26.22		

LULC map of Henval catchment shows 5 land cover classes (Fig. 2.5). A similar pattern was observed in land cover change like that in Jijali catchment. In Henval catchment also increase in dense forest, agricultural, barren land and land under the settlement was observes which was compensated by the decrease in open forest land.

Table 2.3 indicate the areal coverage of various land uses in the year 2001 and 2011. In the year 2011, a decrease of 30.68% was seen in the open forest area, which accounts for 23.24 km^2 of Henval catchment. Approximately similar increases in the dense forest were noticed in both the catchments, i.e. of 15%.

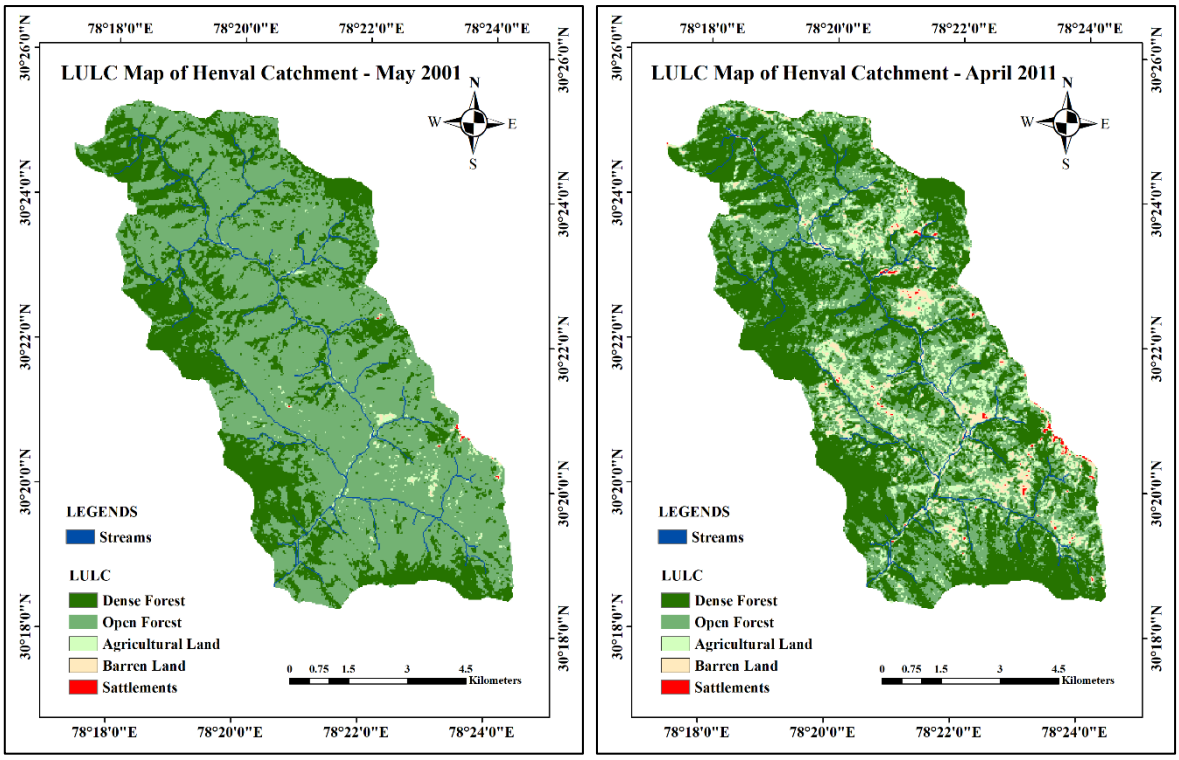

Fig. 2. 5: LULC Maps of the Henval Catchments for the year 2001(L) and 2011(R)

A combined LULC map of both the experimental watersheds is depicted in Fig. 2.6. Watershed, as a whole, shows significant changes from May-2001 to April-2011. All classes excluding open forest land shows an increase in the area. The turnout of the open forest into the dense forest (15.55%, i.e. 15.86 km^2) is the significant change that can be seen over time in the area.

Table 2. 3: Area of coverage by different land cover within the Henval catchment

S. No.	Land cover Type	2001 (km^2)	2011 (km^2)	Change Area (km^2)	Change (%)
1	**Dense Forest**	23.28	35.4	12.11	15.99
2	**Open Forest**	51.57	28.33	-23.24	-30.68
3	**Agriculture**	0.76	8.71	7.95	10.5
4	**Barren Land**	0.12	3.09	2.97	3.92
5	**Settlements**	0.03	0.23	0.21	0.27
	Total	75.76	75.76		

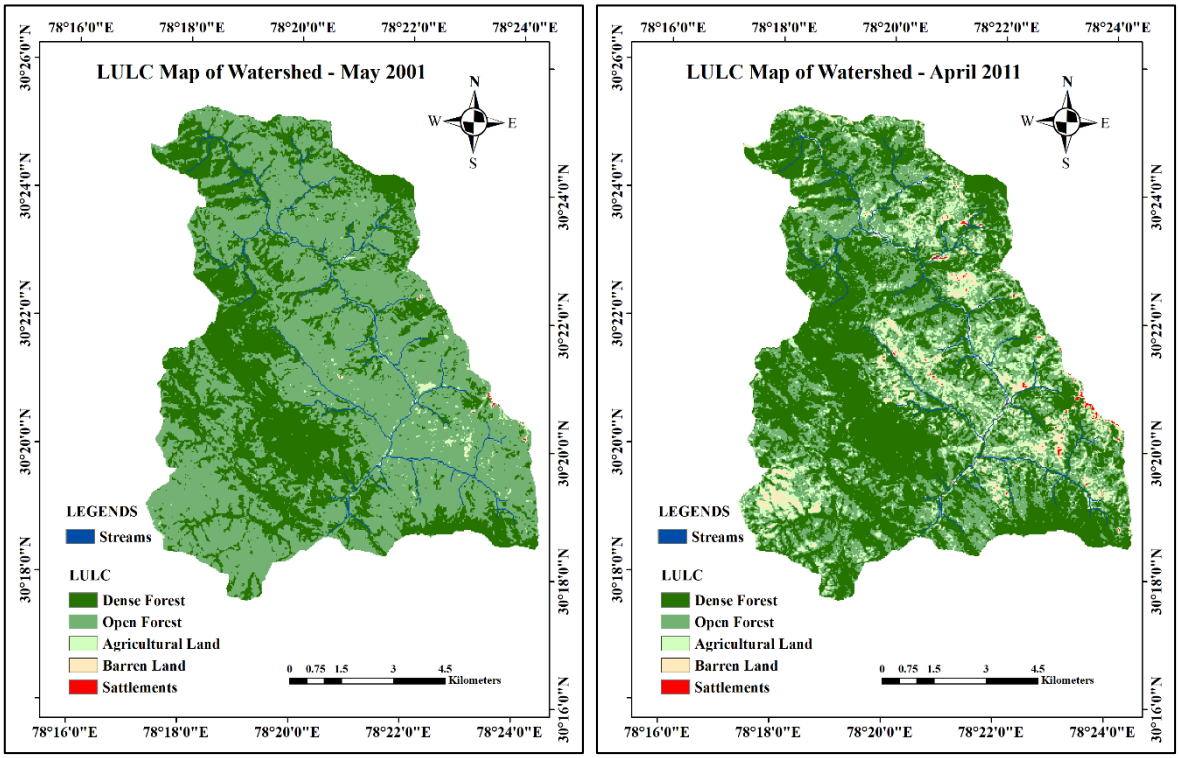

Fig. 2. 6: LULC Maps of the watershed for the year 2001(L) and 2011(R)

Agricultural land, Barren land and Settlements have also increased in the watershed, which is all due to decreased open forest land. The possible reason behind this decrease in open forest land and increase in all other land cover classes can be the unplanned restricted movement of the population in the open forest land for fuel or fodder for their livestock. The reason behind this unplanned restricted movement can be many such as availability of LPG which would limit the fuel consumption from the open forest, increased agricultural area which would help in supplementing food both for the livestock and the population living in the area.

Chapter 3

3.0 DATA AND INSTRUMENTATION

One of the primary objectives of the project is to generate various hydro-meteorological datasets for the study catchment for understanding the hydrological and climatic processes and their interactions. An experimental catchment has been designed with various instrumentations and established the project site at Henval catchment was done to achieve this objective.

3.1 Construction of Rectangular Weirs

Discharge is an essential component and process of the hydrological cycle. Two broad crested rectangular weirs have been constructed to measure the discharge at the outlet of Henval and Jijali. Guidelines for ideal site selections for discharge monitoring were followed. After a survey of many possible gauging sites, a location near to the Uttarakhand Jal Sansthan (UJS) pumping station was identified for construction of a weir across the perennial stream. It was challenging to construct a permanent structure in a running stream, and the success of the structure depends on the skill of the workers. Construction of weir was done in two phases in the first phase the water was diverted to one side, and RCC work on the other side was completed. After two weeks in the second phase, the other side of the weir was casted with water diversion over the completed part.

The weir at Henval is constructed just upstream of the pedestrian cross-over bridge near the pumping station of UJS at Jijali-Devnagar. The length of the weir is 11m, the height is 1.0m (initially 0.7m), and the width of the crest is 0.5m. The weir at Henval was also provided with one staff gauge to measure the water level in the upstream of the weir.

The weir was operated for one entire year successfully, and it was noticed after the first monsoon that the majority of the weir is laden with the silt, boulders and many river bed materials. Thus, it was creating obstacles for proper monitoring of the water level. The issue was discussed within the project team, and it was decided to raise the height of the weir to one meter from 0.7 meter. Then, the second phase of construction works carried over the same weir and after that, the monitoring was continued. Fig. 3.1 shows the evolution of the weir at Henval and various phases of its construction.

Fig. 3. 1: Various phases of construction of Weir at Henval

The second weir at Jijali stream of the forested catchment has been constructed about 250m upstream of the confluence of Jijali and Henval. The dimensions of this weir are 11.5m X 0.7m X 0.5m. The various phases of construction of a weir at Jijali area shown in Fig. 3.2. During the field visit on May 04th, 2016 it was found that the soon after its construction Jijali weir is thoroughly water submerged due to a water intake structure constructed by the Uttarakhand Jal Sansthan (UJS) just downstream of the weir. The situation was examined by the team of experts to resolve the issue. But the requisite free-flow condition for the Jijali weir could not be created in that location, so no observations are available fro Jijali weir. Submerged weir is also visible in the Fig. 3.2

Fig. 3. 2: Various phases of construction of Weir at Jijali

3.2 Installation of Automatic Weather Station (AWS) - Nagani

One automatic weather station (AWS) with soil parameters monitoring station has been purchased from Campbell Scientific and installed in the agricultural catchment (Fig. 3.3) near village Nagani at 1090 m a.s.l.. Initially, the data at an interval of 30min were received at NIH servers through FTP from March 23rd, 2016 on a near real-time basis, but due to poor mobile

network, it was shifted to email-based reporting. The various sensors their make and accuracy and other installation details are given in Table 3.1.

Table 3. 1: Details of the sensors, their accuracy and installation information plugged in in the AWS and the soil Monitoring Station at Nagani

Sensor	Symbol (Unit)	Make	Height/Depth (m)	Stated accuracy
Data loger		Campbell CR1000	NA	NA
AT/RH: Radiation Shield	Ta (^{0}C) RH (%)	Rotronics-HygroClip2	2.0m	±0.2^{0}C ±1.5% RH
Air temperature/Fan Aspirated	Ta (^{0}C)	Rotronics-HygroClip2	2.0m	±0.2^{0}C
Relative Humidity/ Fan Aspirated	RH (%)	Rotronics-HygroClip2	2.0m	±1.5% RH
Wind Speed	U (m s^{-1})	RM Young 05103-45	2.0, m	±0.3m/s
Wind Direction (WD2.0)	WD (^{0})	RM Young 05103-5	2.0 m	±0.3^0
Wind Speed (WS 63cm)	U (m s^{-1})	RM Young 05103-5	2.0m	±0.3m/s
Wind Direction (WD 63 cm)	WD (^{0})	RM Young 05103-5	2.0 m	±0.3^0
Four Component radiometer	(W m^{-2})	Kipp & Zonen (CNR4)	2.5 m	
Air pressure	hpa	Setra CS100 (500-1100hPa)		±0.3hpa
Rain Gauge	(m)	TE525MM	1.0	±1.0cm
Soil temperature (04 Nos.)	T (^{0}C)	107-L	2.0cm (L, R) 30 cm (L, R)	
Soil Moisture, Temp(TDR) Sensor (05 Nos.)		CS655	6.0 cm (L, R) 15 cm (Centre) 50 cm (Centre) 90 cm (Centre)	
Soil Heat flux plate (02 Nos)	(W m^{-2})	Hukseflux HFP01-L	8.0 cm (L, R)	

The data received from March 23rd, 2016, has been processed, analysed, and the results are presented in this report.

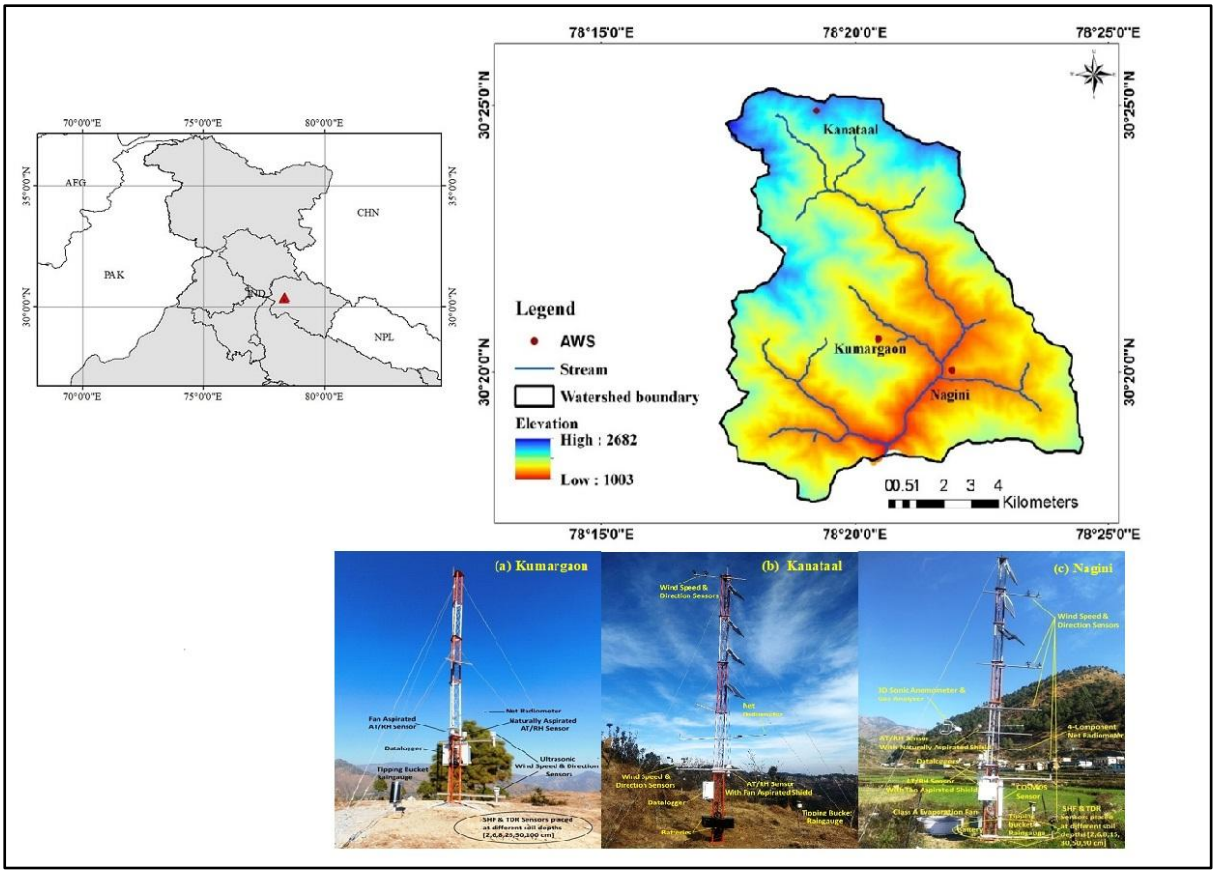

Fig. 3. 3: The automatic weather stations (AWSs) installed at Henval Catchment

3.3 Installation of Automatic Weather Station (AWS) - Kanataal

Another automatic weather station (AWS) with soil parameters monitoring station has been procured from a sponsored project (MoES) and installed in the agricultural catchment (Fig. 3.4) at the Research and Extension Centre of Uttarakhand University of Horticulture and Forestry (UUHF), Kanataal (Tehri Garhwal) of on an elevation of 2590 m a.s.l. Meteorological, soil and solar data are being recorded at this AWS at a frequency of 30 min. The installation of this AWS tower was done on January 04th, 2018. The various sensors their make and accuracy and other installation details are given in the Table 3.2. However, only the results of the analysis of the data received from AWS tower of Nagani (Table 3.3) are presented in this report.

Table 3. 2: Details of the sensors, accuracy and installation information plugged in the AWS and the soil Monitoring Station at Kanataal

Sensor	Symbol (Unit)	Make	Height/ Depth (m)	Stated accuracy
Data logger	-	Campbell CR3000	NA	NA
AT/RH Sensor	Ta (^{0}C) RH (%)	HC2S3-L-20pt	2 m	±0.1°C ±0.8% RH
Compact Aspirated Shield		43502	2 m	
Net Radiometer	(W m^{-2})	NRLite2	2 m	10 µV W-1 m2
Rain Gauge	(m)	TE-525-L25-PT	1 m	1.0% up to 50 mm/h
Heat Flux Sensor	(W m^{-2})	HFP01-L-25pt	2 m	± 3 % (k = 2)
Barometric Pressure Sensor	Mb	CS-106		±0.3 mb
Soil sensor	Ta (^{0}C)	CS-665-L-66pt	2, 6, 25, 50, 100 m	±0.1°C
Wind Speed Sensor	U (m s^{-1})	FST200-201	2, 10 m	±0.5 m/s
Wind Direction Sensor	WD (^{0})	FST200-202	2, 10 m	±3 °

Table 3. 3: Details of Automatic Weather Station (AWS) considered

Station	AWS1	AWS2	AWS3
Location (Lat-Long)	30˚ 21' 00" N, 78˚ 19' 40.80" E	30˚ 24' 53.08" N, 78˚ 19' 17.98" E	30° 19' 54.11" N, 78° 21' 40.19 " E
Elevation	1798 m	2590 m	1000 m
Soil type	Loamy	Loamy	Sandy-Loam
land use	Open Forest	Apple Orchid	Agricultural Land

3.4 Installation of Automatic Water Level Recorder (AWLR)

For the measurement of discharge at the outlet of Henval, a weir has been constructed as discussed in section 3.1. An automatic radar type water level recorder with telemetric arrangement has been purchased and installed (Fig. 3.4) to monitor the water levels (head over the weir). It is a non-contact device which looks down toward the river water. The installation of AWLR was not easy. A complete telescopic cantilever with a perpendicular balancing arrangement with stay-wires was fabricated at the NIH workshop. The cantilever transported to the project site and fixed with a masonry civil structure with many humanitarian efforts.

Installation of AWLR is in the upstream of pedestrian cross-over bridge near the pumping station of UJS at Jijali-Devnagar. AWLR is a fully computerized, digital and self-contained power source system, fitted with data logger and battery charging solar panel with rechargeable batteries with sealed waterproof enclosure for the data logger. The data logger is placed on the rooftop of the nearby residential quarter of UJS employee.

Fig. 3. 4: The digital water level recorder (DWLR) installed on the outlet of Henval stream

3.5 Eddy Flux Tower

Variables describing the turbulent transport such as three components of the 3-dimensional wind speed (u, v, w), sonic temperature (Ts), the concentration of the gas of interest, and water vapour serves the requirement of eddy covariance method for the computation of evapotranspiration. These measurements have to be fast to be able to compute the gas flux and are captured by an eddy covariance station. The term “fast” usually refers to devices capable

of adequately measuring processes at about 10 Hz (10 times per second). The instrumentation consists of a **3-dimensional sonic anemometer** and an **open-path gas analyser**. The gas analyser is usually positioned at or slightly below the sonic anemometer level. The vertical and horizontal separation between the anemometer and other instruments should be kept to a minimum, preferably not exceeding 15 to 20 cm.

3.5.1 3-Dimensional Sonic Anemometer

A 3-dimensional sonic anemometer uses 3 pairs of transducers to measure the speed of sound for each pair. Three vector components of wind speed are then computed, and the vertical wind speed component (w) is used for the eddy covariance calculations. The three main types of the physical arrangement of sonic anemometers most used in eddy covariance are:

1. Omni-directional design with u, v and w components measured in the same physical space by non-orthogonal off-axis pairs of transducers (e.g., not at 90° to each other),
2. Non-Omni directional c-clamp design with u, v and w components measured in the same physical space by non-orthogonal pairs of transducers,
3. C-clamp design with u, v and w components measured in the same or different physical spaces by orthogonal transducers, with w measured by a pair of vertically aligned transducers.

3.5.2 Gas Analyser

There are many different ways to measure gas content in the air. These may be based on chemical, electric, optical and other types of technology. However, not all of these measurements are suitable for eddy covariance. In the eddy covariance method, fast fluctuations in atmospheric gas concentration need to be sampled with high resolution at a frequency of about 10 Hz. Chemical sensors are usually too slow for such sampling, and electric sensors generally do not work well with the low concentrations of gases typically found in the atmosphere. Optical analysers, however, can be sufficiently fast for use in eddy covariance, depending on the performance of the specific instruments.

The flux tower arrangement installed at the site in Henval valley contains a 3-D sonic anemometer, i.e**. CSAT-3A** by Campbell scientific (Fig 3.3), for the measurements of the turbulent fluctuations of horizontal and vertical wind, and an open-path gas analyser, i.e. **EC 150** by Campbell scientific (Fig 3.3), specially designed for eddy-covariance carbon and water

flux measurements. As a stand-alone analyser, it simultaneously measures absolute carbon-dioxide and water-vapour densities, air temperature, and barometric pressure.

Fig. 3. 5: The Eddy covariance sensor installed at Nagani AWS station

Chapter 4

4.0 SOIL MOISTURE MODELING: EMPIRICAL

4.1 General

Soil moisture plays a vital role in the water transport pathway of soil-plant-atmosphere continuum systems. The moisture content of the soil is a crucial governing variable of the water and energy cycle as it has a strong influence on energy and water balance. In addition, it determines the proportion of incoming longwave solar radiation into outgoing longwave radiation, latent, sensible, and ground heat flux (Entekhabi and Rodriquez-Iturbe, 1994; Collier, 2016) and partitions the rainfall into the runoff, surface storage, and infiltration components (Aubert et al., 2003; Venktesh et al., 2011).

As a consequence, it's estimation and prediction emerged as research focus and significantly applied in various disciplines: for example (a) in earth system dynamics, it affects boundary layer development (Ek and Holtslag, 2004; Zhou and Geerts, 2013; Cioni and Hohenegger, 2017; Zhang et al., 2019) and atmospheric circulation (Haarsma et al., 2009; Koster et al., 2014, 2016; Berg et al., 2017; Van der Linden et al., 2019) (b) in water resource management, soil moisture is used for reservoir operation (Mehrotra, 1999; Srinivasa Prasad et al., 2013; Kumari, 2019), drought assessment (Mozny et al., 2012; Mananze et al., 2019) , flood forecasting (Viterbo and Betts, 1999; Basara, 2001; Feng et al., 2015; Chifflard et al., 2017; Massari et al., 2018), hydrologic processes and water-balance studies (Hudson, 1988; Brocca et al., 2017; Salugin et al., 2018), (c) in agriculture, soil moisture affects crop production (Rossato et al., 2017; Peichl et al., 2018), irrigation scheduling (Schroder, 2006; Aguilar et al., 2015), pest detection and control (Koppenhöfer and Fuzy, 2007; Garrido-Juradoet al., 2011) (d) in forestry, soil moisture is essential for forest yield estimation (Mantovani et al., 2013), and forest fire prediction (Krueger et al., 2015; Jensen et al., 2018); (e) in soil science, soil moisture plays a significant role in erosion, mass movement, and landslides (Zhou et al., 2019; Abraham et al., 2020). Due to these widespread uses, soil moisture research has attracted the attention of numerous scientists worldwide.

Observations and soil moisture estimation are complex, time-consuming and expensive (Meng and Quiring, 2008). Moreover, it is spatially and temporally variable due to the heterogeneity of soil texture, topography, vegetation and climate (Kong et al., 2011). Therefore, various

applications requiring soil moisture information trust on model simulation are mainly driven by various meteorological factors in a climate system (Robock et al., 1998; Hagan et al., 2019). Understanding the relationship of soil moisture with meteorological parameters helps estimate and predict eco-hydrological processes such as evapotranspiration, groundwater recharge, etc. It also helps to estimate heat fluxes, which can lead to better weather forecasts. In addition, it is vital to suitably manage agricultural water requirements and support increases in crop productions. For revealing the relationship of soil moisture with other meteorological parameters, several models have been developed over time which is generally based on two types of approaches, viz. empirical and physically-based models. Empirical models are based on simple empirical algorithms using field observations in which water transfer in and out of the soil profile is adopted. This modelling approach has demonstrated versatility, but reliable predictions at the specific site require some calibration using observed soil moisture data.

Several other studies indicate that successful retrieval of soil moisture profiles requires mathematical models that include the dominant processes for the particular hydrological conditions (Walker et al., 2001). However, it is challenging to develop an ideal empirical model for soil moisture estimation due to complicated structural characteristics and meteorological factors. Therefore, this chapter deals with these objectives (1) to propose an empirical model for estimating soil moisture at different soil depths, (b) to check the workability of the proposed model at different soil depths, and (c) to simplify the proposed model for making it applicable at other sites and check its workability.

4.2 Model Development

4.2.1 Background

For this study, the study site's soil is considered a gigantic reservoir consisting of various layers. It is a common experience that soil moisture in the upper soil layers is significantly affected and replenished by single rainfall events, and it gets lost through evaporation, transpiration and percolation. In contrast, soil moisture in the deeper layers is primarily replenished by infiltration of water stored in the variable layers, groundwater, and mainly used by vegetation through transpiration. Soil moisture is also strongly coupled with temperature. It controls the partitioning of energy into sensible and latent heat fluxes and influences near-surface air temperatures (Huang et al. 1996). An increase or decrease in air temperature results in wind speed which plays a significant role in transporting the water vapour either evaporated from the soil or transpired from the plant into the atmosphere.

When a parcel of warm air moves over a wet surface, the temperature of the interacting surface decreases until the air surrounding the surface is saturated with moisture, which results in a temperature lower than ambient. The air surrounding the plant can approach saturation with water vapour transpired from the plant. With the reduction in air movement, the movement of saturated air mass away from the plant also reduces, resulting in a minimum vapour pressure deficit. A high wind speed results in more evapotranspiration and vice-versa. Rayner (2007), Roderick et al. (2007), Zheng et al. (2009), Tang et al. (2011), Liu et al. (2011, 2019), McVicar et al. (2012) and many others have reported that the decline in surface wind speed decreases the drying of soil moisture by reducing atmospheric evaporative demand. Various researchers also described that the increase in air temperature reduces the soil moisture in the top-soil layer (Jin and Mullens, 2014; Feng and Liu, 2015; Tang and Chen, 2017). Similar relations are observed by researchers between soil temperature and soil moisture (Al-Kayssi et al., 1990).

4.2.2 Model Formulation

(a) Water Balance Equation

The soil water balance equation for a soil column is considered as

$$\theta_t = \theta_{t-1} + F - ET - Per \tag{4.1}$$

where θ_t is the soil moisture of present-day, $\theta_{(t-1)}$ is the soil moisture of the previous day, F is the infiltration, ET is the evapotranspiration, Per is the percolation.

(b) Relation Between Soil Moisture and Rainfall

It is commonly experienced that when light rains fall on warm, parched soil, it gets converted into vapour within a few hours. On the contrary, the heavy rains of such a short duration for which runoff is very high results in a thorough wetting of upper layer soils and an addition to the soil moisture through infiltration. The infiltration is a complex process and varies non-linearly (Asgari et al., 2011; Pathak and Singh, 2016; Broadbridge et al., 2017), which can be described mathematically as

$$F = \alpha P^{\beta} \tag{4.2}$$

where α and β are coefficients varies between 0 and 1.

(c) Loss of Soil Moisture

The above discussion clarifies that soil moisture decreases on primary meteorological factors, viz., soil surface temperature, air temperature, wind speed, and downward percolation. The ET and the percolation are the two significant soil moisture loss components. Based on various permutations and combinations of different mathematical functions, the following loss components have been formulated.

(i) <u>ET component</u>

(a) Soil moisture loss (evapotranspiration component) due to wind is formulated as

$$ET_W = \ln(\lambda * U) \tag{4.3}$$

Where U - wind speed at 2 m and λ - coefficient.

The mathematical expression for representing the soil moisture loss (evapotranspiration component) due to air temperature is expressed as an exponential function as

$$ET_{AT} = \exp(\gamma * AT_{Max}) \tag{4.4}$$

Similarly, the soil moisture loss due to soil surface temperature can be modelled as

$$ET_{ST} = \exp(\delta * ST_{Max}) \tag{4.5}$$

ET_{AT} and ET_{ST} are evaporative (soil moisture loss) due to air temperature and soil surface temperature, respectively. $AT_{Max\ and}$ ST_{Max} are the maximum air soil surface temperature, respectively. γ, δ are the model coefficients.

The combined effect of wind speed, air and soil surface temperature on evapotranspiration is formulated as

$$ET = \ln(\lambda * U) + \exp(\gamma * AT_{MAx}) + \exp(\delta * ST_{MAx}) \tag{4.6}$$

(ii) <u>Percolation component</u>

Percolation is formulated as

$$Per = \exp(\mu * (\theta_{t-1} + F))$$

$$Per = \exp(\mu * (\theta_{t-1} + \alpha P^{\beta})) \tag{4.7}$$

Where $\theta_{(t-1)}$– Soil moisture of previous day, μ - coefficient

(d) Computation of soil moisture

By replacing the infiltration, evapotranspiration and percolation formulations in Eq. (8.1), the present-day soil moisture can be formulated as:

$$\theta_t = \theta_{t-1} + \alpha P^{\beta} - \ln(\lambda * U) - \exp(\gamma * AT_{Max}) - \exp(\delta * ST_{Max}) - \exp\left(\mu * \left(\theta_{t-1} + \alpha P^{\beta}\right)\right) \tag{4.8}$$

4.2.3 Model Calibration

The proposed empirical relation (Eq. (8.8)) is calibrated using observed rainfall, wind speed, maximum air temperature and maximum soil temperature data. For this chapter study, data of the Kanataal site from another project sponsored by MoES is also used here, along with the data of Nagini and Kumargaon. The study site Kanataal is located at 30^{o} 24' 53.08" N, 78^{o} 19' 17.98" E, altitude - 2590 m.a.s.l within the Henval watershed. Near-surface soil temperature (at a depth of 2 cm) is used as surface soil temperature due to the unavailability of surface soil temperature data. For the Kumargaon, Kanataal and Nagini sites, data from 13/02/2018 to 03/10/2018, 03/01/2018 to 31/05/2018 and 23/03/2016 to 31/03/2017 is used for model calibration.

4.2.4 Parameter Estimation

The Generalized Reduced Gradient (GRG) optimization technique which is a non-linear method, was used to optimize the parameters used in the proposed equation of soil moisture. GRG solver looks at the slope of the objective function as the decision variables alter and decides that it has touched an optimum solution when the partial derivatives equal zero. It is a simple, robust and trustworthy approach to model difficult non-linear systems (Moore and Jones, 2015). GRG solver stops if the absolute value of relative change in the objective function is less than the tolerance value for the last five iterations (Zakwan et al., 2017). Barati (2013) successfully used it to estimate the parameters of non-linear Muskingum models for flood routing. Zakwan et al. (2016) and Zakwan (2017) also used it and found it effective to obtain the parameter of infiltration equations.

Using this technique with appropriate bounds on parameters of the proposed equation, the objective function (RMSE) was optimized to obtain the optimal values of the parameters. The acquired set of parameters for different soil depths are given in table 4.1.

Table 4. 1: Obtained parameters at different soil depths

Parameters	Range	Soil depth								
		Kumargaon			Kanataal			Nagini		
		2 cm	6 cm	25 cm	2 cm	6 cm	25 cm	6 cm	15 cm	50 cm
α	0-1	0.747	0.655	0.500	0.585	0.303	0.109	0.721	1.000	0.532
β	0-1	0.380	0.390	0.252	0.513	0.695	0.657	0.361	0.355	0.000
λ	0-1	0.020	0.023	0.021	0.010	0.010	0.010	0.018	0.015	0.010
γ	0-1	0.000	0.000	0.001	0.100	0.010	0.062	0.006	0.000	0.062
δ	0-1	0.007	0.000	0.001	0.085	0.100	0.050	0.037	0.015	0.019
μ	0-1	0.070	0.073	0.100	0.043	0.032	0.031	0.037	0.039	0.031

4.2.5 Model Simplification

The obtained parameters in optimization for the same depth are averaged together to simplify the model and increase its field applicability, as shown in Table (4.2). Using these values of parameters in Eq. (8.8), the simplified equations for soil moisture estimation can be obtained as

For soil depth of 2 cm,

$$\theta_t = \theta_{t-1} + 0.666 * P^{0.446} - \ln(0.015 * U) - \exp(0.050 * AT_{Max}) - \exp(0.046 * ST_{Max}) - \exp(0.057 * (\theta_{t-1} + (0.666 * P^{0.446})))$$

(4.9)

For soil depth of 6 cm

$$\theta_t = \theta_{t-1} + 0.560 * P^{0.482} - \ln(0.017 * U) - \exp(0.005 * AT_{Max}) - \exp(0.046 * ST_{Max}) - \exp(0.048 * (\theta_{t-1} + (0.560 * P^{0.482})))$$

(4.10)

For soil depth of 25 cm,

$$\theta_t = \theta_{t-1} + 0.305 * P^{0.455} - \ln(0.016 * U) - \exp(0.031 * AT_{Max}) - \exp(0.026 * ST_{Max}) - \exp(0.065 * (\theta_{t-1} + (0.305 * P^{0.455})))$$

(4.11)

Table 4. 2: Average value of parameters at different soil depths

Parameters	Soil depth		
	2 cm	6 cm	25 cm
α	0.666	0.560	0.305
β	0.446	0.482	0.455
λ	0.015	0.017	0.016
γ	0.050	0.005	0.031
δ	0.046	0.046	0.026
μ	0.057	0.048	0.065

4.2.6 Performance Evaluation

For evaluating the performance of the proposed empirical relation, indices of agreement, namely, Coefficient of determination (R^2), Root Mean Square Error (RMSE), Mean Absolute Error (MAE) and Unbiased Root Mean Square Error (ubRMSE), are used, which can be described as

$$R^2 = \frac{\left[\sum_{i=1}^{N}\left(\theta_{Obs}-\bar{\theta}_{Obs}\right)\left(\theta_{Comp}-\bar{\theta}_{Comp}\right)\right]^2}{\sum_{i=1}^{N}\left(\theta_{Obs}-\bar{\theta}_{Obs}\right)_i^2\sum_{i=1}^{N}\left(\theta_{Comp}-\bar{\theta}_{Comp}\right)_i^2} \quad (4.12)$$

$$RMSE = \sqrt{\frac{1}{N}\sum_{i=1}^{N}\left(\theta_{Obs}-\theta_{Comp}\right)^2} \quad (4.13)$$

$$ubRMSE = \frac{1}{N}\sqrt{\sum_{i=1}^{N}\left(\left(\theta_{Obs}-\bar{\theta}_{Obs}\right)-\left(\theta_{Comp}-\bar{\theta}_{Comp}\right)\right)^2} \quad (4.14)$$

$$MAE = \frac{1}{N}\left[\sum_{i=1}^{N}\left|\theta_{Obs}-\theta_{Comp}\right|\right] \quad (4.15)$$

where, θ_{Obs} is the observed soil moisture, θ_{Comp} is the computed soil moisture, $\bar{\theta}_{Obs}$ is the mean of observed soil moisture, $\bar{\theta}_{Comp}$ is the mean of computed soil moisture, N is the total number of observations, and i is an integer varying from 1 to N.

4.3 Result and Discussion

4.3.1 Model Validation

For validation of the proposed model at the study sites of Kumargaon, Kanataal and Nagini, data from 16/10/2018 to 14/12/2019, 01/06/2018 to 31/12/2018 and 01/04/2017 to 09/08/2017

are used, respectively. For assessing the performance of the proposed empirical model, the coefficient of determination (R^2) is computed, which designates the total variance between the observed and the modelled data and ranges from 0 to 1. A perfect correlation is obtained if R^2 equals 1, whereas R^2 equals 0 indicate no fit. In between, higher values of R^2 show superior performance and decreasing values indicate a poor fit.

Table (4.3) shows the R^2 values obtained in calibration and validation for all the soil depths of the study sites. Figure (4.1) shows the R^2 between the observed and the predicted soil moisture for the Kumargaon site, which indicates that the proposed empirical equation is capable of computing the soil moisture in the upper layers of 2 cm and 6 cm with excellent performance associated with high R^2 value in calibration and validation. At the soil depth of 2 cm, R^2 for calibration and validation is 0.91 and 0.85, respectively, whereas, at the soil depth of 6 cm, R^2 for calibration and validation is 0.90 and 0.83, respectively. At the deeper soil depth of 25 cm, R^2 for calibration and validation is 0.73 and 0.62, respectively. Similar performance is obtained for the Kanataal site for the same soil depths as shown in figure (4.2).

Similarly, R^2 between the observed and the predicted soil moisture for the Nagini site is shown in figure (4.3). Here, it is observed that for the soil depth of 6 cm, R^2 for calibration and validation is 0.89 and 0.78, respectively. In contrast, at the soil depth of 15 cm, the R^2 for calibration and validation is 0.67 and 0.73, respectively. At the soil depth of 50 cm, R^2 for calibration and validation is 0.72 and 0.76, respectively. It can be noted that R^2 for calibration and validation decreases with the increase in soil depth which indicates the decreasing performance of the proposed empirical relation with the increasing soil depth.

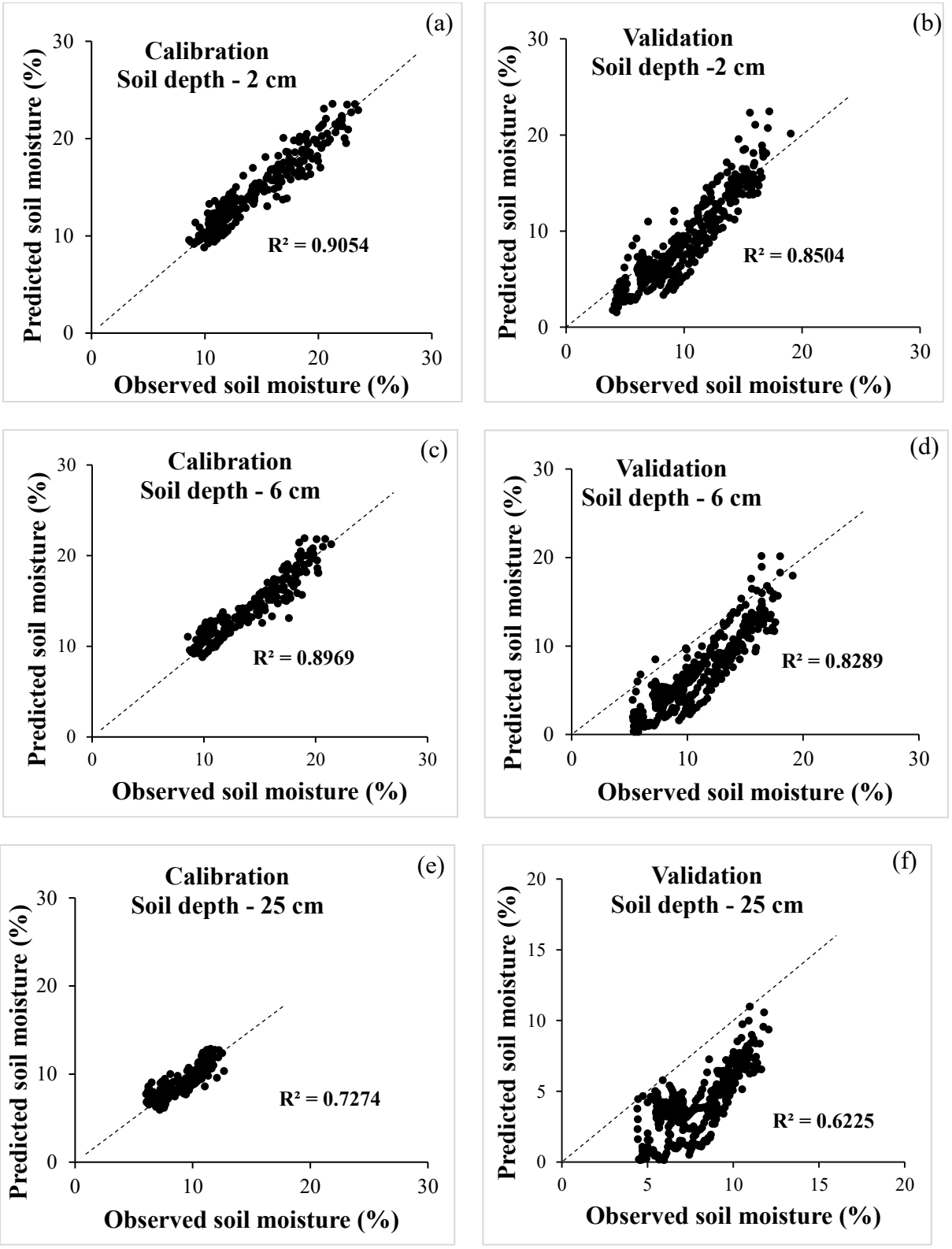

Fig. 4. 1 (a-f): Comparison of observed vs predicted soil moisture for different soil depths

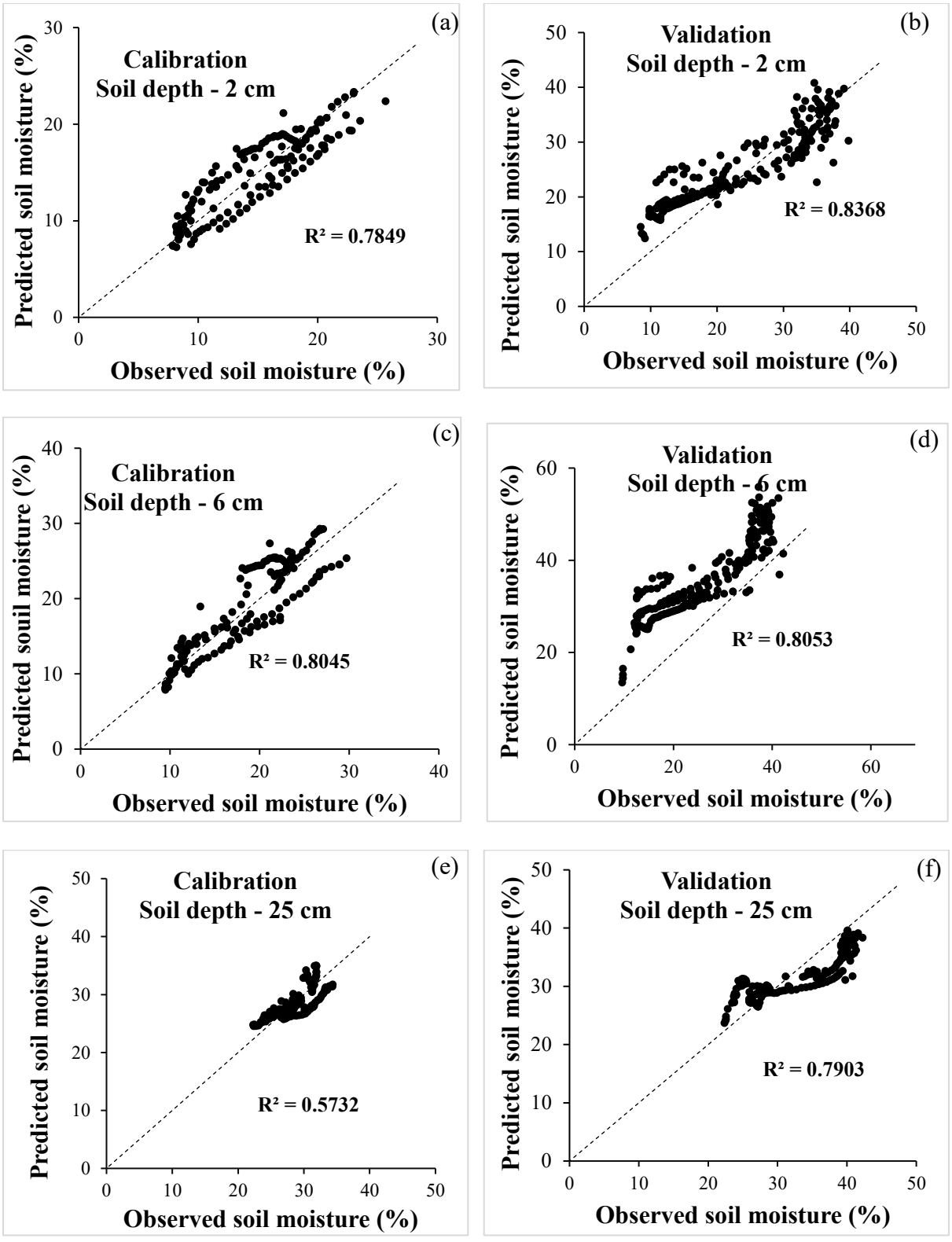

Fig. 4. 2 (a-f): Comparison of observed vs predicted soil moisture for different soil depths at Kanataal

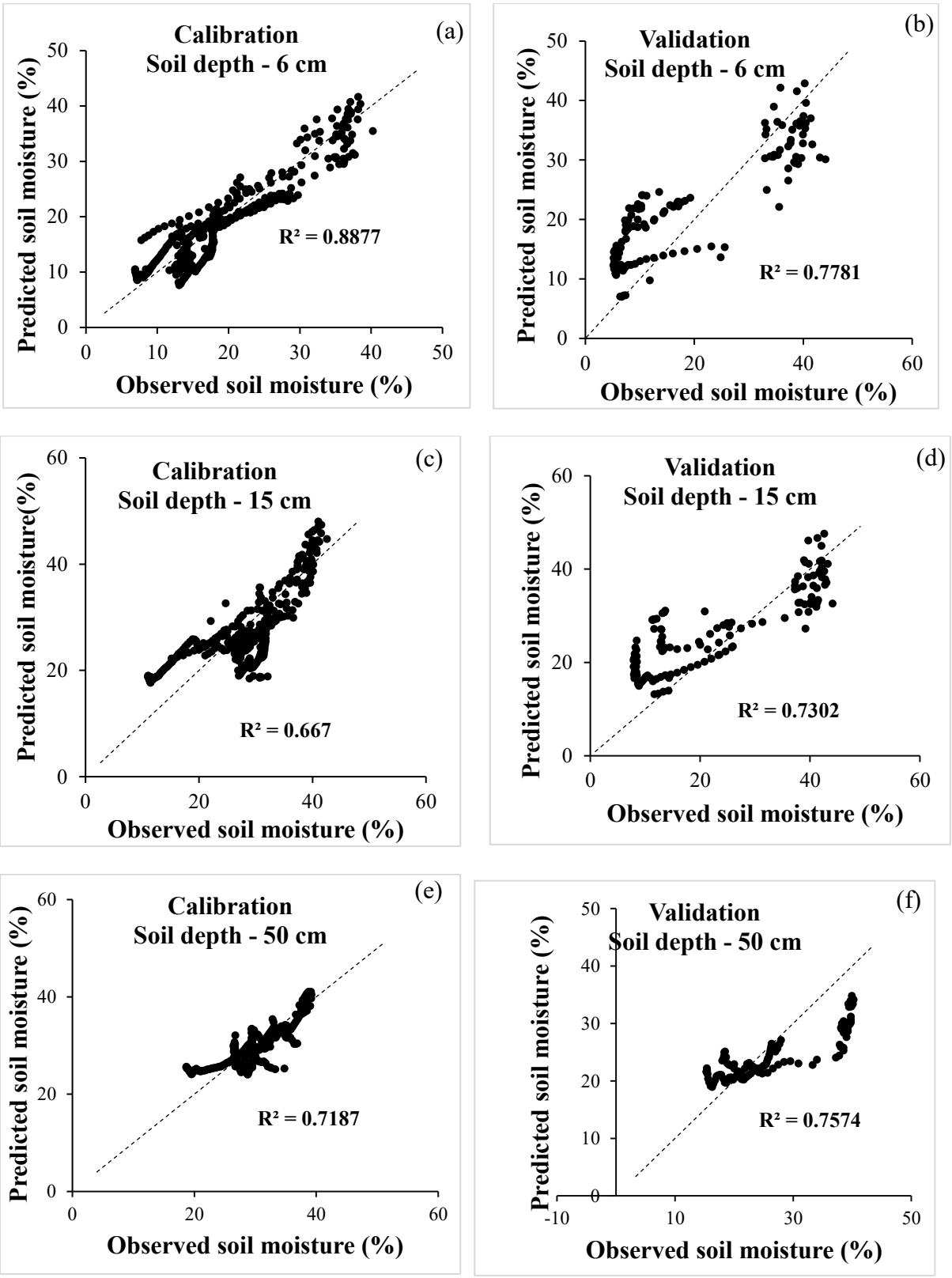

Fig. 4. 3 (a-f): Comparison of observed vs predicted soil moisture for different soil depths at Nagini

According to Ahmadisharaf *et al.* (2019), the R^2 criterion is unresponsive to additive and proportional variances between the predicted and observed values. Still, it is more sensitive to outliers than to the values near the mean, leading to a bias towards the extreme values. To overcome the discrepancies related to the use of R^2, alternative measures of performance, i.e. RMSE, provide an estimate of the error between the computed and observed data. The perfect fit between the observed and predicted values is described by its optimal value equal to 0, and increasing values indicate a poor fit.

RMSE has been computed for all the soil layers and sites under study, as shown in table 4.3. For the soil depth of 2 cm, 6 cm and 25 cm at Kumargaon, RMSE is found 1.22, 1.13 and 1.00 in calibration and 2.08, 4.23 and 3.97 during validation, respectively. For the similar soil depth at Kanataal, RMSE is found 2.08, 2.68 and 2.09 in calibration and 4.76, 10.76 and 3.46 during validation, respectively. Similarly, for the soil depth of 6 cm, 15 cm and 50 cm at Nagini, RMSE is found 2.96, 5.02 and 2.81 in calibration and 7.61, 8.23 and 2.81 during validation, respectively.

Table 4. 3: Performance measures of the model at different soil depths of the study sites.

Kumargaon								
Soil depth	**Calibration**				**Validation**			
	R^2	**RMSE**	**ubRMSE**	**MAE**	**R^2**	**RMSE**	**ubRMSE**	**MAE**
2 cm	0.91	1.22	0.77	0.93	0.85	2.08	1.19	1.70
6 cm	0.90	1.13	0.68	0.88	0.83	4.23	1.61	3.90
25 cm	0.73	1.00	0.54	0.80	0.62	3.97	1.41	3.70
Kanataal								
Soil depth	**Calibration**				**Validation**			
	R^2	**RMSE**	**ubRMSE**	**MAE**	**R^2**	**RMSE**	**ubRMSE**	**MAE**
2 cm	0.79	2.07	1.11	1.75	0.84	4.76	2.66	3.96
6 cm	0.80	2.68	1.48	2.23	0.81	10.76	4.18	9.92
25 cm	0.57	2.09	1.05	1.80	0.79	3.46	1.95	2.86
Nagini								
Soil depth	**Calibration**				**Validation**			
	R^2	**RMSE**	**ubRMSE**	**MAE**	**R^2**	**RMSE**	**ubRMSE**	**MAE**
6 cm	0.89	2.96	1.63	2.48	0.78	7.61	3.59	6.68
15 cm	0.67	5.02	2.56	4.32	0.73	8.23	4.94	6.54
50 cm	0.72	2.81	1.72	2.21	0.76	2.81	3.74	5.06

The obtained results indicate the satisfactory performance of the model at all the sites. It is also found here that the model performance decreases with the increasing soil depth.

4.3.2 Comparison of Model Simulation with Observed Time-series

The visual comparison of observed and predicted soil moisture at Kumargaon is shown in Figure (4.4), which indicates that the predicted and the observed values are very close to each other in the upper layers of 2 cm and 6 cm, whereas at the soil depth of 25 cm, many computed values are appearing far from the observed one. The obtained result is also supported by the Pearson correlation between the observed and computed values (calibration (0.95, 0.95 and 0.85) and validation (0.91, 0.84, and 0.65) for soil depth of 2 cm, 6 cm and 25 cm, respectively, which decreases with the increasing soil depth. Similar results are obtained for the Kanataal and Nagini sites, as shown in Figures (4.5) and (4.6), respectively. For Kanataal, Pearson correlation is found equal to (0.89, 0.90 and 0.76) in calibration and (0.91, 0.90 and 0.89) during validation for the soil depth of 2 cm, 6 cm and 25 cm, respectively, whereas for the Nagini site, Pearson correlation is found equal to (0.94, 0.82 and 0.85) in calibration (0.88, 0.86 and 0.87) during validation for the soil depth of 6 cm, 15 cm and 50 cm, respectively.

The effect of rainfall events is also shown in these figures, which highlight that the addition of a part of rainfall (infiltration) in the soil profile after rainfall events increases soil moisture immediately in the upper layers of 2 cm and 6 cm. In contrast, in the deeper layer of 15 cm, 25 cm and 50 cm, the immediate effect of these rainfall events is not visible. During the summer months (April - June), the small rainfall events increase the soil moisture in the upper layers (2 cm and 6 cm) only. The infiltrated water from these small events is not able to reach the deeper layers (15 cm, 25 cm and 50 cm) because infiltrated water percolates downward very slowly. Due to increased solar radiation and high temperature during summers, soil moisture depletes rapidly through evapotranspiration (Zhuo et al., 2017) and cannot reach the deeper layer. With the advancement of the southwest monsoon season during June-July, the frequency and magnitude of rainfall events increases, increasing soil moisture continuously. The infiltrated water percolates downward continuously and improves the soil moisture in the deeper layers of 15, 25 and 50 cm.

In the absence of rainfall events, soil moisture starts depleting due to air and soil temperature and wind speed. The effect of these meteorological variables is visible in all the layers and at all the study sites, highlighting that the depletion rate of soil moisture is faster in the upper

layers than in the deeper layer. The effect of meteorological variables decreases with the increasing soil depth, resulting in slower depletion of soil moisture in deeper layers.

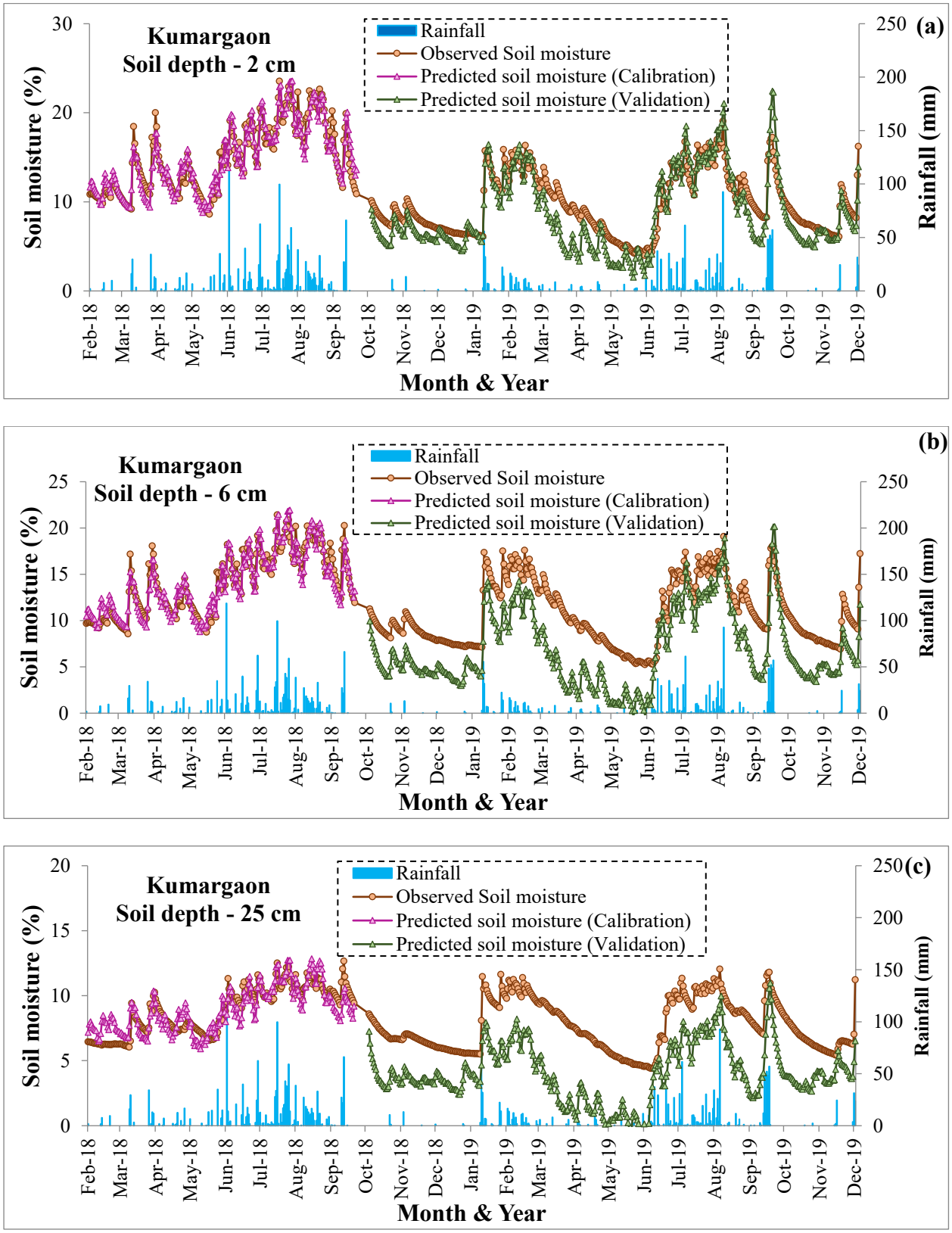

Fig. 4. 4 (a-c): Effect of rainfall on soil moisture at Kumargaon

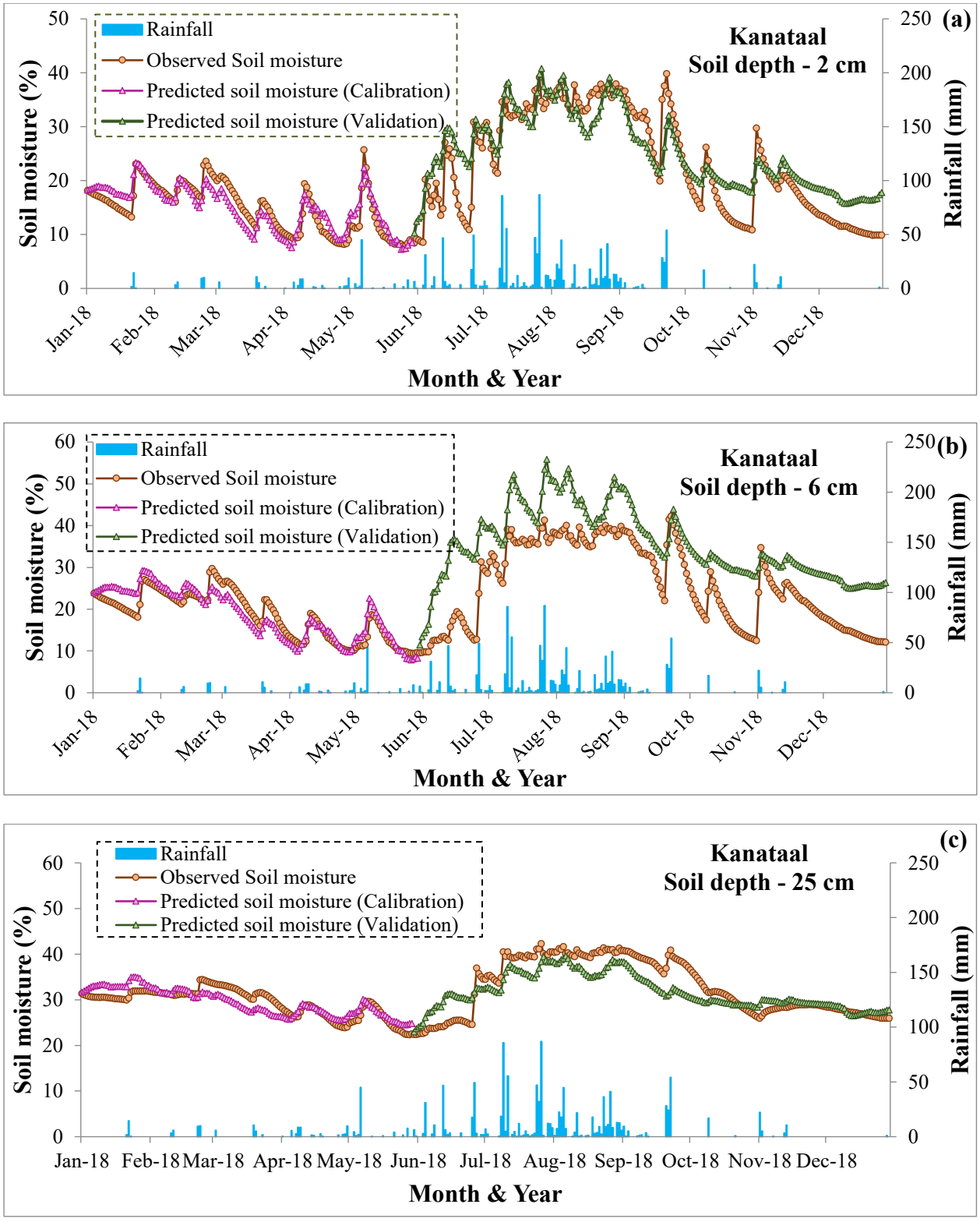

Fig. 4. 5 (a-c): Effect of rainfall on soil moisture at Kanataal

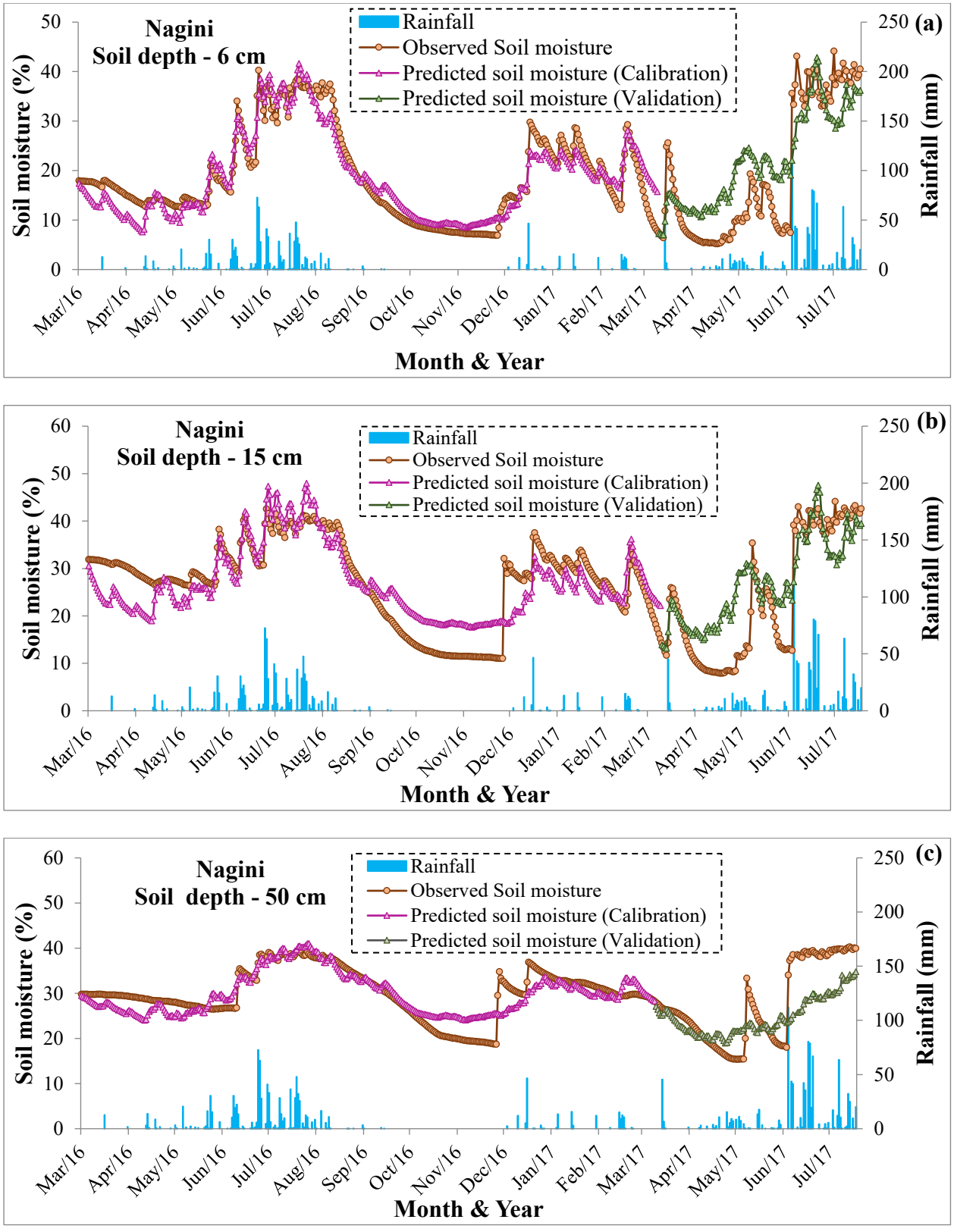

Fig. 4. 6 (a-c): Effect of rainfall on soil moisture at Nagini

Moriasi et al. (2015) stated that RMSE is sensitive to more significant errors. Therefore, to remove the discrepancies associated with RMSE, ubRMSE is computed for all the soil depths at all the sites under study (Table 4.3). At Kumargaon, ubRMSE is found equal to 1.19, 1.61 and 1.41 for the soil depths of 2 cm, 6 cm and 25 cm, respectively, whereas, for the similar soil depth at Kanataal, ubRMSE is found equal to 2.66, 4.38 and 1.95. Similarly, at Nagini, ubRMSE is found equivalent to 3.59, 4.94 and 3.74 for the soil depths of 6 cm, 15 c and 50 cm, respectively. Furthermore, to evaluate the performance of the proposed model, MAE between the observed and computed data is also calculated, which shows similar results at all the study sites, as shown in Table 4.3.

8.3.3 Performance Evaluation of Simplified Model

The simplified model (Eq. (4.9-4.11)) is tested using the data used for validation of the models, and the results are shown in figure (4.7). The obtained results indicated that the simplified models performed very well at Kumargaon for all the soil depths by depicting high R2 values, 0.86, 0.83 and 0.64 for the soil depths of 2 cm, 6 cm and 25 cm, respectively (Table 4.4). At Kanataal, the model performed very well only for the topmost layer of 2 cm with high R^2 (0.81) value. In contrast, for the deeper layers of Kanataal, the lower value of R^2 (0.50 for 6 cm and 0.33 for 25 cm) value indicates unsatisfactory performance. For the soil depth of 6 cm at Nagini, the model again performed well with high R^2 (0.81) value. Similar results are depicted by figure (4.8), which visually compares observed and predicted soil moisture.

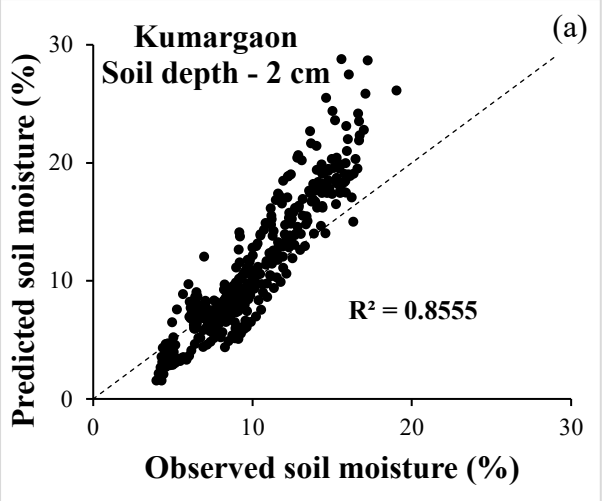
(a)
Kumargaon
Soil depth - 2 cm
Predicted soil moisture (%)
Observed soil moisture (%)
R² = 0.8555
0
10
20
30

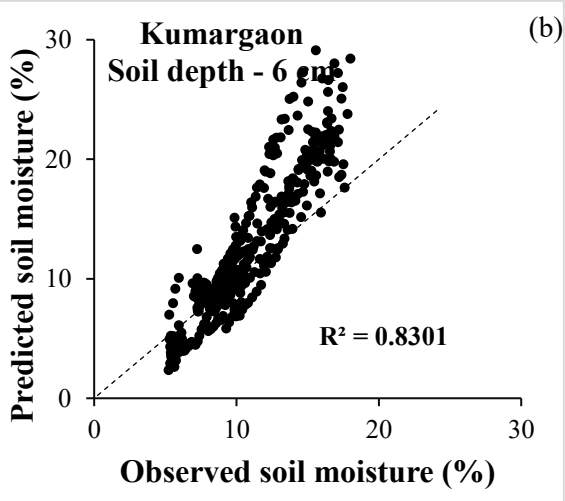
(b)
Kumargaon
Soil depth - 6 cm
Predicted soil moisture (%)
Observed soil moisture (%)
R² = 0.8301
0
10
20
30

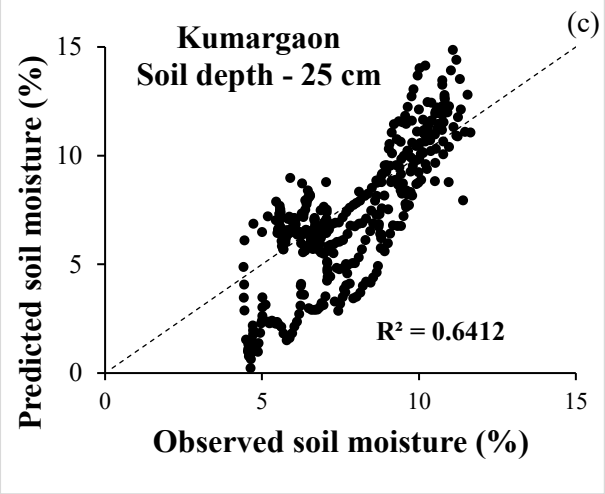
(c)
Kumargaon
Soil depth - 25 cm
Predicted soil moisture (%)
Observed soil moisture (%)
R² = 0.6412
0
5
10
15

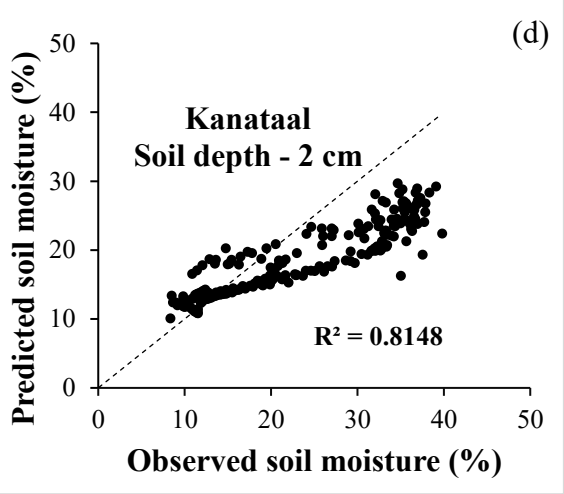
(d)
Kanataal
Soil depth - 2 cm
Predicted soil moisture (%)
Observed soil moisture (%)
R² = 0.8148
0
10
20
30
40
50

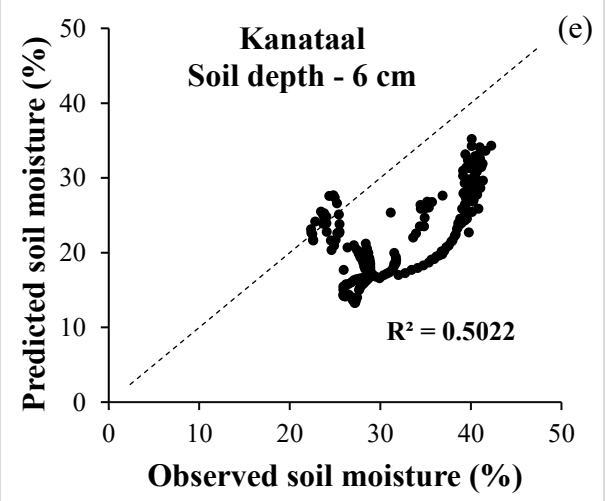
(e)
Kanataal
Soil depth - 6 cm
Predicted soil moisture (%)
Observed soil moisture (%)
R² = 0.5022
0
10
20
30
40
50

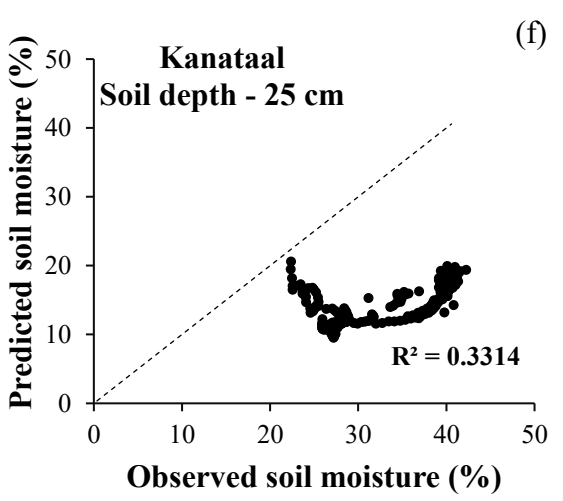
(f)
Kanataal
Soil depth - 25 cm
Predicted soil moisture (%)
Observed soil moisture (%)
R² = 0.3314
0
10
20
30
40
50

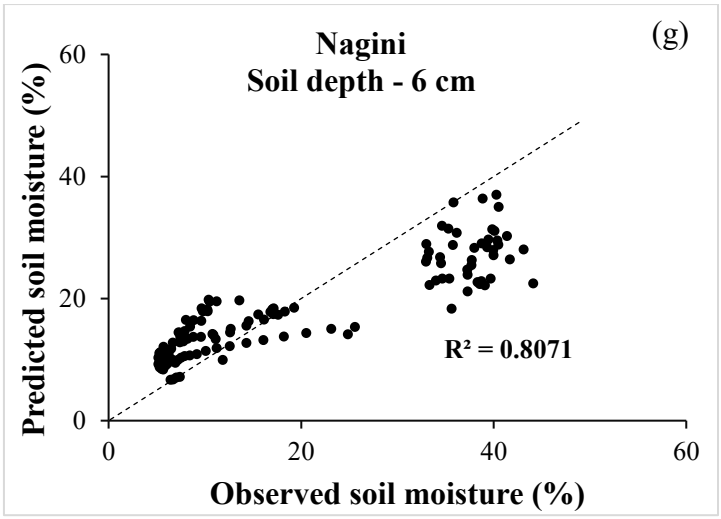

Fig. 4. 7 (a-g): Performance of simplified model for different soil depths

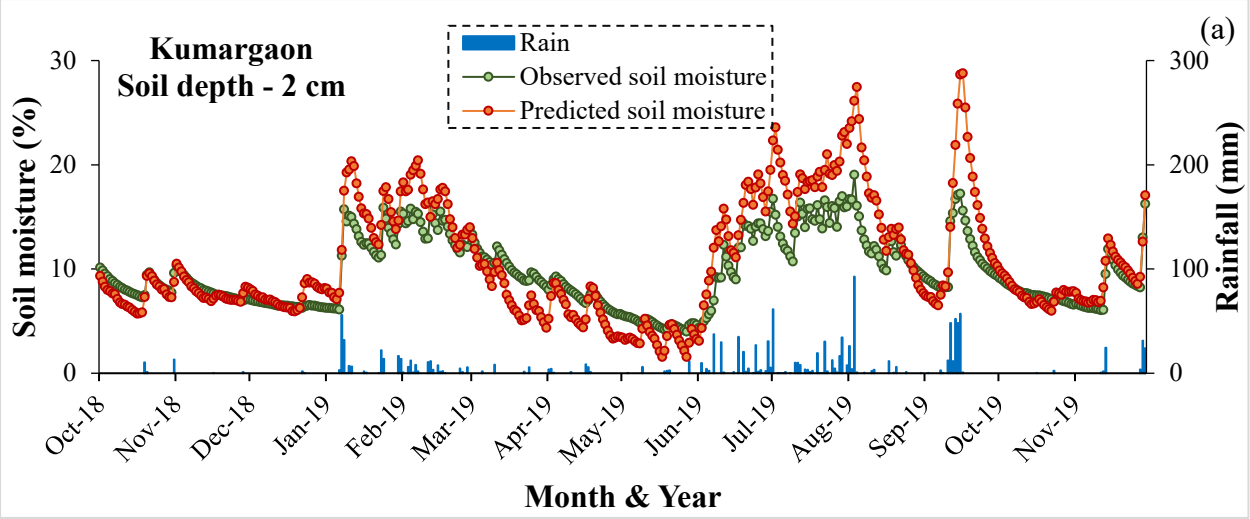
(a)
Kumargaon
Soil depth - 2 cm
Rain
Observed soil moisture
Predicted soil moisture
Soil moisture (%)
Rainfall (mm)
Month & Year
Oct-18
Nov-18
Dec-18
Jan-19
Feb-19
Mar-19
Apr-19
May-19
Jun-19
Jul-19
Aug-19
Sep-19
Oct-19
Nov-19

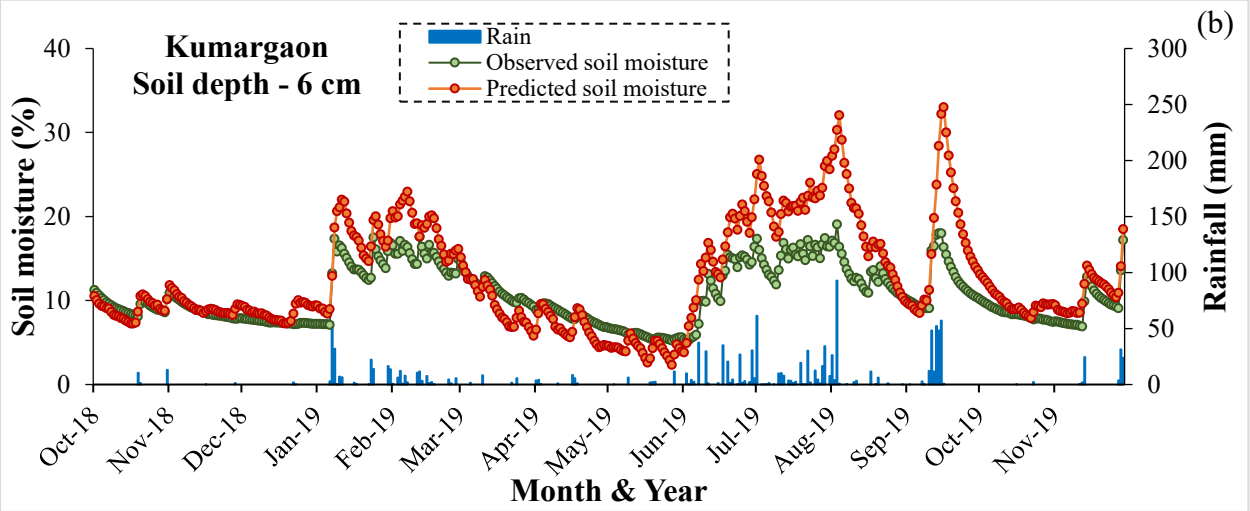
(b)
Kumargaon
Soil depth - 6 cm
Rain
Observed soil moisture
Predicted soil moisture
Soil moisture (%)
Rainfall (mm)
Month & Year
Oct-18
Nov-18
Dec-18
Jan-19
Feb-19
Mar-19
Apr-19
May-19
Jun-19
Jul-19
Aug-19
Sep-19
Oct-19
Nov-19

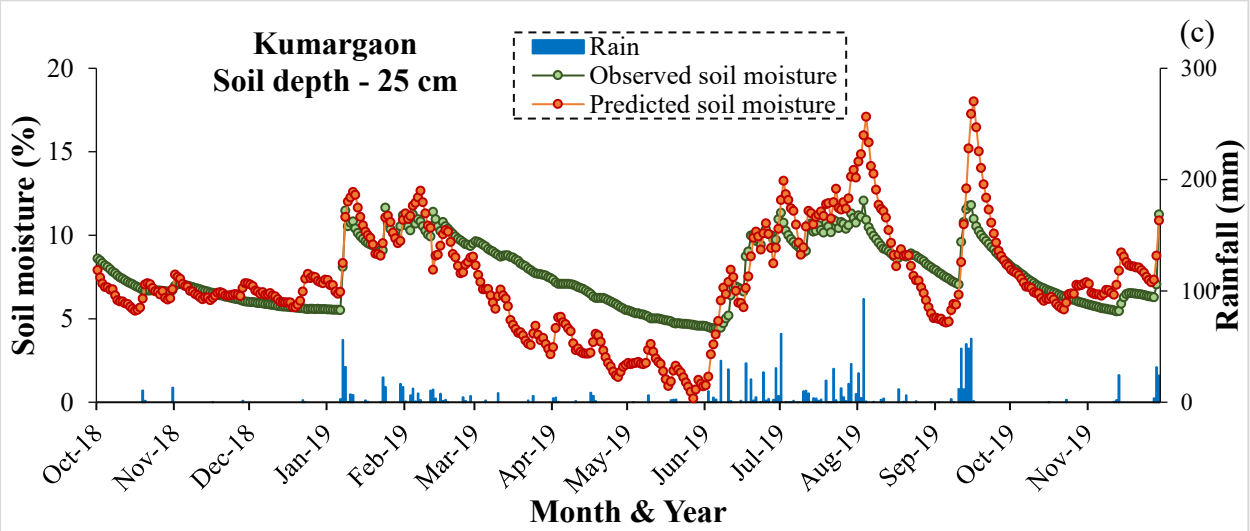
(c)
Kumargaon
Soil depth - 25 cm
Rain
Observed soil moisture
Predicted soil moisture
Soil moisture (%)
Rainfall (mm)
Month & Year
Oct-18
Nov-18
Dec-18
Jan-19
Feb-19
Mar-19
Apr-19
May-19
Jun-19
Jul-19
Aug-19
Sep-19
Oct-19
Nov-19

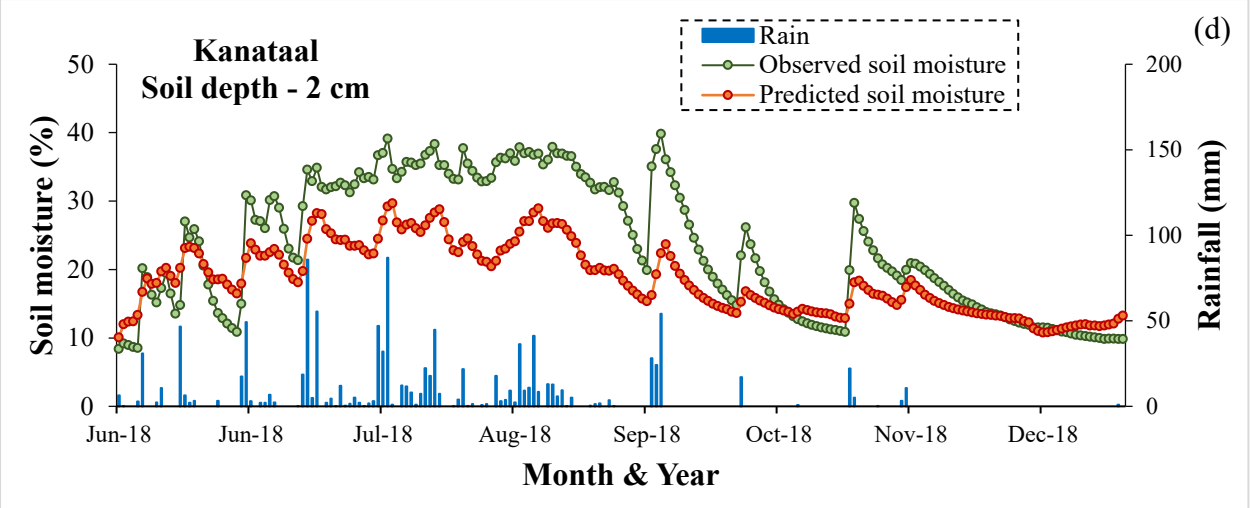
(d)
Kanataal
Soil depth - 2 cm
Rain
Observed soil moisture
Predicted soil moisture
Soil moisture (%)
Rainfall (mm)
Month & Year
Jun-18
Jun-18
Jul-18
Aug-18
Sep-18
Oct-18
Nov-18
Dec-18

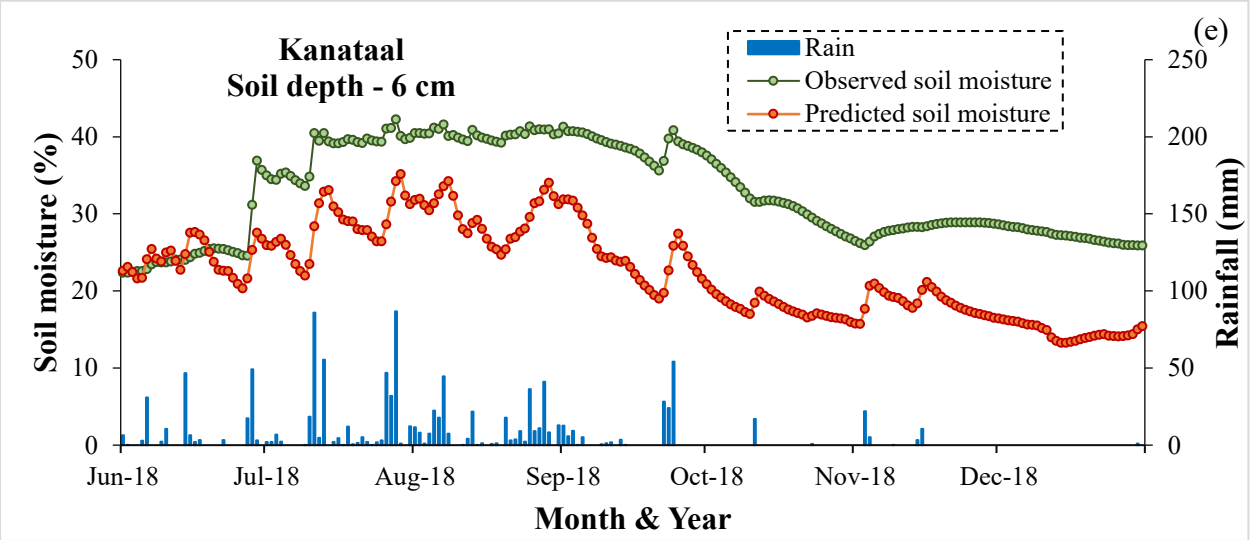
(e)
Kanataal
Soil depth - 6 cm
Rain
Observed soil moisture
Predicted soil moisture
Soil moisture (%)
Rainfall (mm)
Month & Year
Jun-18
Jul-18
Aug-18
Sep-18
Oct-18
Nov-18
Dec-18

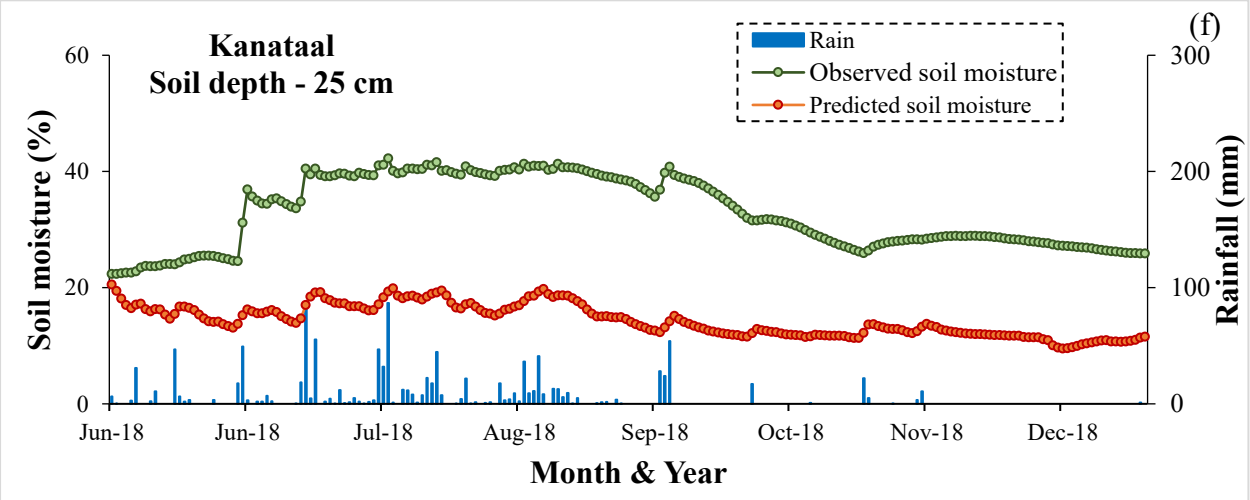
(f)
Kanataal
Soil depth - 25 cm
Rain
Observed soil moisture
Predicted soil moisture
Soil moisture (%)
Rainfall (mm)
Month & Year
Jun-18
Jun-18
Jul-18
Aug-18
Sep-18
Oct-18
Nov-18
Dec-18

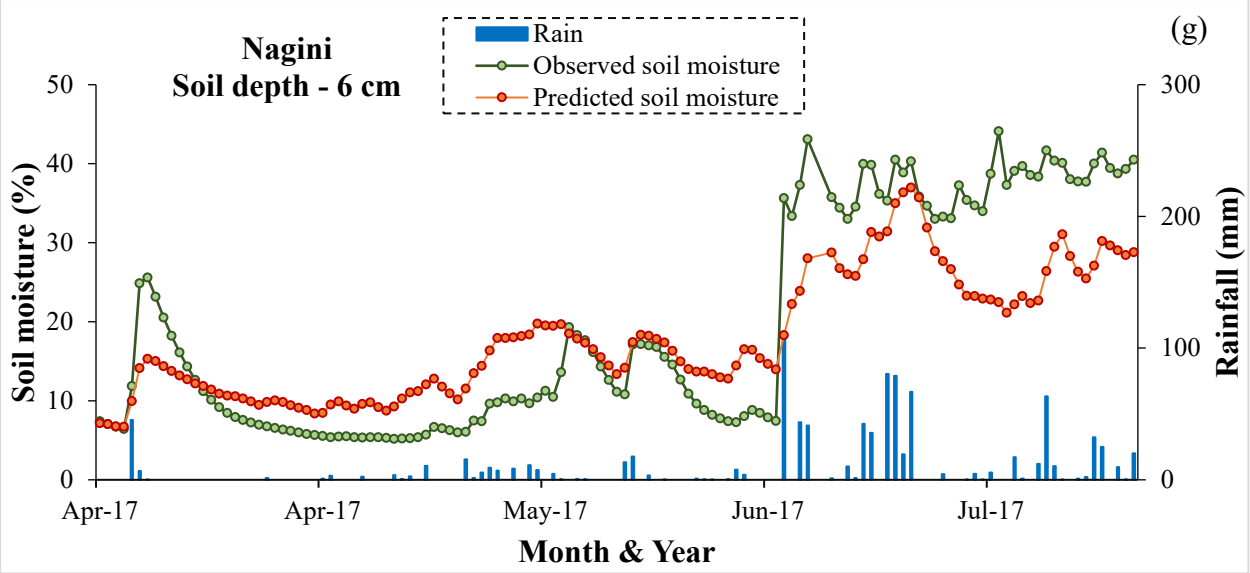

Fig. 4. 8 (a-g): Comparison of observed and predicted soil moisture for different soil depths

Table 4. 4: Performance measures of the simplified models at different soil depths of the study sites

Site	Soil depth	R^2	RMSE	ubRMSE	MAE
Kumargaon	2 cm	0.86	2.90	2.03	2.07
	6 cm	0.83	3.96	2.83	2.78
	25 cm	0.64	2.07	1.32	1.59
Kanataal	2 cm	0.82	7.28	4.34	5.85
	6 cm	0.50	11.24	4.19	10.42
	25 cm	0.33	19.10	5.12	18.40
Nagini	6 cm	0.81	7.74	4.57	6.25

Furthermore, to evaluate the performance of the simplified model, RMSE between the observed and predicted data is also computed, which reveals that at Kumargaon, RMSE is 2.90, 3.96 and 2.07 for the soil depth of 2 cm, 6 cm and 25 cm, respectively (Table 4.4). The performance of the simplified model at Kanataal is found comparatively inferior by depicting a high RMSE value of 7.28, 11.24 and 19.10 for the soil depth of 2 cm, 6 cm and 25 cm, respectively. For the soil depth of 6 cm at Nagini, high RMSE (4.57) is obtained, indicating the inferior performance of the simplified model. Similar results are obtained when the simplified model is tested using the ubRMSE and MAE criteria, as shown in Table 4.4.

8.4 Concluding Remarks

An empirical model is formulated using available parameters in this study, i.e. rainfall, wind speed, air temperature, and near soil surface temperature. This model was calibrated and validated using the Kumargaon, Kanataal and Nagini sites in the lesser Himalayan region. The results indicated the best performance of the model at Kumargaon with high R^2 in calibration and validation. These results are further supported by lower values of RMSE, ubRMSE, MAE and Pearson's correlation coefficient for this site. The model performed good at the other two sites of Kanataal and Nagini, but the results are comparatively inferior to Kumargaon.

Furthermore, this model is simplified using the averaged values of optimized parameters and tested using the data used for validation. The study results indicated that the simplified model also performed best at Kumargaon for all the soil depths with high R^2 values, which are obtained as 0.86 for 2 cm, 0.83 for 6 cm and 0.64 for 25 cm, whereas for the similar soil depths at Kanataal, the performance was good only for the topmost layer of 2 cm with a high R^2 value of 0.82. For the deeper soil layers at Kanataal, lower values of R^2 (0.50 for 6 cm and 0.33 for 25 cm) indicates relatively average performance. Once again, the simplified model performed well at the site of Nagini with high R^2 (0.81) value for the soil depth of 6 cm. It is also found that the model's performance decreases with increasing soil depth which indicates that the effect of meteorological variables decreases with the increasing soil depth.

Chapter 5

5.0 SOIL MOISTURE MODELING: MACHINE LEARNING

5.1 General

Climate change is one of the world's most significant problems, having the potential to create regular or long-term droughts in many parts of the globe (Le Houérou, 1996). Rainfall that is infrequent or unexpected and increased evapotranspiration due to rising temperatures result in lower soil moisture (Kingston, 2009). Soil moisture is essential for the growth of practically all arable crops across the world, affecting everyone from tiny subsistence farmers to major industrial, agricultural businesses. Irrigation is one of the world's most significant freshwater uses, as it is necessary for many locations to keep soil moisture sufficient for crops (Frenken, 2012). Adequate soil moisture is essential for crop development and production maximisation. Crop failure due to insufficient soil moisture is a threat to farmers' livelihoods and jeopardises the strength of the food supply chain, which is critical in today's world.

Physical models were formerly used to forecast future soil moisture levels. Physical models or basic regression models might be used to estimate soil moisture using weather predictions by using precipitation and temperature as inputs. These models tended to be inaccurate and forecast on a low-resolution, offering coarse temporal scale generalisations of soil moisture. Artificial intelligence's arrival in the field of hydrology has prompted researchers to look into more areas with large amounts of data in order to improve accuracy. To predict soil moisture, one study (Prakash S. S., 2018) used a Recurrent Neural Network (RNN), Multiple Linear Regression (MLR), and Support Vector Machines (SVM).

In comparison to other models, MLR fared well in this investigation, having the lowest mean square error (MSE). Another study (Prakash S. &., 2020) used a shallow neural network with MLR and SVM to forecast soil moisture one, two, and seven days in advance. The findings indicate that a shallow neural network outperforms other models. Other studies (Ji, 2017) used a multilayer neural network with many neurons to predict soil moisture. It was able to generalise soil moisture development, demonstrate good generalisation, and improve forecast precision by 9.1%. Another study (Cai, 2019) found that deep neural network (DNN) performance was better than MLP and SVM. Machine learning and deep learning have substantially improved model performance, allowing for fine-scale climate forecasts such as

nowcasting (Bromberg, 2019), which delivers on-the-spot predictions within very short timescales. However, projecting further into the future in a helpful fashion remains a challenge. With the use of recurrent neural networks (RNNs) (Rumelhart, 1986)and long-short term memory RNNs (LSTMs) (Hochreiter, 1997), deep learning has recently become a technique that excels in the field of time series prediction. (Alibabaei, 2021) the study shows CNN-LSTM model outperformed other models while predicting soil moisture.

With these studies in mind, the objective of the study is to forecast soil moisture in the Lesser Himalayan area using meteorological and soil moisture data using deep hybrid models CNN-LSTM and RNN-LSM. Four quantitative standard statistical metrics, such as RMSE, R2, MAPE, and EN-S, were used to assess the model's performance. This research aims to develop the best model for predicting soil moisture with few errors and more accuracy.

5.2 Materials and Methods

5.2.1 Description of Model

As of now, very few studies have focused on predicting soil moisture using machine learning, with most examples being artificial neural networks (ANN) and extreme learning machines (ELM). This study evaluated two prominent deep learning-based hybrid ANN techniques to model the sub-surface soil moisture in a Himalayan environment. Long Short Term Memory (LSTM) based Recurrent and Convolutional Neural networks were developed and tested against the actual field level observations.

5.2.2.1 Recurrent Neural Network (RNN)

A feed-forward neural network (FFNN) with internal memory is known as a Recurrent Neural Network (RNN). (Medsker, 2001)RNN is recurrent since it executes the same functions for each data input, whereas the current input is dependent on the previous computation. The output is replicated and returned to the recurrent network when it is created. It uses the current input and output and what it has learned from past input to make a decision. RNNs can process sequences of inputs using their internal state (memory) rather than feed-forward neural networks. All of the inputs in other neural networks are unrelated to one another. In an RNN, however, all of the inputs are interconnected, and figure 5.1(A) shows the architecture of RNN.

5.2.2.2 Long Short Term Memory (LSTM)

LSTM networks are a revised form of RNNs that make it simpler to recall data from the past (Abbes, 2019). They're well-suited to categorising, analysing, and forecasting time series with

indefinite time delays. Back-propagation is often used to train the model. In an LSTM network, three gates are present (figure 5.1(B)):

1. Input gate – discover which value from input should be used to modify the memory.
2. Foregate gate – discover what details are to be discarded from the block.
3. Output gate – the input and the memory of the block is used to decide the output.

5.2.2.2 Convolutional Neural Network (CNN)

A feed-forward neural network is a convolutional neural network (Albawi, 2017). Convolutional neural networks include the same properties as standard neural networks, including input layers, hidden layers, and output layers. The input of the layer of convolution is the output of the preceding layer of convolution or pooling. They do, however, have certain distinct properties, such as pooling layers, complete connection layers, and so on. The number of hidden layers of a convolutional neural network is more than that of a regular neural network, demonstrating the neural network's capabilities to some extent. The bigger the number of hidden layers, the more information it can extract and recognise from the input.

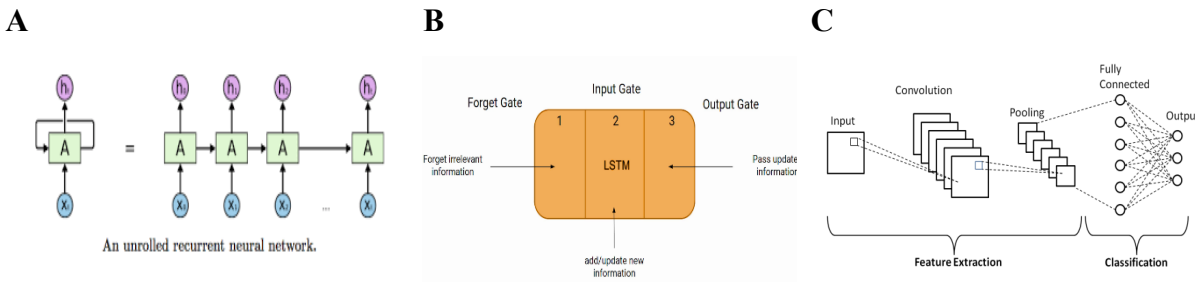

Fig. 5. 1: Architecture of (A) RNN, (B) LSTM, and (C) CNN

5.3 Data Analysis and Pre-Processing

The data of three Automatic Weather Station (AWS) viz. Kumargaon (AWS1), Kanatal (AWS2), and Nagini (AWS3), located in the lesser Himalayan catchment, have been used for soil moisture prediction through deep learning-based hybrid models. Meteorological data obtained from AWSs consists of daily rainfall, average wind speed at 2m above ground, and maximum air temperature. The AWS sites are also instrumented with the TDR probes; hence the daily data of maximum soil temperature and soil-moisture data consisting of daily volumetric water content (VWC) at a soil depth of 2cm, 25cm, and 50cm were used. Input parameters for the selected models consist of rainfall, average wind speed at 2m, maximum air temperature, maximum soil temperature at a depth of 2cm, soil moisture at a depth of 2cm, and one-day previous soil moisture at a depth of 25cm and 50cm. Output feature for the model

consists of present-day soil moisture at 25cm and 50cm depth. Missing data were identified, using Decision Tree Regressor (Vateekul, 2009,) as an estimator of iterative Imputer function the data were corrected to have uninterrupted time-series. Observation obtained from three sites was divided into training and testing sets to train the models. Table 5.1 gives the information on data distribution used for training and testing the DL models.

Table 5. 1: Description of data used for training and testing the DL models

Station	AWS1	AWS2	AWS3
Total no. of observation (Period)	652 (02/13/2018 to 12/14/2019)	363 (01/3/2018 to 12/31/2018)	362 (01/05/2018 to 01/01/2019)
No. of Training observation (Period)	526 (02/13/2018 to 08/05/2019)	290 (1/3/2018 to 10/19/2018)	289 (01/05/2018 to 10/20/2018)
No. of Testing observation (Period)	132 (08/06/2019 to 12/14/2019)	73 (10/20/2018 to 12/31/2018)	73 (10the /21/2018 to 01/01/2019)

5.4 Prediction Model Evaluation

As shown by (Moriasi, 2007) and (Dawson, 2007), mean evaluate the overall performance of machine learning models, we use the coefficient of determination (R^2), root mean square error ($RMSE$), mean absolute percentage error ($MAPE$) and Nash-Sutcliffe efficiency coefficient (E_{N-S}) as the standard quantitative statistical performance evaluation measures.

$$R^2 = \left(\frac{\frac{1}{n}\sum_{i=1}^{n}(y_o(i)-\overline{y_o})(y_f(i)-\overline{y_f})}{\sqrt{\frac{1}{n}\sum_{i=1}^{n}(y_o(i)-\overline{y_o})^2 * \sqrt{\frac{1}{n}\sum_{i=1}^{n}(y_f(i)-\overline{y_f})^2}}} \right)^2 \quad (5.1)$$

$$RMSE = \sqrt{\frac{1}{n}\sum_{i=n}^{n}(y_f(i) - y_o(i))^2} \quad (5.2)$$

$$MAPE = \frac{1}{n}\sum_{i=1}^{n}\left|\frac{y_f(i)-y_o(i)}{y_o(i)}\right| \times 100 \quad (5.3)$$

$$E_{N-S} = 1 - \frac{\sum_{i=1}^{n}(y_f(i)-y_o(i))}{\sum_{i=1}^{n}(y_o(i)-\overline{y_o})} \quad (5.4)$$

Where $y_o(i)$ and $y_f(i)$ are, respectively, the observed and predicted soil moisture and $\overline{y_o}$, $\overline{y_f}$ denote their means, and *n* is the number of data points considered.

5.5 Development of Models

The models used in this study have been programmed using Keras API of Tensorflow framework and Sickit-learn. To train the models, the dataset has been divided into training, and

testing sets mentioned earlier in section 5.2.2. It has been shown that RNN lacks in processing very long sequences and has gradient vanishing and exploding problems. In order to overcome these problems, LSTM is combined with the RNN model. In the RNN-LSTM model, 14 days of data were considered to predict the subsequent day data. The CNN-LSTM architecture involves using CNN layers for feature extraction on input data combined with LSTM to support sequence prediction (Table 5.2).

Table 5. 2: Range of tested hyper-parameter in designing CNN-LSTM and RNN-LSTM predictive models through Trial-and-Error Method

Tested range of model Hyper- Parameters		
Model	Model Hyper-parameter	Search space for optimal Hyper Parameters
CNN-LSTM	Filter 1	60,40
	Filter 2	30,15
	Filter 3	10
	LSTM 1	20
	LSTM 2	10
	Dense	20,10
	Epochs	200,500,1000
	Activation function	ReLu
	Optimiser	Adam
	Learning rate	0.01,0.02
	Batch size	12,20
RNN-LSTM	LSTM 1	60,40
	LSTM 2	30,20
	LSTM 3	15,10
	Epochs	200,500,1000
	Activation function	ReLu
	Optimiser	Adam
	Batch size	20

Table 5.3 gives information about the various combination of hyper-parameters used for the two models at different AWS datasets. A different combination of hyper-parameters was adopted to reduce the over-fitting and under-fitting of the models while training.

Table 5. 3: Optimally selected hyper-parameter for AWS1

Optimally Selected Hyper- Parameters		
Model	Model Hyper-parameter	Search space for optimal Hyper Parameters
CNN-LSTM	Convolution Layer 1 (filters)	60
	Activation function	ReLu
	Kernel Size	3
	Convolution Layer 2 (filters)	30
	Activation function	ReLu
	Kernel Size	2
	Convolution Layer 3 (filters)	20
	Activation function	ReLu
	Kernel Size	2

	Drop out rate	0.3
	MaxPooling-Pool_size	2
	LSTM Layer 1(cell)	20
	Activation function	ReLu
	LSTM Layer 2 (cell)	10
	Activation function	ReLu
	Drop out rate	0.2
	Dense (neurons)	20
	Activation function	ReLu
	Optimiser	Adam
	Learning rate	0.02
	Epochs	200
	Loss function	MSE
	Batch_size	12
RNN-LSTM	LSTM_layer 1	60
	Drop-out rate	0.3
	Activation function	ReLu
	LSTM layer 2	30
	Drop-out rate	0.2
	Activation function	ReLu
	LSTM layer 3	15
	Drop-out rate	0.1
	Activation function	ReLu
	Optimiser	Adam
	Loss function	MSE
	Learning rate	0.01
	Batch size	15
	Epochs	200

Table 5.3 also gives information on the architecture of CNN-LSTM and RNN-LSTM models for the AWS1 region. ReLu stands for Rectified Linear Units, and MSE stands for Mean Squared error (Sharma, 2017).

5.6 Results and Discussion

The daily soil moisture data at depths of 25 cm and 50 cm from three AWS in Kumargaon, Kanatal, and Nagini in the lower Himalayan area were used to create more acceptable models for predicting future daily soil moisture. All of the models, as mentioned earlier, are generated based on a comparison of the same amount of training and testing datasets, respectively. At the same time, the quantitative standard statistical performance assessment measure is used to evaluate the performance of the various models developed. The residual between actual and anticipated soil moisture is measured by $RMSE$, while the mean absolute percentage error of the forecast is measured by $MAPE$. $E_{(N-S)}$examines the model's ability to forecast soil moisture values away from the mean, whereas R^2 analyses the linear correlation between actual and predicted soil moisture.

From Table 5.4, it can be observed that the R2 value of the CNN-LSTM model is in the range of 0.99 - 0.856, whereas the RNN-LSTM model range is 0.95 - 0.69, which depicts that the performance of the former is nearly 20% accurate than the later one. It can be observed that RMSE and MAPE of the CNN-LSTM model predict 90%, 4.12% less error, respectively, compared to others after considering the average of all the sites.

Table 5. 4: Forecasting performance indices of models

Model	CNN-LSTM				RNN-LSTM			
Performance indices	R^2	$RMSE$	$MAPE$ (%)	$E_{(N-S)}$	R^2	$RMSE$	$MAPE$ (%)	$E_{(N-S)}$
ASW1 at a depth of 25 cm	0.96	0.541	4.3	0.911	0.92	0.503	3.4	0.903
ASW1 at a depth of 50 cm	0.934	0.814	3.7	0.896	0.954	1.64	9.8	0.579
ASW2 at a depth of 25 cm	0.885	0.463	1.3	0.828	0.687	2.372	9.5	-4.99
ASW2 at a depth of 50 cm	0.875	0.605	1.8	0.389	0.706	0.347	0.8	0.214
ASW3 at a depth of 25 cm	0.992	1.794	7.3	0.956	0.69	5.748	21.2	0.542
ASW3 at a depth of 50 cm	0.856	2.362	6.1	0.657	0.853	2.044	4.5	0.757

CNN-LSTM **RNN-LSTM**

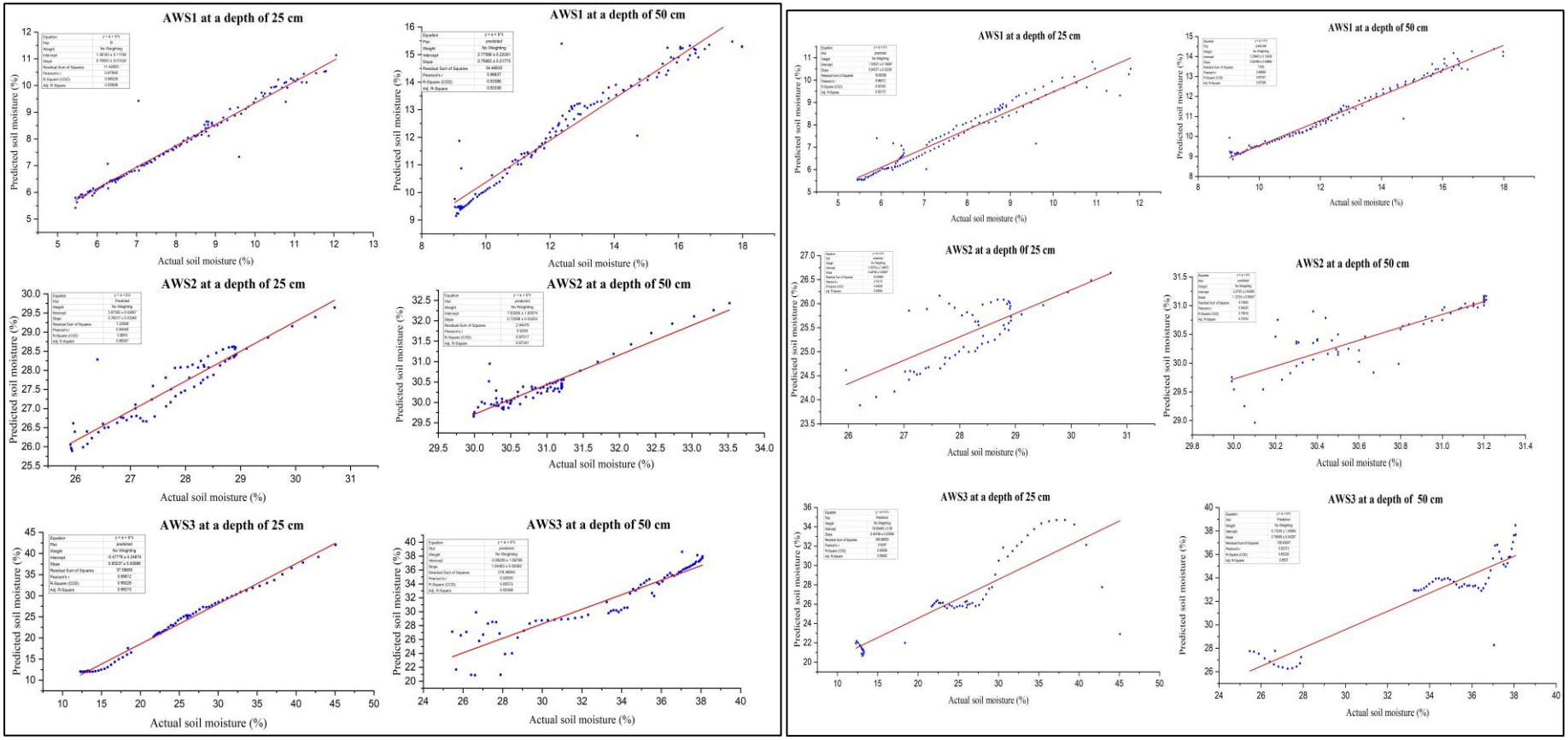

Fig. 5. 2: Scatter plot showing performance of CNN-LSTM and RNN-LSTM at given sites and depths

CNN-LSTM **RNN-LSTM**

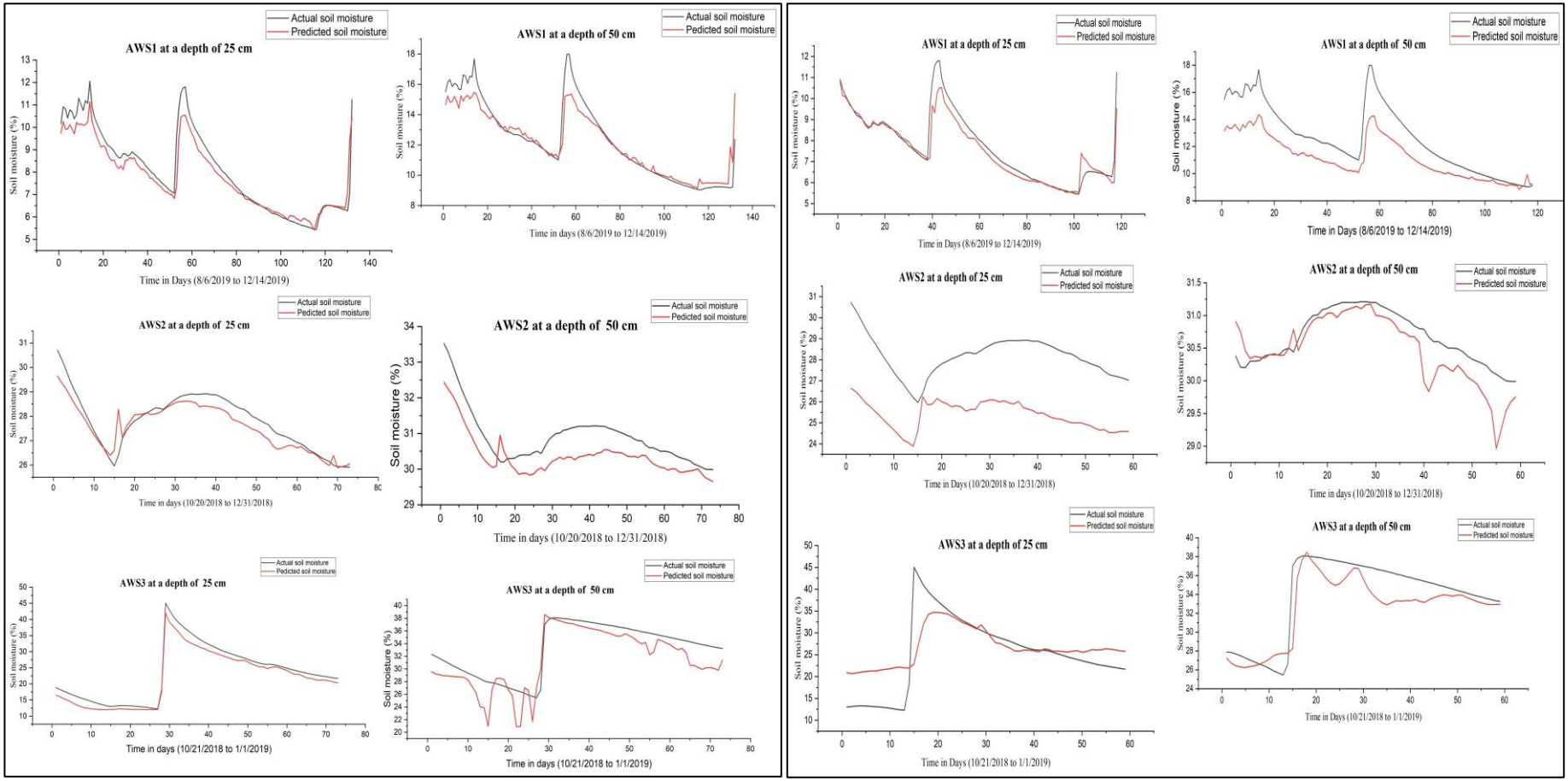

Fig. 5. 3: Time series performance of CNN-LSTM and RNN-LSTM at given sites and depths

Figure 5.2 and 5.3 shows the plot of actual and predicted soil moisture at 25 cm and 50 cm depth of given sites. It is observed that for some sites, the RNN-LSTM model has predicted with high error in terms of negative value and shows its inefficiency. Hence the results from this study assure that the CNN-LSTM model can be used to obtain a promising prediction. (Vateekul, 2009,)

5.7 Concluding Remarks:

In the study, two deep learning hybrid models based on long-short term memory, namely, CNN-LSTM and RNN-LSTM, were developed and tested to model the sub-surface soil moisture at three stations located in a Lesser Himalayan catchment. The developed models were trained and tested for two depths (25cm and 50cm) with the meteorological data monitored at each of the three stations. The study shows that a deep learning algorithm can accurately estimate soil moisture in the lower Himalayan basin. When comparing the CNN-LSTM model to the RNN-LSTM model, we found that the quality of the prediction by CNN-LSTM is superior. The model may be used in any other agricultural forecast system with modest changes and fine-tuning. Although this research is still in its early stages, the results are pretty encouraging. As a result, this work can pave the way for several new research avenues.

Chapter 6

6.0 GLACIO HYDROLOGICAL MODELING USING SPHY MODEL

6.1 Description of SPHY model

The SPHY model is a conceptual, continuous-time, raster-based spatially distributed leaky bucket-type water balance model that can simulate the behavior of glaciers and their interaction with the hydrological system at a regional or watershed scale. It requires a large number of input parameters varying widely in space and time while transforming input into output. It is a freely available model that is useful especially in mountainous areas despite the data scarcity, complexity and variability of the region for understanding the impacts of climate change on glacier dynamics, water resources, and downstream communities (Van Vliet et al., 2012, Lutz et. al, 2014; Terink et al, 2015). The SPHY model combines best components of existing widely used simulation models viz. SRM, VIC, SWAT, SWAP, HydroS, PCR – GLOBWB, SWAP, HIMSIM. SPHY glacio-hydrological models typically integrate various components such as glacier mass balance, ice melt, snow accumulation and melt, surface runoff, groundwater flow, and streamflow routing. An overview of SPHY model is represented in the Figure 6.1.

The model is based on physical principles and incorporate data on topography, climate, land cover, digital elevation model (DEM), soil properties and other relevant factors to simulate the complex interactions between glaciers and the hydrological cycle. SPHY operates at flexible scales viz. local, regional and global, accounting for relevant terrestrial hydrological processes. The tool can be used in water resource assessment, planning, management and decision-making policies. Major concept of SPHY is mass conservation and hence, simulates the dynamic behaviour of the glaciers. Therefore, SPHY can be used for assessing the potential effects of glacier retreat on water availability, hydropower generation, agriculture, and other socio-economic aspects in regions dependent on glacier meltwater. They also aid in predicting changes in flood and drought patterns resulting from alterations in glacier contributions to river flow. SPHY also includes lake module and erosion module enabling erosion studies. The model provides great adaptability depending on the spatial relevance of hydrological processes.

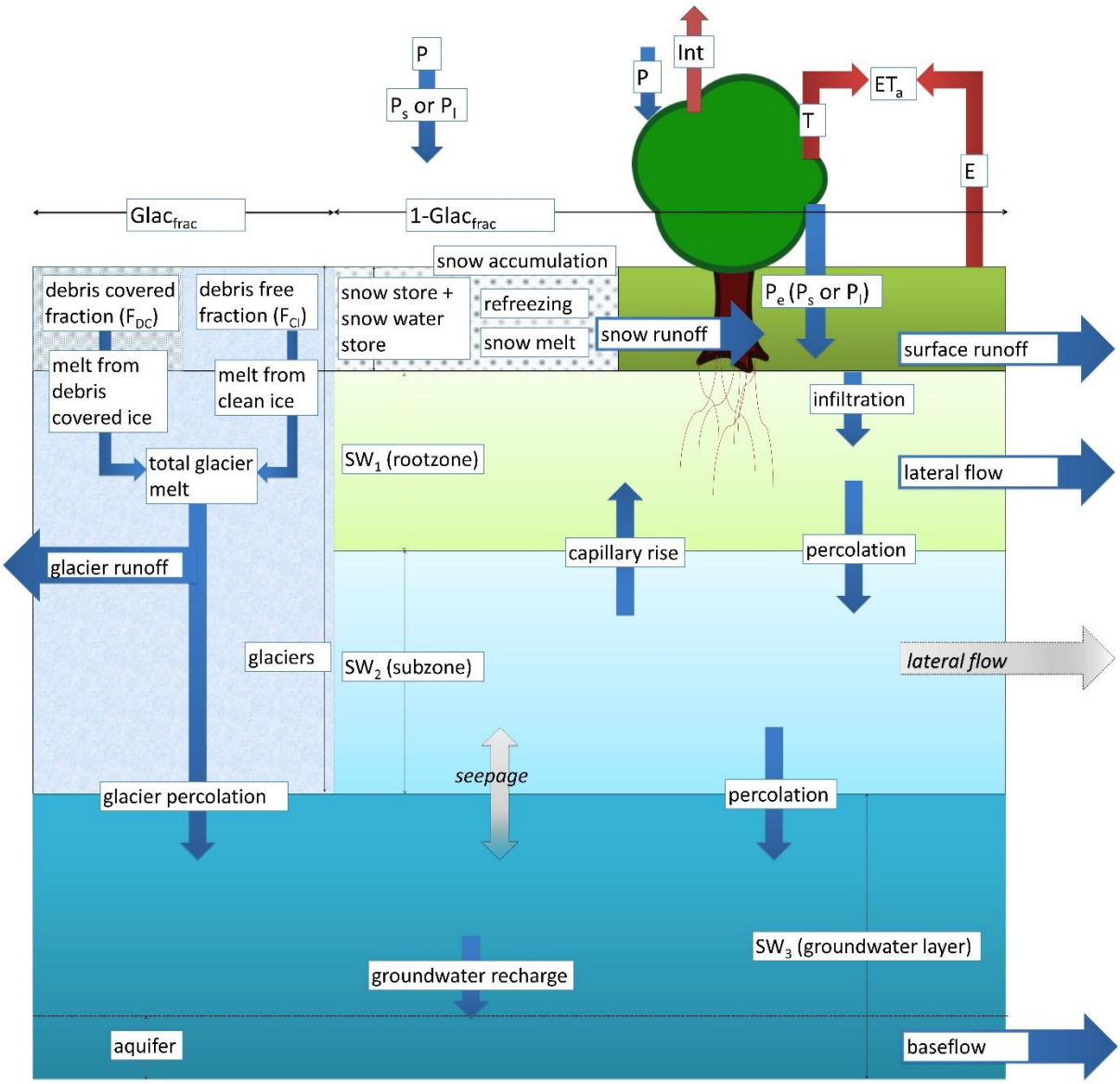

*source: sphy.readthedocs.io/en/latest/concepts.html

Fig. 6. 1: Overview of SPHY model

SPHY model requires spatial data like DEM, LULC, soil, glacial cover and meteorological data. Since SPHY is grid-based model, optimal use of remote sensing data and other global data is possible. The DEM of the study area was downloaded from https:// search.earthdata.nasa.gov, where elevation data at 30 m resolution acquired through SRTM is available for the globe. The Land Use data derived using the SENTINEL image was downloaded from the ESRI land cover explorer, https://livingatlas.arcgis.com/landcoverexplorer. The image is then projected into proper projection same as the DEM having the same datum using ArcGIS. The land use land cover

map of Henval watershed shown in Fig. (6.2). The other required inputs for glacio-hydrological modeling were prepared using the Hindu-Kush Himalaya database in the SPHY pre-processor. However, to obtain comprehensive and current data on glacial extends and their characteristics, the glacial dataset in the Hindu Kush Himalaya database in SPHY Preprocessor is updated with the latest version of the Randolph Glacier Inventory Version 7 (RGI 7.0) (RGI Consortium, 2017). The land cover map was further utilized to prepare a crop coefficient table with the corresponding crop coefficient values derived from literature.

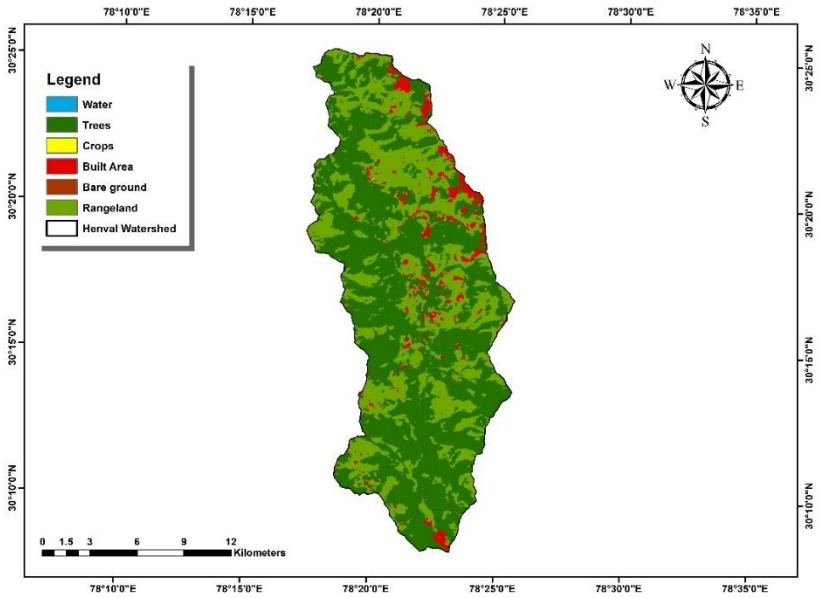

Fig. 6. 2: LULC classes map of Henval watershed

The meteorological and hydrological data required for the study at Henval watershed was procured from the AWS tower installed in Nagani village for the time being. Hence, the SPHY model was first set for the Henval sub-catchment with the outlet at Jijali-Devnagar and then, upscaled for the Henval basin with outlet at Shivapuri. The base map of the Henval sub-catchment within the Henval watershed is shown in Fig. 6.3.

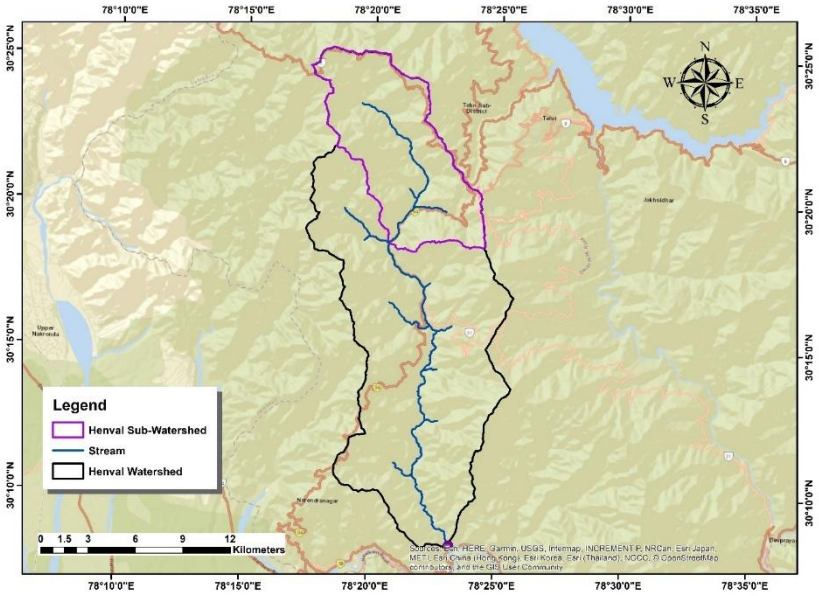

Fig. 6. 3: Base map of Henval sub-watershed

Precipitation and temperature in-situ datasets for Henval sub-watershed were obtained from the AWS stations of NIH. The in-situ meteorological data were used to find the best alternative datasets for the respective location amongst the various satellite and reanalysis datasets.

The daily discharge for the study was obtained from the broad crested compound rectangular-rectangular weir constructed at the outlet of Henval stream at Jijali-Devnagar and an automatic water level recorder installed across the Henval river at the same outlet. The cross-sectional diagram of the broad crested rectangular-rectangular weir is shown in Fig. 6.4. A compound rectangular-rectangular broad crested weir for monitoring of discharge was constructed, and its discharge can be calculated using the following equation

$$Q_t = \frac{2}{3} C_{rd1} \sqrt{2g} (2b_1) h_1^{3/2} + \frac{2}{3} C_{rd2} \sqrt{2g} b_2 h_2^{3/2}$$

$$C_{rd} = \frac{0.611 + 2.23(\frac{B}{b} - 1)^{0.7}}{1 + 3.8(\frac{B}{b} - 1)^{0.7}} + \frac{0.075 + 0.011(\frac{B}{b} - 1)^{1.46}}{1 + 4.8(\frac{B}{b} - 1)^{1.46}} \frac{h}{P}$$

Where, C_{rd}= discharge coefficient of the rectangular weir; g= gravitational acceleration; b = weir length; h = water head on the weir crest; B = channel width and P = weir height.

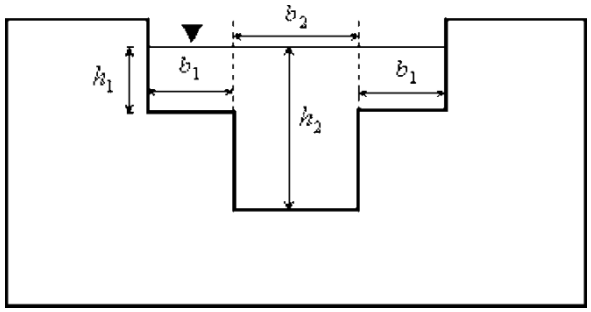

Fig. 6. 4: Cross-section of the compound rectangular-rectangular broad crested weir.

6.2 Model set up

The SPHY model was set up using the QGIS-SPHY interface. SPHY pre-processor was used to delineate the watershed and create the sub-basins. The additional datasets viz. DEM, land use, rivers, slope, and soil characteristics required for the SPHY model were generated using the Hindu–Kush Himalaya database in the SPHY pre-processor. A crop coefficient table comprised of crop coefficient values of different land classes was prepared referring to the literature. Furthermore, meteorological forcing was also done in the SPHY pre-processor using the datasets identified as the best alternative to in-situ data on a daily time scale based on bilinear interpolation with a lapse rate of -0.0065 ºC/m elevation for the temperature data (Terink et. al, 2015b).

The SPHY model was run to estimate runoff for the Henval sub-watershed initially from January 2016 to December 2018. The outputs were available as time series and map series data.

6.3 Model Simulation

The SPHY modelling concepts for studying the hydrology of glaciated watersheds along with the relevant governing equations have been expounded in the manual.

6.3.1 Computation of precipitation forms

Precipitation is calculated on a daily time step at each defined grid cell capturing the spatio-temporal variability in snowfall mass balancing (Singh. Et. al, 2023). Depending on the critical temperature, SPHY models precipitation as either rain (liquid) or snow (solid) for every cell. Vegetation on the ground intercepts the precipitation and causes partial or whole evaporation (Terink et. al, 2015).

6.3.2 Calculation of Evapotranspiration

Despite the energy-based Penman-Monteith method being the sole standard method for calculating reference evapotranspiration, due to the high input data requirements SPHY model utilizes a simpler, temperature-based approach of modified Hargreaves equation to calculate reference evapotranspiration and further, calculates potential evapotranspiration using the single crop coefficient approach (Allen et al., 1998; Terink et al, 2015). Kc for each land class in the study area was derived from the literature and taken as constant throughout the simulation period.

6.3.3 Quantification of snow processes

Dynamic snow storage is simulated for each cell and when snow accumulates or melts, the snow storage is updated for each cell at a daily time step considering precipitation, snow melt and refreezing of rainfall and snowmelt within the snowpack. The easy approach of the Temperature Index Model with varying degree-day factors based on the empirical relationship between melt and air temperature has been used to simulate daily potential snowmelt.

DDF_S is the degree day factor for snow, which is a calibrating parameter. However, the snow storage at the end of the previous day is a limiting factor for the actual snowmelt. The snow storage from the previous day is updated to the current day with respect to the actual snowmelt and the snow accumulation of the day t. Snow accumulation accounts for both the solid precipitation and refreezing of rainfall and snow melt stored within the snowpack.

The maximum of meltwater that can freeze within the snowpack depends on the thickness of snow storage and a calibrated parameter namely water storage capacity. The water storage capacity of the snowpack represents the capacity to refreeze the snow melt within the snowpack and is defined as the total water equivalent of snowmelt in mm that can freeze per water equivalent of snow in the snow storage in mm.

Based on the assumption in SPHY, snow melting and accumulation are limited to the grid-cell fraction designated as the non-glaciated land surface. The total snow storage comprises the snow storage along with the meltwater within it that can freeze again. However, the glacier module incorporates snow falling on glaciers. Snow runoff is generated when the air temperature surpasses the melting point and the snowpack is unable to hold any more meltwater.

6.3.4 Evaluation of Glacier Processes

Glaciers are assumed to be melting surfaces covering each glacierized grid cell completely or partially. The melting rates of clean ice and debris-covered glaciers vary necessitating separate spatial maps of both kinds of glaciers as model input. A degree-day modeling approach was adopted to differentiate the melt rates of clean and debris-covered glaciers with individual calibrated degree-day factors. The total glacial melt per grid cell is the sum of individual contributions from the debris-free glacier and debris-covered glacier with respect to the fractional glacier cover.

The glacial melt contributes to runoff as a quick direct runoff component and a slow component where it percolates to the groundwater layer, eventually becoming baseflow, which is defined by a calibrated parameter namely the glacial melt runoff factor.

6.3.5 Computing Soil Water Balance

With two upper soil storages- root zone and sub-zone layers- and third groundwater storage, the soil column structure is comparable to VIC (Liang et al., 1994, 1996) with surface runoff, lateral flow, and base flow serving as the respective drainage components. The water balance of each layer is given by:

$$SW_{1,t} = SW_{1,t-1} + Pe_t - ET_{a,t} - RO_t - LF_{1,t} - Perc_{1,t} + Cap_t$$

$$SW_{2,t} = SW_{2,t-1} + Perc_{1,t} - Perc_{2,t} - Cap_t$$

$$SW_{3,t} = SW_{3,t-1} + Gchrg_t - BF_t$$

Where, SW_t and SW_{t-1} are the soil water content on the days t and t-1, respectively, Pe_t is the effective precipitation on day t, $ET_{a,t}$ is the actual evapotranspiration on day t, RO_t is the surface runoff on day t, LF_t is the lateral flow from the soil layer on day t, $Perc_t$ is the percolation from the layer to the layer beneath on day t, Cap_t is the capillary rise to the layer from the layer below on day t, $Gchrg_t$ is the groundwater recharge consists of both glacial melt percolation and percolation to the third layer of soil on day t and BF_t is the base flow on day t. The subscript 1,2,3 represents the first layer or the root zone, the second layer or the subzone and third layer or the groundwater, respectively. All the components are in mm.

5.3.6 Estimating actual evapotranspiration

The resulting soil moisture after surface runoff is vulnerable to evapotranspiration, depending on the soil characteristics and fractional vegetation cover. The actual evapotranspiration is assumed to rely on the stresses due to the non-optimal conditions viz. water excess and water deficit on the potential evapotranspiration captured as reduction parameters which is calculated based on Feddes equation as elaborated by Terink et al. (2015).

5.3.7 Computing surface runoff

A portion of the liquid precipitation infiltrates the soil, while the remaining is transformed into surface runoff. SPHY assumes surface runoff as Hewlettian runoff based on the saturation of the first soil layer.

5.3.8 Calculating lateral flow

The remaining moisture contributes to river discharge as base flow from the groundwater layer and lateral flow from the first soil layer. SPHY considers only that water surpasses field capacity as contributing to lateral flow and is calculated at the hill slope outlet according to Sloan and Moore. However, the catchments with a time of concentration greater than one day lag a portion of lateral flow in reaching the main channel on the same day of generation. This implies that, even in the unlikely event that no lateral flow is formed in time step t, lateral flow from earlier time steps can be generated indefinitely.

5.3.9 Quantifying percolation

An approach similar to the SWAT model where the percolation from a layer is assumed to occur only when the water content surpasses the field capacity of that layer while the layer beneath is still unsaturated (Neitsch et al., 2009). Percolation occurs from the first to second soil layer and the second to third soil layer.

5.3.10 Computing baseflow

The glacier melts that percolates and the water that percolates together eventually contribute to groundwater recharge. An approach similar to SWAT has been adopted to compute groundwater recharge considering the time lag caused by the depth of the groundwater table and soil characteristic. However, baseflow occurs only when the water stored in the groundwater layer exceeds a threshold and is calculated similarly to SWAT assuming a linear correlation between the rate of change in water table height and the variation in base flow. A

calibrated parameter namely the baseflow recession coefficient is used to represent the baseflow response to the variations in groundwater recharge with a value ranging from 0 to 1 where higher value represent areas having rapid response to groundwater recharge.

5.4.11 Quantifying total routed runoff

The total of surface runoff (RO), lateral flow from the first soil layer (LF_1), baseflow (BF), snow runoff (SRo), and glacier runoff (GRo) is the cell-specific total runoff that becomes available for routing. The surface runoff and lateral flow components are combinedly termed as rainfall runoff (RRo). All the terms are in mm.

$$QTot = RRo + SRo + GRo + BF$$

The PCRaster-supported SPHY Preprocessor QGIS plugin was used to define a river network based on DEM to route QTot through a flow direction network for retrieving river discharge. A basic flow accumulation routing scheme was performed where the accumulated amount of water that flows out of the cell into its neighboring downstream cell is calculated using the flow direction network as the sum of the specific runoff generated in the cell and the accumulated specific runoff from the upstream cells. (Terink et. al, 2015). However, a calibrated flow recession coefficient accounted for flow delay due to channel friction ranging from 0 to 1 where the lower values of Kx attribute to a fast-responding catchment.

5.3 Sensitivity Analysis, Calibration and Validation of Model

A sensitivity analysis was carried out to identify the most relevant model parameters for the study. Parametrization has been done on a quarterly and seasonal basis with respect to the simulated discharge of the final year of the model run. The change in hydrograph and the change in the trend of average discharge for each simulation were carefully analyzed and the observations for Henval watershed are tabulated in Table 6.1. Parameter sensitivity for annual, quarterly and seasonal averages was plotted. Parameters with the maximum difference in the average discharge corresponding to a 50% increase and a 50% decrease in the value were ranked and the most sensitive parameters were chosen. The ranking of the parameters based on their effect on a quarterly, annual, and seasonal basis for the Henval watershed are represented in Table 6.2.

Calibration and validation were carried out based on the observed discharge from the study area on a daily time step. The approach used for calibration and validation is the minimization of error between the observed and simulated outputs. The calibration was carried out as a trial-

and-error process by manually adjusting the model parameters relevant to the hydrological behavior of the study area. The parameters affecting the model performance were selected based on the results of sensitivity analysis. The model was calibrated for the period of 01/01/2016 –31/12/2018 (3 years) for the Henval sub-watershed. The knowledge of model concepts and river basin characteristics smoothened the process of calibration, which was otherwise a computationally demanding task. The calibration of the model was performed using the observed discharge data by adjusting the most sensitive parameters in the range as shown in Table 6.3 for Henval catchment and their corresponding best fitted values of the parameters are found.

Fig. 6.5 shows the time series plot of observed and predicted runoff for the calibration period for the Henval watershed. From the time series plot, it can be seen that even though the simulated runoff is underestimated, it follows the same trend as the observed runoff. Also, the rainfall distribution aligns well with the observed and simulated runoff suggesting the model performance satisfactory.

The statistical analysis with the most common metrics was carried out for the simulations of each watershed and results are shown in Table 6.4. The R^2 value for the calibration period was found as 0.75 and the NSE value ranged from 0.74 indicating the model calibration was performing satisfactory in terms of its predictive skills. And the variability of the simulation w.r.t the actual observations were analysed using RMSE (1.42) and the Bias (-15.7). Since the statistical analysis gave significant results, the same parameter values were used for validation and the model was stabilized.

Table 6. 1: Sensitivity Analysis for Henval sub-watershed

a) Quarterly scale

Parameter			Alpha Gw	Root layer thickness (mm)	Sub layer thickness (mm)	Recession Coefficient	DDFS (mm/degree/day)	GW layer thickness (mm)	Saturated GW content (mm)	Initial GW storage (mm)
Default Value			0.5	500	1500	0.4	6	3000	2000	1500
Change in Discharge (%)	**Annual**	50% decrease	-0.57	-15.32	0	0	-0.02	-0.01	-0.01	0
		50% increase	0.19	9.49	0	0	0	0	0	-0.01
	JFM	50% decrease	15.7	3.91	-0.01	0	0.67	0	0	0
		50% increase	-5.14	0.48	-0.01	0	-0.01	0	0	0
	AMJ	50% decrease	3.74	-96.11	-3.3	-7.98	0	1.83	1.83	0
		50% increase	-2.2	43.78	2.11	13.72	0	0	0	1.83
	JAS	50% decrease	-0.24	-8.48	0.27	0.71	0	-0.13	-0.13	0
		50% increase	0.17	6.84	-0.15	-1.19	0	0	0	-0.13
	OND	50% decrease	-102.9	39.45	36.5	17.29	0	-57.08	-57.08	0
		50% increase	29.91	-52.48	-45.56	-62.99	0	0	0	-57.08

b) Seasonal Scale

Parameter			Alpha Gw	Root layer thickness (mm)	Sub layer thickness (mm)	Recession Coefficient	DDFS (mm/degree/day)	GW layer thickness (mm)	Saturated GW content (mm)	Initial GW storage (mm)
Default Value			0.5	500	1500	0.4	6	3000	2000	1500
Change in Discharge (%)	**ANNUAL (WATER YEAR)**	50% decrease	0.07	-15.65	-0.01	-0.01	-0.07	-0.02	-0.02	0
		50% increase	-0.02	11.58	0.03	0.03	0	0	0	-0.02
	Monsoon (JJASO)	50% decrease	-0.03	-17.3	0.02	0.01	0	-0.03	-0.03	0
		50% increase	0.01	12.92	-0.01	-0.03	0	0	0	-0.03
	Winter (NDJF)	50% decrease	1.79	-1.16	-0.62	-0.36	-0.53	0.19	0.19	0
		50% increase	-0.52	0.52	0.77	1.15	0	0	0	0.2
	Summer (MAM)	50% decrease	1.79	1.16	0.62	0.36	0.53	0.19	0.19	0
		50% increase	0.52	0.52	0.77	1.15	0	0	0	0.2

Table 6. 2: Parameter ranking for Henval watershed

Parameters	Alpha Gw	Root layer thickness	Sub layer thickness	Recession coefficient	DDFS	Delta GW	GW layer thickness	Saturated GW content	Initial GW storage
Annual	2*	1	---	---	3**	3**	---	---	---
JFM	1	2	---	---	3*	4*	---	---	---
AMJ	3	1	4	2	---	5**	---	---	---
JAS	3*	1	3*	2	---	4**	---	---	---
OND	1	2	3	4	---	5	---	---	---
Monsoon (JJASO)	3**	1	4**	2**	---	5**	---	---	---
Winter (NDJF)	3*	1	4*	5*	2*	6**	---	---	---
Summer (MAM)	1	2	4	3	5*	6**	---	---	---
ANNUAL (WATER_YEAR)	2**	1	4**	5**	3**	---	---	---	---

Major influence *Minor influence **Negligible

Table 6. 3: Parameter values used for calibrating model for Henval sub-watershed

Rank	Major parameters	Parameter description	Unit	Range as per literature	Calibrated Value
1	Rootlayer thickness	Thickness of rootzone	mm	50 - 1000	500
2	Alpha GW	Baseflow recession coefficient	---	0.01 – 1.0	0.03
3	Recession Coefficient	Routing recession coefficient	---	0.01 – 0.99	0.9
4	Sublayer thickness	Thickness of subsoil	mm	300 - 3000	1000
5	DeltaGW	Groundwater recharge delay time	day	1 - 180	1

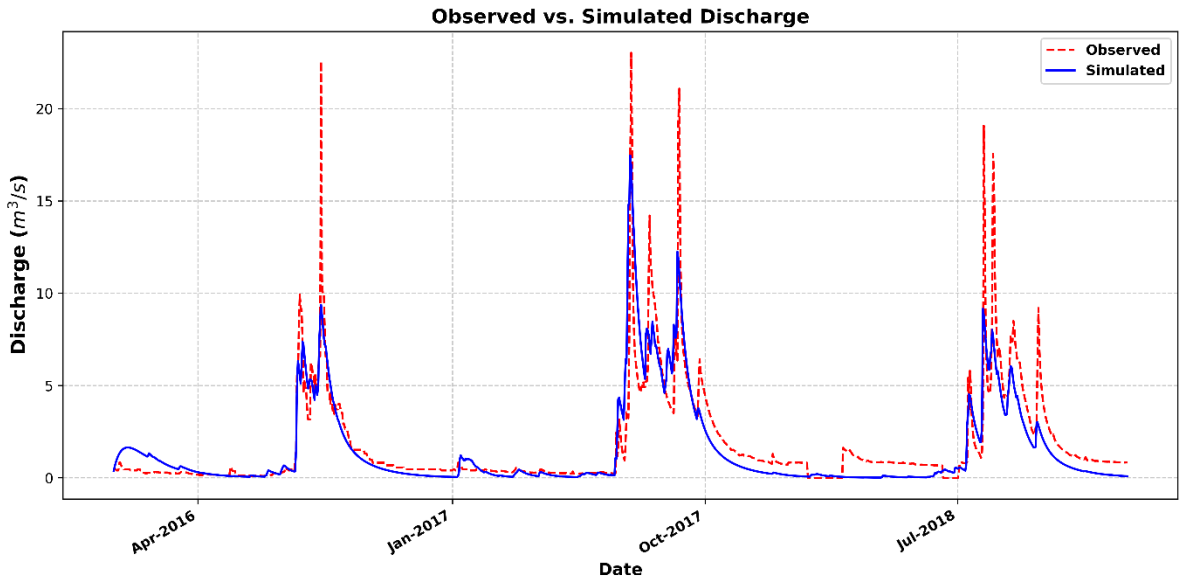

Fig. 6. 5: Time series plot of observed and simulated runoff during the calibration period in Henval watershed

Table 6. 4: Statistics for the calibrated models

Indicators	Range	Best Value	Henval Catchment
NSE	(- ∞ to 1)	1	0.74
RMSE	(0 to ∞)	0	1.4
R2	(0 to 1)	1	0.75
Bias	(- ∞ to ∞)	0	-15.7

6.5 Quantification of Routed Runoff components

The stabilized model after calibration and validation was statistically analyzed using different measures to evaluate the predictability and variability of the simulations and the results are tabulated in Table 6.5. The established models slightly improved their statistical performance from that of during calibration. The simulations for the Henval watershed were initially done for the period from 01/01/2016 to 31/12/2021 for the smaller sub watershed with the outlet at Jijali and the Fig. 6.6 shows the time series SPHY discharge output. Once found satisfactory, the model was then upscaled to the larger Henval watershed with the outlet at Shivapuri with the same parameter values for an extended period from 1/1/2010 to 31/12/2023. The output discharge obtained is illustrated in Fig. 6.7. The contribution of each of the runoff components were derived and represented as Fig. 6.8. The non-glaciated Henval watershed were having only two major runoff components – baseflow and rainfall induced runoff. The Rainfall

induced runoff contributes 83% to the total discharge in the watershed indicating the heavy dependency of the watershed on the rainfall especially during monsoon season for a thriving ecosystem and groundwater recharge. The visible fluctuations in the discharge over the year points out the changes in the rainfall regime in the region.

Table 6. 5: Statistics for the established models

Indicators	Range	Best Value	Henval
NSE	(- ∞ to 1)	1	0.74
RMSE	(0 to ∞)	0	1.4
R2	(0 to 1)	1	0.75
Bias	(- ∞ to ∞)	0	-15.7

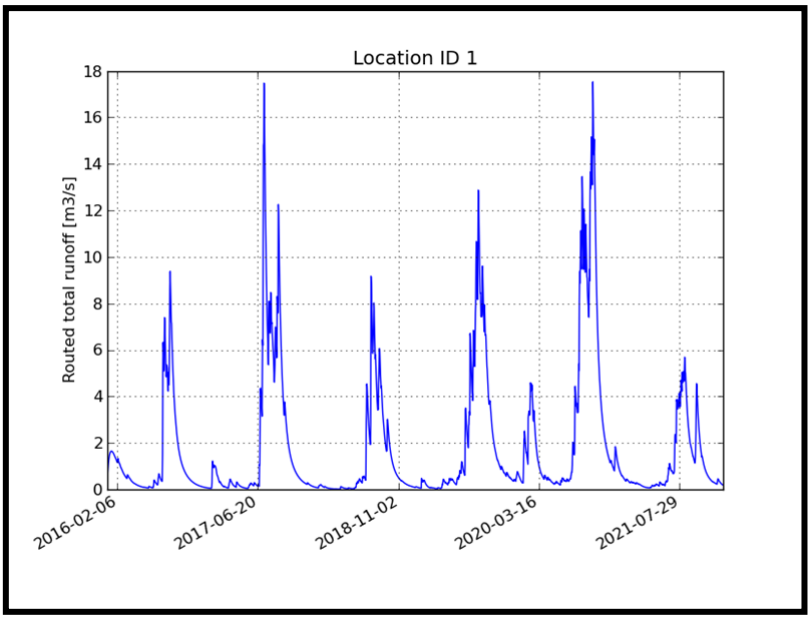

Fig. 6. 6: Time series SPHY output for the Henval sub-watershed

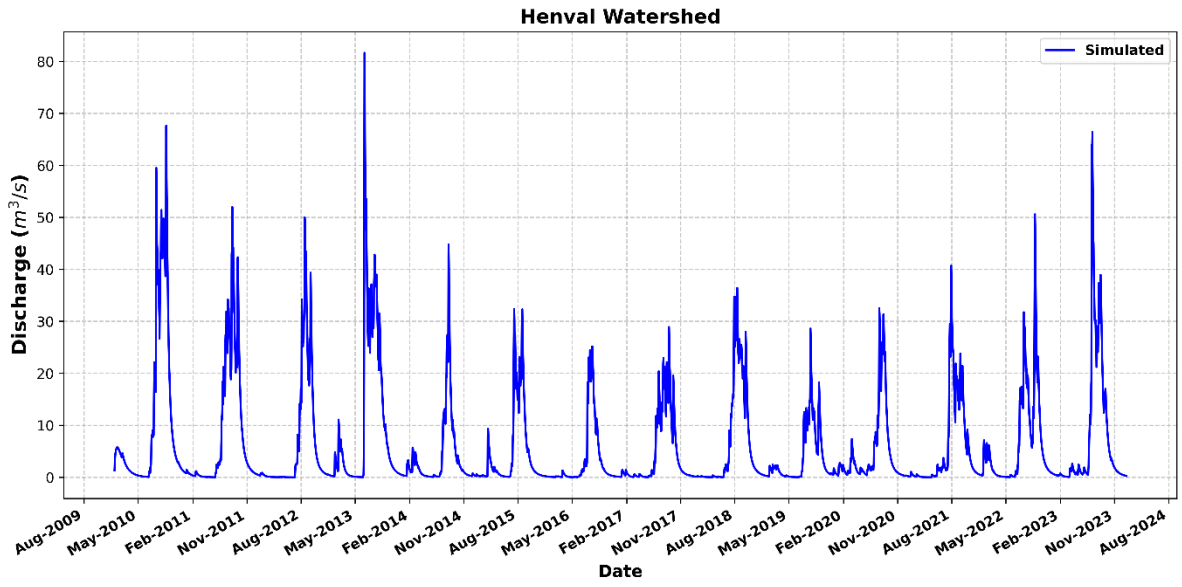

Fig. 6. 7: Time series SPHY output for the Henval watershed

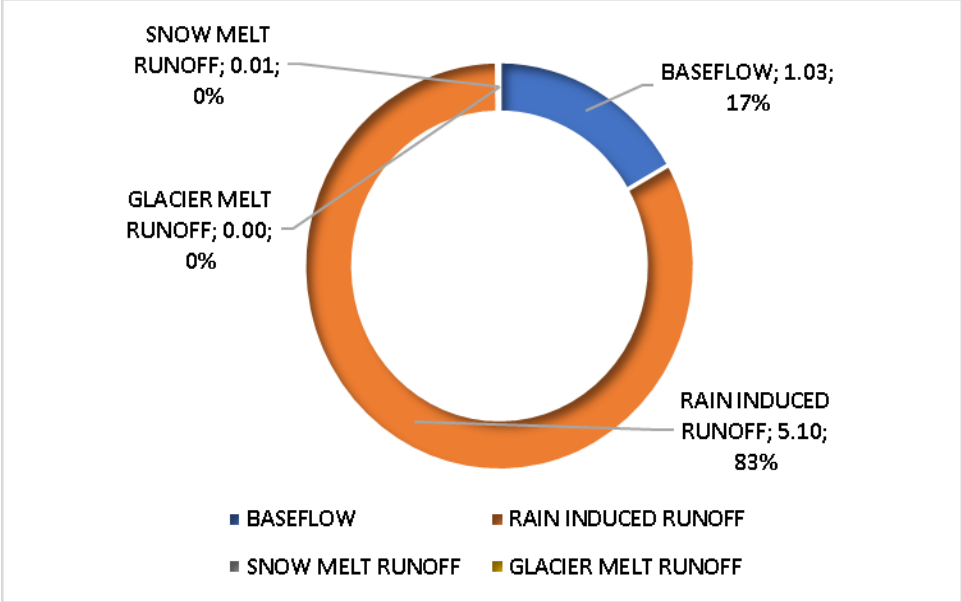

Fig. 6. 8: Relative contributions of different runoff components for the Henval watershed (m^3/s; %)

6.5 Water Balance of the watershed

Water Balance is defined as the numerical calculation accounting for the inputs to, outputs from, and changes in the volume of water in the various components (e.g. reservoir, river, aquifer) of the hydrological cycle, within a specified hydrological unit (e.g. river basin) and during a specified time unit (e.g. month/year), occurring both naturally and as a result of the

human-induced water abstractions and returns. Water in the catchment is always balanced and its components are influenced by the morphology of the watershed, climatic conditions, soil characteristics and land use land cover. It is simply based on the concept of change in the storage of water. It helps in the development of River Basin Management Plans by providing a coherent framework to cross-evaluate the information on drivers, pressures and impacts on water quantity and provides a sound basis for the quantitative management of water resources.

Estimation of the water balance components is a complicated task and can be achieved either using water balance models or hydrological models which have been developed at various time scales. The hydrologic processes are very complex and an understanding of the watershed model is essential. There exist numerous physically based distributed hydrological models and among them, SPHY is one of the widely used open-source models in glacierized regions. Since the current research aimed to understand the hydrological processes and analyze the hydrological response of the glaciated and non-glaciated watersheds in North West Himalya, SPHY model was chosen for both the kind of watersheds.

The most important hydrologic processes are surface runoff, lateral flow, baseflow and evapotranspiration and the cryospheric processes are Snow melt and Glacial melt. In this study SPHY model is used to evaluate water balance components in a non-glaciated watershed in the Upper Ganga Basin and the respective models were calibrated. The calibrated parameters were used for validation as well.

Once stabilized, the model was established for a duration of 14 years from 1/1/2010 to 31/12/2023. The SPHY model was found working satisfactorily for the Himalayan watershed despite their unique nature and challenges indicating the versatility of the SPHY model. This suggests the model could be used for simulating the hydrological response of the other watersheds in North West Himalaya. When supplemented with geospatial techniques and better datasets by integrating the in-situ data and satellite data in the data scarce Himalayan region, the model can be a very helpful tool to understand the hydrological processes and simulate the hydrological response of the watersheds in the region. In the context of the rising challenges due to the climate change, it is critical to understand the response of the Himalayan watersheds to the variations in the meteorological parameters due to their either glaciated or non-glaciated watersheds very dependent nature on temperature and precipitation regime for region's water availability. The integration of glacio-hydrologic models like SPHY, climate models and longer historical datasets can effectively help us to be resilient in the face of climate change

with better adaptation techniques and policies, given the hydrological and ecological importance of the Himalayan watersheds.

Chapter 7

7.0 SUMMARY OF REPORT

7.1 Empirical Soil Moisture Modelling

In pursuance of the study's second objective, an empirical model is formulated using available parameters in this study, i.e., rainfall, wind speed, air temperature, and near soil surface temperature. This model was calibrated and validated using the Kumargaon, Kanataal and Nagini sites in the lesser Himalayan region. The results indicated the best performance of the model at Kumargaon with high R2 in calibration and validation. These results are further supported by lower values of RMSE, ubRMSE, MAE and Pearson's correlation coefficient for this site. The model performed good at the other two sites of Kanataal and Nagini, but the results are comparatively inferior to Kumargaon. Furthermore, this model is simplified using the averaged values of optimized parameters and tested using the data used for validation. The results indicate that the simplified model also performed best at Kumargaon for all the soil depths with high R2 values which are obtained as 0.86 for 2 cm, 0.83 for 6 cm and 0.64 for 25 cm depths, respectively. Whereas for the similar soil depths at Kanataal, the performance was good only for the topmost layer of 2 cm with a high R2 value of 0.82. For the deeper soil layers at Kanataal, lower values of R2 (0.50 for 6 cm and 0.33 for 25 cm) indicates relatively average performance. Once again, the simplified model performed well at the site of Nagini with high R2 (0.81) value for the soil depth of 6 cm. It is also found that the model's performance decreases with increasing soil depth which indicates that the effect of meteorological variables decreases with the increasing soil depth. Yet, no ideal model would precisely predict soil moisture; hence, this quest emergence of deep learning models makes the process efficient and reliable. In the later part of the study's second objective, two deep learning hybrid models based on long-short term memory, namely, CNN-LSTM and RNN-LSTM, were developed and tested to model the sub-surface soil moisture at three stations located in a Lesser Himalayan catchment. The work is still ongoing, and findings will be shared in future working group meetings.

7.2 Soil Moisture Modelling Based on Machine Learning Models

Soil moisture is an essential component of the hydrological cycle which plays a critical role in planning and managing water resources in conjunction with sustainable irrigation and

agricultural practices. Hence, with the increasing computational capabilities for soil moisture prediction, many intelligent models and advanced algorithms have been developed for agricultural water management to extract features from historical data. Yet, there is no ideal model that would precisely predict soil moisture; hence, with this quest emergence of deep learning models makes the process efficient and reliable. In this paper, the Deep Learning hybrid models, namely, Convolution Neural Network - Long-Short Term Memory Network (CNN-LSTM) and Recurrent Neural Network - LSTM (RNN-LSTM), were designed to simulate the soil moisture at three stations located in a Lesser Himalayan catchment. The developed models were trained and tested for two depths (25cm and 50cm) with the meteorological data monitored at each of the three stations. The results demonstrate a more excellent predicting capability of the hybrid CNN-LSTM model concerning the counterpart comparative model. This is supported by relatively lower values of the mean absolute error (MAE), root-mean-square error (RMSE), and a higher value of the coefficient of determination (R2) for the CNN-LSTM model. In terms of statistical metrics used for training and testing the models, the proposed CNN-LSTM model was found considerably higher compared to the RNN-LSTM model. Therefore, the CNN-LSTM modeling technique can be endorsed for estimating soil moisture when the primary meteorological data are available. The proposed approach may be efficaciously implemented in hydrology and agriculture water management. Climate change is one of the world's most significant problems, having the potential to effect each and every sphere of the life on earth.

7.3 Hydrological Modeling using SPHY Model

This study focuses on key hydrological processes—surface runoff, lateral flow, baseflow, and evapotranspiration—alongside cryospheric processes such as snowmelt and glacier melt. The SPHY (Spatial Processes in Hydrology) model was employed to evaluate the water balance components of a non-glaciated watershed in the Upper Ganga Basin. The model was successfully calibrated and validated using observed data, and subsequently applied over a 14-year period (January 1, 2010 to December 31, 2023).

The results demonstrate that the SPHY model performs reliably in the context of Himalayan watersheds, which are characterized by complex terrain and climatic variability. This underscores the model's robustness and adaptability, suggesting its broader applicability for hydrological simulations in other watersheds across the northwestern Himalaya.

When enhanced with geospatial techniques and improved datasets—through the integration of in-situ and satellite observations—the SPHY model proves to be a valuable tool for understanding and simulating hydrological dynamics in data-scarce Himalayan regions. Given the region's sensitivity to variations in temperature and precipitation, particularly in both glaciated and non-glaciated watersheds, such modeling is crucial for assessing water availability under changing climatic conditions.

In light of the increasing challenges posed by climate change, the integration of glacio-hydrological models like SPHY with climate models and long-term datasets offers significant potential for developing effective adaptation strategies. This is particularly vital for ensuring water security and ecological sustainability in the Himalayan region.

*****

8.0 REFERENCES

Abraham, M.T., Satyam, N., Pradhan, B. and Alamri, A.M. (2020) Forecasting of landslides using rainfall severity and soil wetness: A probabilistic approach for Darjeeling Himalayas. Water, 12, 804.

Aguilar, J., Rogers, D. and Kisekka, I. (2015) Irrigation scheduling based on soil moisture sensors and evapotranspiration. Kansas Agricultural Experiment Station Research Reports, 1, 5, 20.

Ahmadisharaf, E., Camacho, R.A., Zhang, H.X., Hantush, M.M. and Mohamoud, Y.M. (2019) Calibration and validation of watershed models and advances in uncertainty analysis in TMDL studies. Journal of Hydrologic Engineering, 24, 7, 03119001.

Aksoy, H. and Kavvas, M.L. (2005) A review of hillslope and watershed scale erosion and sediment transport models. Catena, 64, 247-271.

Al-Kayssi, A.W., Al-Karaghouli, A.A., Hasson, A.M. and Beker, S.A. (1990) Influence of soil moisture content on soil temperature and heat storage under greenhouse conditions. Journal of Agricultural Engineering Research, 45, 241-252.

Allen, R.G., Pereira, L.S., Raes, D. and Smith, M. (1998) Crop Evapotranspiration: Guidelines for Computing Crop Water Requirements. Fao Irrigation and Drainage Paper 56; FAO-Food and Agriculture Organization of the United Nations Rome: Rome, It.

Arnoldus, H.M.J. (1980) An approximation of the rainfall factor in the Universal Soil Loss Equation. In: De Boodt, M., Gabriels, D. (Eds.), Assessment of Erosion. Wiley, Chichester, UK, pp. 127-13

ASCE (1970) Sediment sources and sediment yields. Journal of Hydraulics Division, ASCE, 96 (HY6), 1283– 1329.

Asgari, A., Bagheripour, M. and Mollazadeh, M. (2011) A generalized analytical solution for a non-linear infiltration equation using the exp-function method. Scientia Iranica, 18, 28-35.

Ashbridge, D. (1995) Processes of river bank erosion and their contribution to the suspended sediment load of the River Culm, Devon. In: Sediment and Water Quality in River Catchments, 229–245. Wiley, Chichester, UK.

Aubert, D., Loumagne, C. and Oudin, L. (2003) Sequential assimilation of soil moisture and stream flow data in a conceptual rainfall-runoff model. Journal of Hydrology, 280, 145–161.

Baba S.M.J. and Yusof, K.W. (2001) Modeling soil erosion in tropical environments using remote sensing and geographical informations systems. Hydrological Sciences Journal, 46(1), 191–198.

Bača, P. and Koníček, A. (2003) Suspended sediment dynamics during the baseflow in a small experimental Rybárik basin. Journal of Hydrology and Hydromechanics, 51(1), 52–61.

Barati, R. (2013) Application of excel solver for parameter estimation of the non-linear Muskingum models. KSCE Journal of Civil Engineering, 17(5), 1139–1148.

Basara J.B. (2001) Soil moisture observations for flash flood research and prediction. In: Gruntfest E., Handmer J. (eds) Coping With Flash Floods. NATO Science Series (Series 2. Environmental Security), vol 77. Springer, Dordrecht.

Belayneh, M., Yirgu, T. and Tsegaye, D. (2019) Potential soil erosion estimation and area prioritization for better conservation planning in Gumara watershed using RUSLE and GIS techniques. Environmental System Research, 8, 20.

Bennett, J.P. (1974) Concepts of mathematical modelling of sediment yield. Water Resources Research, 10, 485–492.

Berg, A., Lintner, B., Findell, K. and Giannini, A. (2017) Soil moisture influence on seasonality and large-scale circulation in simulations of the West African monsoon. Journal of Climate, 30, 2295– 2317.

Bogardi, I., Bardossy, A., Fogel, M. and Duckstein, L. (1986) Sediment yield from agricultural watersheds. Journal of Hydrologic Engineering., ASCE, 112(1), 64-70.

Broadbridge, P., Daly, E. and Goard, J. (2017) Exact solutions of the Richards equation with non-linear plant-root extraction. Water Resources Research, 53, 9679–9691.

Brocca, L., Ciabatta, L., Massari, C., Camici, S. and Tarpanelli, A. (2017) Soil moisture for hydrological applications: open questions and new opportunities. Water, 9, 2, 140.

Capehart, W.J. and Carlson, T.N. (1994) Estimating near surface soil moisture availability using meteorologically-driven soil water profile model. Journal of Hydrology, 160, 1–20.

Chifflard, P., Kranl, J., zur Strassen, G. and Zepp, H. (2017) The significance of soil moisture in forecasting characteristics of flood events. A statistical analysis in two nested catchments. Journal of Hydrology and Hydromechanics, 66, 1, 1-11.

Chow, V.T. (1964) Handbook of Applied Hydrology, McGraw-Hill Book Co. Inc., New York.

Cioni, G. and Hohenegger, C. (2017) Effect of soil moisture on diurnal convection and precipitation in large-eddy simulations. Journal of Hydrometeorology, 18, 7, 1885–1903.

Collier, C.G. (2016) Hydrometeorology; Wiley Blackwell: Hoboken, NJ, USA; University of Leeds: Leeds, UK.

De Girolamo, A. M., Pappagallo, G. and Lo Porto, A. (2015) Temporal variability of suspended sediment transport and rating curves in a Mediterranean river basin: The Celone (SE Italy), Catena, 128, 135–143. doi:10.1016/j.catena.2014.09.020.

Dickenson, R.E., Henderson-Sellers, A., Kennedy, P.J. and Wilson, M.F. (1986) Biosphere/atmosphere transfer scheme for NCAR community climate model. NCAR Technical Note TN275+STR. December, 69.

Dickinson, A. and Collins, R. (1998) Predicting erosion and sediment yield at the catchment scale. Soil erosion at multiple scales. CAB International, 317–342.

Dutta, S. (2016) Soil erosion, sediment yield and sedimentation of reservoir: a review. Modelling Earth Systems and Environment, 2, 123.

Ek, M.B. and Holtslag, A.A.M. (2004) Influence of soil moisture on boundary layer cloud development. Journal of Hydrometeorology, 5, 86–99.

Entekhabi, D. and Rodriguez-Iturbe, I. (1994) Analytical framework for the characterization of the space-time variability of soil moisture. Advances in Water Resources, 17, 35-45.

Feng, H. and Liu, Y. (2015) Combined effects of precipitation and air temperature on soil moisture in different land covers in a humid basin. Journal of Hydrology, 531, 1129–1140.

Feng, X., Porporato, A. and Rodriguez-Iturbe, I. (2015) Stochastic soil water balance under seasonal climates. Proceedings of Royal Society, 471, 20140623.

Garrido-Jurado, I., Valverde-Garcı´a, P. and Quesada-Moraga, E. (2011) Use of multiple logistic regression model to determine the effects of soil moisture and temperature on the Biocontrol Science and Technology 1211 virulence of entomopathogenic fungi againast pre-imaginal Mediterranean fruit fly Ceratitis capitata. Biological Control, 59, 366-372.

Graf, W. H. (1971) Hydraulics of Sediment Transport. McGraw-Hill, New York, N.Y., 513 pp.

Haarsma, R.J., Selten, F., van den Hurk, B., Hazeleger, W. and Wang, X. (2009) Drier Mediterranean soils due to greenhouse warming bring easterly winds over summertime central Europe. Geophysical Research Letters, 36, L04705.

Hagan, D.F.T., Parinussa, R.M., Wang, G. and Draper, C.S. (2019) An evaluation of soil moisture anomalies from global model-based datasets over the people's republic of China. Water, 12, 1, 117.

Hairsine, P. and Rose, C., (1992) Modelling water erosion due to overland flow using physical principles: 1. Sheet flow. Water Resources Research, 28 (1), 237–293.

Hargreaves, G.H. and Samani, Z.A. (1985) Reference crop evapotranspiration from temperature. Applied Engineering in Agriculture,1, 96–99.

Högstrom, U. (1996) Review of some basic characteristics of the atmospheric surface layer. Boundary Layer Meteorology, 78, (3-4), 215–246.

Huang, J., van den Dool, H.M. and Georgakakos, K.G. (1996) Analysis of model-calculated soil moisture over the US (1931 – 1993) and applications to long range temperature forecasts. Journal of Climate, 9, 1350 – 1362.

Hudson, J.A. (1988) The contribution of soil moisture storage to the water balances of upland forested and grassland catchments. Hydrological Sciences Journal, 33, 289–309.

Hudson, N. W. (1975) The factors determining the extent of soil erosion. In: Greemland, R. (Ed.), Soil Conservation and Management in the Humid Tropics. John Wiley and Sons.

Ives, J.D. and Messerli, B. (1989) The Himalayan dilemma: reconciling development and conservation. Routledge, London.

Jackson, S.H. (2003) Comparison of calculated and measured volumetric water content at four field sites. Agricultural Water Management, 58, 209-222.

Jain, M.K. and Kothyari, U.C. (2000) Estimation of soil erosion and sediment yield using GIS. Hydrological Sciences Journal, 45(5), 771–786.

Jain, S.K., Kumar, S. and Varghese, J. (2001) Estimation of soil loss for a Himalayan watershed using GIS technique. Water Resources Management, 15,41–54.

Jensen, D., Reager, J.T., Zajic, B., Rousseau, N., Rodell, M. and Hinkley, E. (2018) The sensitivity of US wildfire occurrence to pre-season soil moisture conditions across ecosystems. Environmental Research Letters, 13, 014021.

Jesan, T., Manonmani, C., Brindha, Jt., Rajaram, S., Ravi, P. and Tripathi, R. (2016) Estimation of roughness length Z 0 for Kalpakkam site . Radiation Protection and Environment, 39(1), 44.

Jin, M.S. and Mullens T. (2014) A study of the relations between soil moisture, soil temperatures and surface temperatures using ARM observations and offline CLM4 simulations. Climate, 2, 279–295.

Jose, C.S. and Das, D.C. (1982) Geomorphic prediction models for sediment production rate and intensive priorities of watershed in Mayurakshi catchment. In: Proceedings of the international symposium on hydrological aspects of mountainous watershed held at school of hydrology. University of Roorke, pp 15–23.

Kirkby, M.J. (1976) Hydrological slope models: the influence of climate. In Geomorphology and Climate (Derbyshire, E., Ed.). London: Wiley, 247-267.

Klein, M. (1984) Anti-clockwise hysteresis in suspended sediment concentration during individual storms. Catena, 11, 251–257.

Kong, X., Dorling, S. and Smith, R. (2011) Soil moisture modelling and validation at an agricultural site in Norfolk using the MetOffice surface exchange scheme (MOSES). Meteorological Applications, 18, 18–27.

Koppenhöfer, A.M. and Fuzy, E.M. (2007) Soil moisture effects on infectivity and persistence of the entomopathogenic nematodes Steinernema scarabaei, S. glaseri, Heterorhabditis zealandica, and H. bacteriophora. Applied Soil Ecology, 35(1), 128–139.

Koster, R.D., Chang, Y. and Schubert, S.D. (2014) A mechanism for land–atmosphere feedback involving planetary wave structures. Journal of Climate, 27, 9290–9301.

Koster, R.D., Chang, Y., Wang, H. and Schubert, S.D. (2016) Impacts of local soil moisture anomalies on the atmospheric circulation and on remote surface meteorological fields during boreal summer: A comprehensive analysis over North America. Journal of Climate, 29, 7345–7364.

Kothyari, U.C., Tiwari, A.K. and Singh, R. (1996) Temporal variation of sediment yield. Journal of Hydrologic Engineering, 1, (4), 169-176.

Kronvang, B., Laubel, A. and Grant, R. (1997) Suspended sediment and particulate phosphorus transport and delivery pathways in an arable catchment. Gelbaek stream, Denmark. Hydrological Processes, 11, 627–642.

Krueger, E.S., Ochsner, T.E., Engle, D.M., Carlson, J.D., Twidwell, D. and Fuhlendorf, S.D. (2015) Soil moisture affects growing-season wildfire size in the southern great plains. Soil Science Society of America Journal, 79, 1567–1576.

Kumar, S. and Rastogi, R.A. (1987) Conceptual catchment model for estimation of suspended sediment flow. Journal of Hydrology, 95, 155-163.

Kumari, S. (2019) Fuzzy-set-based real-time reservoir operation using genetic algorithm. ISH Journal of Hydraulic Engineering, 1–8.

Lana-Renault, N., Regues, D., Nadal-Romero, E., Serrano-Muela, M.P. and Garcia-Ruiz, J.M. (2010) Streamflow Response and Sediment Yield after Farmland Abandonament: Result from a small experimental catchment in the Central Spanish Pyrenees. Pirineos: revista de ecologia de montaña, 165, 97–114.

Lee, Y.H. and Singh, V.P. (2005) Tank model for sediment yield. Water Resources Management, 19, 349-362.

Legates, D.R. and McCabe Jr., G.J. (1999) Evaluating the use of goodness-of-fit measures in hydrologic and hydroclimatic model validation, Water Resources Research, 35, 1, 233–241.

Lettau, (1969) Note on aerodynamic roughness-parameter estimation on the basis of roughness element description. Journal of Applied Meteorology, 8, 828–832.

Lewis, T., Braun, C., Hardy, D.R., Francus, P. and Bradley, R.C. (2005) An extreme sediment transfer event in a Canadian High Arctic stream. Arctic Antarctic and Alpine Research, 37 (4), 477–482.

Liu, X., Luo, Y., Zhang, D., Zhang, M. and Liu, C. (2011) Recent changes in pan-evaporation dynamics in China. Geophysical Research Letters, 38, L13404.

Liu, Y., Liu, Y., Chen, M., Labat, D., Li, Y., Bian, X. and Ding, Q. (2019) Characteristics and drivers of reference evapotranspiration in hilly regions in Southern China. Water, 11(9), 1914.

Liu, Z.D., Qin, A., Duan, A., Zhang, J., Sun, J., Ning, D., Zhao, B., Mi, Z. and Liu, Z.G. (2017) Soil moisture and crop evapotranspiration forecast for winter wheat based on weather information in North China Plain. In Proceedings of the 2nd International Conference on Modelling, Simulation and Applied Mathematics, Bangkok, Thailand, 26–27 March 2017; pp. 295–299.

Loch, R.J. and Silburn, D.M. (1996) Constraints to sustainability—soil erosion erosion. In: Clarke, L., Wylie, P.B. (Eds.), Sustainable Crop Production in the Sub-tropics: An Australian Perspective. QDPI.

Mananze, S., Pôças, I. and Cunha, M. (2019) Agricultural drought monitoring based on soil moisture derived from the optical trapezoid model in Mozambique. Journal of Applied Remote Sensing, 13, 024519.

Mantovani, D., Veste, M., Badorreck, A. and Freese, D. (2013) Evaluation of fast growing tree water use under different soil moisture regimes using wick lysimeters. iForest - Biogeosciences and Forestry, 6, 190–200.

Massari, C., Camici, S., Ciabatta, L. and Brocca, L. (2018) Exploiting satellite-based surface soil moisture for flood forecasting in the Mediterranean area: state update versus rainfall correction. Remote Sensing, 10(2), 292.

McVicar, T.R., Roderick, M.L., Donohue, R.J. and Van Niel, T.G. (2012) Less bluster ahead? Ecohydrological implications of global trends of terrestrial near-surface wind speeds. Ecohydrology, 5, 381–388.

Mehrotra, R. (1999) Sensitivity of runoff, soil moisture and reservoir design to climate change in central Indian river basins. Climatic Change, 42, 725–757.

Meng, L. and Quiring, S.M. (2008) A comparison of soil moisture models using soil climate analysis network observations. Journal of Hydrometeorology, 9, 641–659.

Merritt, W.S., Letcher, R.A. and Jakeman, A.J. (2003) A review of erosion and sediment transport models. Environmental Modelling & Software, 18, 761–799.

Meyer, L.D. and Wischmeier, W.H. (1969) Mathematical simulation of the process of soil erosion by water. Transactions of American Society of Agricultural Engineers, 12,754– 758, 762.

Monteith, J.L. (1973) Principles of Environmental Physic. . London: Edward Arnold. 1–418.

Moore, I.D. and Burch, G.J. (1986a) Physical basis of the length slope factor in the Universal Soil Loss Equation. Soil Science Society of America, 50 (5), 1294-1298.

Moore, I.D. and Burch, G.J. (1986b) Modeling erosion and deposition. Topographic effects. Transactions of American Society of Agriculture Engineering 29 (6), 1624-1630.

Moore, T.J. and Jones, M.R. (2015) Solving non-linear heat transfer problems using variation of parameters. International Journal of Thermal Sciences, 93, 29–35.

Moriasi, D.N., Gitau, M.W., Pai, N. and Daggupati, P. (2015) Hydrologic and water quality models: Performance measures and evaluation criteria. Transactions of ASABE, 58(6), 1763-1785.

Mozny, M., Trnka, M., Zalud, Z., Hlavinka, P., Nekovar, J., Potop, V. and Virag, M. (2012) Use of a soil moisture network for drought monitoring in the Czech Republic. Theoretical and Applied Climatology, 107, 99–111.

Nippes, K.R. (1971) A new method of computation of the suspended sediment load. Proceedings of Symposium 'Mathematical Models in Hydrology', Vol. II, pp. 659-666.

Onderka, M., Krein, A., Wrede, S., MartÌnez-Carreras, N. and Hoffmann, L. (2012) Dynamics of storm-driven suspended sediments in a headwater catchment described by multivariable modeling. Journal of Soils and Sediments, 12, 620-635. doi:10.1007/s11368- 012-0480-6.

Pan, F., Peters-Lidard, C.D. and Sale, M.J. (2003) An analytical method for predicting surface soil moisture from rainfall observations. Water Resources Research, 39, 11, 1314-1328.

Pathak, S. and Singh, T. (2016) The solution of non-linear problem arising in infiltration phenomenon in unsaturated soil by optimal homotopy analysis method. International Journal of Advances in Applied Mathematics and Mechanics, 4, 21–28.

Patil, M.N. (2006) Aerodynamic drag coefficient and roughness length for three seasons over a tropical western Indian station. Atmospheric Research, 80(4), 280–293. https://doi.org/10.1016/j.atmosres.2005.10.005.

Peichl, M., Thober, S., Meyer, V. and Samaniego, L. (2018) The effect of soil moisture anomalies on maize yield in Germany. Natural Hazards Earth System Sciences, 18, 889–906.

Priestley C.H.B. and Taylor R.J. (1972) On the assessment of surface heat flux and evaporation using large-scale parameters. Monthly Weather Review, 100, 81-92.

Qiu, Y., Fu, B., Wang, J. and Chen, L. (2003) Spatiotemporal prediction of soil moisture content using multiple-linear regression in a small catchment of the Loess Plateau, China. Catena, 54, 1-2, 173–195.

Rahmani, V., Kastens, J.H., DeNoyelles, F., Jakubauskas, M.E., Martinko, E.A., Huggins, D.H., Gnau, C., Liechti, P.M., Campbell, S.W., Callihan, R.A. and Blackwood, A.J. (2018) Examining Storage Capacity Loss and Sedimentation Rate of Large Reservoirs in the Central U.S. Great Plains. Water, 10, 190.

Rao, K.G. (1996) Roughness length and drag coefficient at two MONTBLEX-90 tower stations. Proceedings - Indian Academy of Sciences, Earth and Planetary Sciences, 105(3), 273–287. https://doi.org/10.1007/BF02841883.

Rayner, D.P. (2007) Wind run changes: The dominant factor affecting pan evaporation trends in Australia. Journal of Climate, 20, 3379–3394.

Renschler, C., Diekkruger, B. and Mannaerts, C. (1997) Regionalization in surface runoff and soil erosion risk evaluation. In: Regionalization of hydrology, vol 254. IAHS Publishers, UK, pp 233–241.

Robock, A., Schlosser, C.A., Ya. Vinnikov, K., Speranskaya, N.A., Entin, J.K. and Qiu, S. (1998) Evaluation of the AMIP soil moisture simulations. Global and Planetary Change, 19, 181–208.

Roderick, M.L., Rotstayn, L.D., Farquhar, G.D. and Hobbins, M.T. (2007) On the attribution of changing pan evaporation. Geophysical Research Letters, 34, L17403.

Rose, C.W. (1993) Erosion and sedimentation. In: Bonell, M., Hufschmidt, M.M., Gladwell, J.S. (Eds.), Hydrology and Water Management in the Humid Tropics: Hydrological Research Issues and Strategies for Water Management. Cambridge University Press, pp. 301–343.

Rossato, L., dos Santos Alvalá, R.C., Marengo, J.A., Zeri, M., do Amaral Cunha, A.P.M., Pires, L.B.M. and Barbosa, H.A. (2017) Impact of soil moisture on crop yields over Brazilian semiarid. Frontiers in Environmental Science, 5, 1–16.

Russell, M.A., Walling, D.E. and Hodgkinson, R.A. (2001) Suspended sediment sources in two small lowland agricultural catchments in the UK. Journal of Hydrology, 252, 1–24.

Salugin, A.N, Kulik, A.K. and Vlasenko, M.V. (2018) Dynamics of water-balance elements in models of soil hydrological processes. Russian Agricultural Sciences, 44, 4, 369-372.

Schroder, J.H. (2006) Soil moisture-based drip irrigation for efficient use of water and nutrients and sustainability of vegetables cropped on coarse soils. M.Sc. Dissertation. University of Florida, Gainesville.

Singh, V.P. (1989) Hydrologic Systems: Vol. 2: Watershed Modeling, Prentice Hall, Englewood Cliffs, N. J.

Soler, M., Latron, G. and Gallart, F. (2008) Relationships between suspended sediment concentrations and discharge in two small research basins in a mountainous Mediterranean Area (Vallcebre, Eastern Pyrenees). Geomorphology, 98, 143–152.

Srinivasa Prasad, A., Umamahesh, N.V. and Viswanath, G.K. (2013) Short-term real-time reservoir operation for irrigation. Journal of Water Resources Planning and Management, 139, 2, 149–158.

Stull, R.B. (1988) An introduction to boundary layer meteorology. An Introduction to Boundary Layer Meteorology. https://doi.org/10.1007/978-94-009-3027-8

Tananaev, N.I. (2013) Hysteresis effects of suspended sediment transport in relation to geomorphic conditions and dominant sediment sources in medium and large rivers of the Russian Arctic. Hydrology Research, 46 (2), 232–243. doi:10.2166/nh.2013.199.

Tang, B., Tong, L., Kang, S. and Zhang, L. (2011) Impacts of climate variability on reference evapotranspiration over 58 years in the Haihe river basin of north China. Agricultural Water Management, 98, 1660–1670.

Tang, C. and Chen, D. (2017) Interaction between soil moisture and air temperature in the Mississippi river basin. Journal of Water Resource and Protection, 9, 1119–1131

Thornthwaite, C.W. and Mather, J.R. (1957) Instructions and tables for computing potential evapotranspiration and the water balance. Publications in Climatology, 10(3).

Van der Linden, E.C., Haarsma, R.J. and Van der Schrier, G. (2019) Impact of climate model resolution on soil moisture projections in central-western Europe. Hydrology and Earth System Sciences, 23, 191–206.

Venkatesh, B., Nandagiri, L., Purandara, B.K. and Reddy, V.B. (2011) Modelling soil moisture under different land covers in a sub-humid environment of Western Ghats, India. Journal of Earth System Sciences, 120, 387.

Viterbo, P. and Betts, A.K. (1999) Impact of the ECMWF reanalysis soil water on forecasts of the July 1993 Mississippi flood. Journal of Geophysical Research, 104, 19,361-19,366.

Walker, J.P., Willgoose, G.R. and Kalma, J.D. (2001) One-dimensional soil moisture profile retrieval by assimilation of near-surface measurements: A simplified soil moisture model and field application. Journal of Hydrometeorology, 2, 356 – 373.

Walling, D.E. and Webb, B.W. (1996) Erosion and sediment yield: a global overview. In: Walling, D.E., Webb, B.W. (Eds.), Erosion and Sediment Yield: Global and Regional Perspectives. IAHS Publication, 236, 3 – 19.

Williams, G.P. (1989) Sediment concentration versus water discharge during single hydrologic events in rivers. Journal of Hydrology, 111(1-4), 89–106. doi:10.1016/0022-1694(89)90254-0.

Williams, J.R. and Berndt, H.D. (1977) Sediment yield prediction based on watershed hydrology. Transactions of ASAE, 20,1100–1104.

Wischmeier, W.H. and Smith, D.D. (1978) Predicting rainfall erosion losses. USDA agricultural research services handbook 537. USDA, Washington, DC.

World Meteorological Organization. (1981) Meteorological aspects of the utilization of wind as an energy source. Technical note no. 175, World Meteorological Organization.

Yellen, B., Woodruff, J.D., Kratz, L.N., Mabee, S.B., Morrison, J. and Martini, A.M. (2014) Source, conveyance and fate of suspended sediments following Hurricane Irene. New England, USA. Geomorphology, 226, 124-134.

Yeshaneh, E., Eder, A. and Blöschl, G. (2013) Temporal variation of Suspended Sediment transport in the Koga Catchment, North Western Ethiopia and environmental implications, Hydrological Processes, 28, 5972-5984.

Zakwan, M. (2017) Assessment of dimensionless form of Kostiakov model. Aqudemia: Water Environment and Technology, 1, 1, 01.

Zakwan, M., Muzzammil, M. and Alam, J. (2016) Application of spreadsheet to estimate infiltration parameters. Perspective in Science, 8, 702-704.

Zakwan, M., Muzzammil, M. and Alam, J. (2017) Developing stage-discharge relations using optimization techniques. Aquademia: Water, Environment and Technology, 1, 2, 05.

Zhang, F., Pu, Z. and Wang, C. (2019) Impacts of soil moisture on the numerical simulation of a post landfall storm. Journal of Meteorological Research, 33, 206–218.

Zhang, Q., Zeng, J. and Yao, T. (2012) Interaction of aerodynamic roughness length and windflow conditions and its parameterization over vegetation surface. Chinese Science Bulletin, 57(13), 1559–1567. https://doi.org/10.1007/s11434-012-5000-y.

Zhang, R., Wang, J., Zhu, C., Sun, X. and Zhu, Z. (2004) The retrieval of two-dimensional distribution of the earth's surface aerodynamic roughness using SAR image and TM thermal infrared image. Science in China, Series D: Earth Sciences, 47(12), 1134–1146.

Zhang, Y. (2018) Estimation of Potential Evapotranspiration by Different Methods in Handan Eastern Plain, China, American Journal of Water Science and Engineering, 4, 4, 117-123.

Zheng, H., Liu, X., Liu, C., Dai, X., and Zhu, R. (2009) Assessing contributions to panevaporation trends in Haihe river basin, China. Journal of Geophysical Research Atmosphere, 114, D24105.

Zhou, X. and Geerts, B. (2013) The influence of soil moisture on the planetary boundary layer and on cumulus convection over an isolated mountain. Part I: Observations. Monthly Weather Review, 141, 3, 1061–1078.

Zhou, Y., Sun, X., Zhu, Z., Zhang, R., Tian, J., Liu, Y., Guan, D. and Yuan, G. (2006) Surface roughness length dynamic over several different surfaces and its effects on modeling fluxes. Science in China, Series D: Earth Sciences, 49(SUPPL. 2), 262–272.

Zhuo, L., Dai, Q., Han, D., Chen, N., Zhao, B. and Berti, M. (2019) Evaluation of remotely sensed soil moisture for landslide hazard assessment. IEEE Journal of Selected Topics in Applied Earth Observations and Remote Sensing, 12, 162–173.

Zhuo, L., Han, D. and Dai, Q. (2017) Exploration of empirical relationship between surface soil temperature and surface soil moisture over two catchments of contrasting climates and land covers. Arabian Journal of Geosciences, 10, 410.

Zuecco, G., Penna, D., Borga, M. and van Meerveld, H.J. (2016) A versatile index to characterize hysteresis between hydrological variables at the runoff event timescale, Hydrological Processes, 30, 1449– 1466.

Abbes, A. B. (2019). Soil moisture estimation from SMAP observations using long short-term memory (LSTM). In IGARSS 2019-2019 IEEE International Geoscience and Remote Sensing Symposium (pp. 1590-1593). IEEE.

Albawi, S. M.-Z. (2017). Understanding of a convolutional neural network. In 2017 International Conference on Engineering and Technology (ICET (pp. 1-6). Ieee.

Alibabaei, K. G. (2021). Modeling Soil Water Content and Reference Evapotranspiration from Climate Data Using Deep Learning Method. Applied Sciences, 11(11), 5029.

Bromberg, C. L. (2019). Machine Learning for Precipitation Nowcasting from Radar Images.

Cai, Y. Z. (2019). Research on soil moisture prediction model based on deep learning. PloS one, 14(4), e0214508.

Dawson, C. W. (2007). HydroTest: a web-based toolbox of evaluation metrics for the standardised assessment of hydrological forecasts. Environmental Modelling & Software, 22(7), 1034-1052.

Frenken, K. &. (2012). Irrigation water requirement and water withdrawal by country. FAO.

Hochreiter, S. &. (1997). Long short-term memory. Neural computation, 9(8), 1735-1780.

Ji, R. Z. (2017). Prediction of soil moisture based on multilayer neural network with multi-valued neurons. Transactions of the Chinese Society of Agricultural Engineering, 33(1), 126-131.

Kingston, D. G. (2009). Uncertainty in the estimation of potential evapotranspiration under climate change. Geophysical Research Letters, 36(20).

Le Houérou, H. N. (1996). Climate change, drought and desertification. Journal of arid Environments, 34(2), 133-185.

Medsker, L. R. (2001). Recurrent neural networks. Design and Applications, 5, 64-67.

Moriasi, D. A. (2007). Model Evaluation Guidelines for Systematic Quantification of Accuracy in Watershed Simulations. Transactions of the ASABE, 50, 885-900.

Prakash, S. &. (2020). Soil Moisture Prediction Using Shallow Neural Network. International Journal of Advanced Research in Engineering and Technology, 11(6).

Prakash, S. S. (2018). Soil moisture prediction using machine learning. In 2018 Second International Conference on Inventive Communication and Computational Technologies (ICICCT) (pp. 1-6). IEEE.

Rumelhart, D. E. (1986). Learning representations by back-propagating errors. Nature, 323(6088), 533-536.

Sharma, S. &. (2017). Activation functions in neural networks. Towards Data Science, 6(12), 310-316.

Vateekul, P. &. (2009,). Tree-based approach to missing data imputation. In 2009 IEEE International Conference on Data Mining Workshops (pp. 70-75). IEEE.

*****